DISTRIBUTED ROUGHNESS RECEPTIVITY IN A FLAT PLATE BOUNDARY LAYER

A Dissertation

by

MATTHEW SCOTT KUESTER

Submitted to the Office of Graduate and Professional Studies of
Texas A&M University
in partial fulfillment of the requirements for the degree of

DOCTOR OF PHILOSOPHY

Chair of Committee,	Edward White
Committee Members,	William Saric
	Rodney Bowersox
	Gerald Morrison
Head of Department,	Rodney Bowersox

May 2014

Major Subject: Aerospace Engineering

ABSTRACT

Surface roughness can affect boundary layer transition by acting as a receptivity mechanism for transient growth. Several experiments have investigated transient growth created by discrete roughness elements; however, very few experiments have studied transient growth initiated by distributed surface roughness. Some of the work in this field predicts a "shielding" effect, where smaller distributed roughness displaces the boundary layer away from the wall and shields larger roughness peaks from the incoming boundary layer.

This dissertation describes an experiment specifically designed to study the shielding effect. Three roughness configurations, a deterministic distributed roughness patch, a slanted rectangle, and the combination of the two, were manufactured using rapid prototyping and installed flush with the wall in a flat plate boundary layer. The main objective was to compare the wakes of the discrete roughness and the combined roughness to examine if the distributed roughness shields the discrete roughness. Naphthalene flow visualization and hotwire anemometry were used to characterize the boundary layer in the wakes of the different roughness configurations.

For roughness Reynolds numbers ($\mathrm{Re_k}$) between 113 and 230, the distributed roughness initiated small amplitude disturbances that underwent transient growth. The discrete roughness element created a pair of high- and low-speed streaks in the boundary layer at a sub-critical Reynolds number ($\mathrm{Re_k} = 151$). At a higher Reynolds number ($\mathrm{Re_k} = 220$), the discrete element created a turbulent wedge 15 boundary layer thicknesses downstream.

When the distributed roughness was added around the discrete roughness, the wake amplitude decreased at the sub-critical Reynolds number, and transition was

delayed by two boundary layer thicknesses at the higher Reynolds number. The distributed roughness redirects energy from longer spanwise wavelength modes to shorter spanwise wavelength modes. The presence of the distributed roughness also decreased the growth rate of secondary instabilities in the roughness wake.

This dissertation documents the first detailed measurements of transient growth over streamwise-extended distributed roughness and demonstrates that the shielding effect has the potential to delay roughness-induced transition. The results from this experiment lay the ground work for future studies of roughness receptivity and transient growth.

DEDICATION

I dedicate this dissertation to all of my family and, in particular, my loving wife. Thank you all for your love and support.

ACKNOWLEDGEMENTS

First and foremost, I would like to acknowledge the Air Force Office of Scientific Research (AFOSR) for funding this work through AFOSR Grant FA9550-11-1-0203. I would also like to acknowledge NASA and ASEE for the NASA Aeronautics Scholarship program, which supported me through my first two years in graduate school.

This dissertation would not have been possible without the help of many people. First, thanks is given to Dr. David Goldstein and Dr. Arjun Sharma at the University of Texas at Austin. Through our teleconferences, I improved my presentation skills and honed several aspects of this research. The same could be said for the past and current students that have worked with Dr. White and Dr. Saric, including Alex Craig, Brian Crawford, Dr. Nicholas Denissen, Dr. Robert Downs III, Glen Duncan, Robert Ehrmann, Dr. Jerrod Hofferth, Dr. Lauren Hunt, Robert Long, Jason Monschke, Dr. Jason Schmucker, Nicole Sharp, Jamie Weber, David West, and Ben Wilcox. Thanks to all of you for your help building the KSWT and/or your presence as a tunnel operator. In particular, Bobby (Robert) Ehrmann, Jason Monschke, and Ben Wilcox deserve special recognition for being a second tunnel operator for most of this dissertation research. I also want to give a special thanks to Chi Mai, who spent some late nights at the KSWT to help me finish data collection.

I would like to acknowledge my committee members (Dr. Gerald Morrison, Dr. Rodney Bowersox, Dr. William Saric, and especially my advisor Dr. Edward White) for their support throughout this endeavor. Finally, I would like to thank all of my family and friends who encouraged me along the way and helped me discover the path that led to this dissertation - there are too many of you to name, but I am very appreciative for your love and guidance.

TABLE OF CONTENTS

LIST OF FIGURES

FIGURE Page

LIST OF TABLES

TABLE Page

1. INTRODUCTION AND BACKGROUND

Understanding and controlling boundary layer transition from laminar to turbulent flow is critical for numerous aerodynamic applications. For example, the reduction in skin friction drag for laminar flow compared to turbulent flow could increase the range and fuel efficiency of commercial airliners. Joslin [1] gives quantitative examples of improvements in total airplane drag and takeoff gross weight by maintaining laminar flow on an airplane's wings and empennage.

Early attempts to understand the role of roughness in boundary layer transition focused on the growth of modal instabilities such as Tollmien–Schlichting (T–S) waves; however, transient growth has emerged as a possible explanation for roughness-induced transition. Reshotko [2] was one of the first to point out the potential links between roughness-induced transition and transient growth. Transient growth occurs through a combination of stable, continuous, and non-orthogonal disturbance modes. As the disturbance modes decay downstream at different spatial rates, the sum of the modes can grow due to the non-orthogonal nature of the linear stability equations. If this growth is large enough, transition can occur due to secondary instabilities (Path C on the transition roadmap from Morkovin et al. [3] shown in Fig. 1.1) or bypass transition (Path D). Transient growth can occur upstream of the onset of modal instabilities and thus may explain boundary layer transition in regions where linear stability analysis indicates a stable boundary layer.

1.1 Previous Research - Transient Growth and Roughness Receptivity

The physical mechanism behind transient growth was first identified by Ellingsen & Palm [4] and Landahl [5]. Transient growth is initiated by weakly damped vortical disturbances in the boundary layer. These vortices redistribute momentum

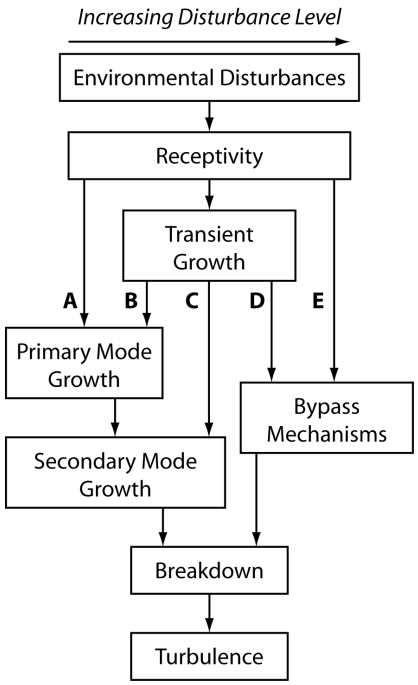

Figure 1.1: Transition roadmap (from Morkovin et al.)

from the freestream into the boundary layer. Even though the vortices are stable and damped by viscosity, the redistribution of streamwise momentum can cause the steady and low frequency streamwise velocity disturbances to grow linearly before decaying exponentially further downstream. The redistribution of streamwise momentum eventually forms low- and high-speed streamwise streaks. If the streaks are large enough in magnitude, transition can occur through secondary instabilities caused by spanwise inflectional profiles in the wake structure [6, 7].

A majority of theoretical work regarding spatial transient growth has focused on optimal disturbances, or the disturbances that undergo the maximum spatial transient growth over a specified domain. Several authors have studied spatial optimal growth in zero-pressure gradient boundary layers: Andersson et al. [8] investigated stationary ($\omega = 0$) disturbances in a non-parallel boundary layer, Luchini [9] in-

vestigated steady and unsteady disturbances in a non-parallel boundary layer, and Tumin & Reshotko [10] investigated stationary and non-stationary disturbances in a parallel boundary layer using a composition of continuous modes of the linear stability equations. Andersson et al. [7] performed a full DNS to validate the linear calculations. All of these authors found similar results; for a Blasius boundary layer, optimal disturbances are stationary ($\omega = 0$) streamwise vortices with a non-dimensional spanwise wavenumber (β) near 0.45. These studies also agreed on the shape of the optimal disturbance structure, which has a peak in the steady velocity disturbance (U') near the height in the boundary layer where $U/U_e = 0.553$, or $\eta = 2.2$.

Experiments at Case Western Reserve University (CWRU) [6,11–16] studied transient growth behind an array of cylindrical roughness elements. These experiments also motivated numerical simulations [17–21] of the flow around and downstream of cylindrical roughness elements. The experiments showed that transient growth is highly dependent on receptivity. Instead of creating optimal disturbances, the roughness arrays created disturbances that remained closer to the wall than predicted by optimal theory. The experiments also showed that the point of maximum transient growth occurred further upstream than indicated by optimal theory. Further, White et al. [14] showed that the nature of roughness-induced transient growth can be changed by varying the height and width of the roughness.

Representing transient growth as a sum of modes of the linear stability equations, as Tumin & Reshotko [10] formulated the optimal disturbance problem, allows receptivity to be defined as the distribution of coefficients (C_α) that multiply the distribution of streamwise modes that form the disturbance. Once the distribution of C_α is known, the entire disturbance (at a particular spanwise wavenumber) can be defined as an integral of different streamwise modes. Quantifying C_α also provides

a means to compare the receptivity of different roughness geometries. Equation 1.1 shows the reconstruction of the velocity disturbance for a single spanwise Fourier mode based on the combination of linear modes, while Fig. 1.2 shows the corresponding experimental setup.

$$\hat{u}_{\lambda_z}(x,\eta) = \int_{\alpha} \left[C_{\alpha,\lambda_z} e^{i\alpha(x-x_0)} \hat{u}_{\alpha,\lambda_z}(\eta) \right] d\alpha + C.C. \tag{1.1}$$

Tumin & Reshotko [22] developed a linear receptivity model to study three-dimensional humps in a Blasius boundary layer. They calculated the continuous spectrum of modes of the linearized stability equations at the streamwise location of a discrete roughness elements and calculated the mode amplitudes based on the Fourier transform of the roughness element geometry. They then investigated the resulting downstream flow-field using Eq. 1.1. Their results showed the qualitative trends of transient growth but did not quantitatively describe the roughness wake of the cases they tested. Tumin & Reshotko pointed out: "The question about the role of the nonlinear receptivity mechanism in the transient growth has to be addressed in the future"; because their method was inherently linear, it was incapable of capturing non-linear receptivity effects.

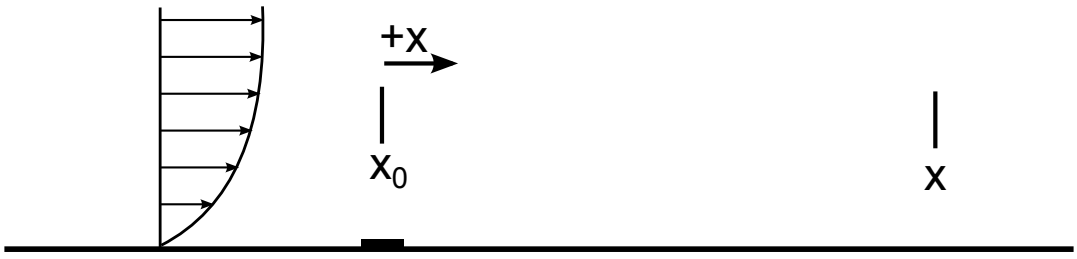

Figure 1.2: Sketch of receptivity at a single streamwise location

In order to quantify receptivity observed in the CWRU experiments, Denissen & White [23] used modal decomposition to describe the receptivity of roughness at a known, single streamwise location. This technique utilizes data collected in the roughness wake to reconstruct the mode amplitudes that were initiated by the roughness. The far-field roughness wake is decomposed into spanwise wavelengths, and each spanwise wavelength is represented as an integral of modes of the linear stability equations at different streamwise wavelengths. They showed that the C_α distribution can be calculated given a full set of DNS data (from Rizzetta & Visbal [19]) or streamwise velocity profiles at several streamwise locations (from Ergin & White [6]) in the roughness wake.

There are two important points that should be mentioned when discussing the modal decomposition technique used by Denissen & White [23]. The disturbance modes used in the decomposition are calculated assuming a parallel boundary layer (U(y)) at a constant Reynolds number (R_δ), and thus this approach defines receptivity within the context of parallel flow. Secondly, the location of x_0 shown in Eq. 1.1 and Fig. 1.2 is not necessarily the location of the roughness. Instead, x_0 is set as the decomposition location. The technique calculates the C_α distribution that matches the disturbance at x_0, and thus it measures the collective receptivity of roughness upstream of the decomposition location. For the aforementioned experiments at CWRU (where the roughness was at a single streamwise location), modal decomposition provides the specific details of roughness receptivity. In cases with roughness at multiple streamwise locations, modal decomposition will provide the net receptivity of all of the roughness rather than specific receptivity details.

1.2 Motivation for Proposed Research - Distributed Receptivity

In many practical applications, such as wind turbine blade erosion or dirt accumulation on an aircraft wing, distributed roughness has the potential to cause boundary layer transition upstream of the growth of modal instabilities. Extending transient growth theory to applications with roughness at multiple streamwise locations will constitute a step towards incorporating transient growth into a comprehensive transition road map.

Over the past 80 years, many experiments have tested the effect of distributed roughness on boundary layer transition; however, only a handful of these experiments have made the detailed measurements necessary to quantify roughness-induced disturbance growth. Reshotko & Leventhal [24] measured streamwise velocity on the centerline of a flat plate with sandpaper roughness. In their experiment, the distributed roughness displaced the boundary layer away from the wall. They also measured low-frequency oscillations that were later identified as transient growth. Kendall [25] used glass beads to create a distributed roughness field and noticed the same displacement of the boundary layer away from the wall. Corke et al. [26] measured enhanced growth of T–S waves in the presence of sandpaper roughness in a flat plate boundary layer, but the roughness was located downstream of the T–S wave neutral stability curve. In this case, the roughness modified the growth rate of T–S waves rather than acting as a receptivity mechanism for transient growth. White & Reshotko [27] also studied the effect of sandpaper roughness in a Blasius boundary layer but did not see any indication of transient growth (the authors indicate that this may be attributed to the experimental setup).

Downs et al. [28] took a different approach to the distributed roughness problem. Instead of using sandpaper roughness, they used rapid prototyping to create patches

of "random" roughness with a known streamwise and spanwise wavelength distribution. Hotwires measured the streamwise velocity both above and downstream of the roughness patches, and the decomposed velocity field indicated the presence of transient growth.

Direct numerical simulation of the Downs et al. [28] experiment by Drews et al. [29] and Drews [30] examined the flow downstream of distributed roughness patches. The DNS matched the experiments well and led to several interesting conclusions:

- Each roughness patch contained three peaks and surrounding smaller amplitude roughness. Examination of the near-wake region showed that the three peaks created the majority of the steady velocity disturbances downstream of the roughness.

- When the roughness valleys ($y < 0$) were replaced with a slip surface at $y = 0$, the flow downstream of the roughness was not strongly altered. This showed that the valleys play only a secondary role in receptivity.

- Removing all of the roughness except the three largest peaks *increased* the strength of the transient growth downstream of the roughness. This suggests that the presence of "foothills" affect the receptivity of larger roughness elements.

The findings of Drews [30] and Drews et al. [29] are consistent with the findings of Kendall [25] who placed a discrete element amongst a field of smaller-amplitude distributed roughness. The wake deficit of the discrete element in the distributed roughness case was three times smaller than in the smooth wall case. These experiments highlight the need to quantify receptivity of roughness "peaks" located in a field of distributed roughness.

The modal decomposition technique used by Denissen & White [23] is useful for quantifying the receptivity of surface roughness at a known location, but the extended streamwise length of distributed roughness complicates this approach. The steady and unsteady disturbances created by distributed roughness will be a combination of disturbances created at different streamwise locations, and each of these disturbances will undergo different amounts of growth over different length scales. One possible extension of modal decomposition to distributed roughness is a convolution integral:

$$\hat{u}_{\lambda_z}(x,\eta) = \int_{\alpha}\int_{x_0}^{x}\left[\frac{\partial C_\alpha}{\partial \xi} e^{i\alpha(x-\xi)}\hat{u}_{\alpha,\lambda_z}(\eta)\right] d\xi d\alpha + C.C. \tag{1.2}$$

Figure 1.3 sketches the setup of the convolution integral. In Eq. 1.2, the total velocity disturbance ($\hat{u}_{\lambda_z}(x,\eta)$) is a linear convolution of disturbances created at different locations on the rough surface (ξ). This approach assumes that the interactions between disturbances are linear, but the disturbance receptivity ($\partial C_\alpha/\partial\xi$) is not necessarily linear.

There are obviously some cases where a convolution integral approach would fail due to non-linear interaction between disturbances; for example, Denissen & White [23] showed that the near-wake of a cylindrical roughness element (less than two diameters downstream) could not be represented using modal decomposition due to a non-linear recirculation region. Despite this, linear superposition of roughness wakes may be applicable to cases with distributed roughness or small isolated roughness. Kendall [25] studied the streamwise interaction of two roughness elements with $Re_k = 45$ and only found a weak interaction. The "shielding" effect associated with distributed roughness may make a convolution integral approach appropriate; however, the streamwise interaction between discrete roughness elements - located amongst distributed roughness - needs to be studied in more detail.

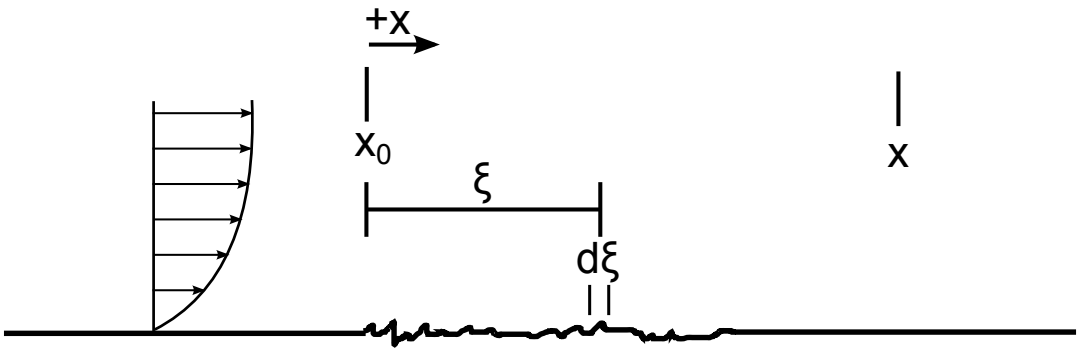

Figure 1.3: Sketch of receptivity at multiple streamwise locations

The goal of the research presented in this dissertation is to further study the shielding effect in order to better understand the receptivity of distributed and discrete roughness. Different roughness configurations (combinations of a deterministic distributed roughness patch and a discrete roughness element) were manufactured using rapid prototyping and placed flush with the wall within a flat plate boundary layer. Detailed hotwire scans, both above and downstream of the roughness, quantify the velocity in the boundary layer. The boundary layer profiles are decomposed into a basic state, a steady, spanwise modulation of the flow, and unsteady disturbances. The hotwire scans, in conjuncture with naphthalene flow visualization, provide insight into the receptivity of distributed and discrete roughness.

Section 2 of this dissertation describes the Klebanoff–Saric Wind Tunnel facility, which was used for this experiment. Section 3 describes the experimental setup (roughness design and the flat plate model) and defines the metrics by which the flow field is decomposed into transient growth quantities. Sections 4-6 present the results from the three different roughness configurations (distributed roughness, discrete roughness, and distributed & discrete roughness) that were chosen specifically to

study the shielding effect and roughness receptivity. Section 7 compares the results from the three roughness configurations, while Section 8 discusses the conclusions from this work and suggests what steps should be taken to further understand the links between surface roughness, transient growth, and boundary layer transition.

2. FACILITY DESCRIPTION - THE KLEBANOFF–SARIC WIND TUNNEL

The KSWT at Texas A&M University is a closed-loop, low speed, low disturbance wind tunnel designed for boundary layer stability and transition experiments. The KSWT, which was previously operational at the National Bureau of Standards and Arizona State University [31], was relocated to Texas A&M in 2005. The tunnel was reconstructed at Texas A&M with modifications to improve flow quality and decrease flow disturbance levels. A tunnel overhead view can be seen in Fig. 2.1. Hunt et al. [32] describes the KSWT in detail, presents freestream turbulence measurements at several points in the test section, and provides information about background sound levels in the tunnel.

2.1 Test Section

The test section is 4.9 m long and has a 1.4 by 1.4 m square cross section at the upstream end. The test section diverges slightly to account for boundary layer growth on the tunnel walls; the cross section at the downstream end of the test section is 1.41 m tall by 1.4 m wide. The test section rests on pneumatic isolating units (Fabreeka Precision-Aire PAL 21) that isolate the test section from building vibrations. The pneumatic isolators remove structural vibrations that induce velocity and acceleration biases in hotwire measurements. To avoid additional vibration transfer, the test section is connected to the rest of the tunnel with duct tape couplings. The test section also has interchangeable windows; one of the windows offers a large viewing area while another supports a three dimensional traverse for detailed hotwire scans.

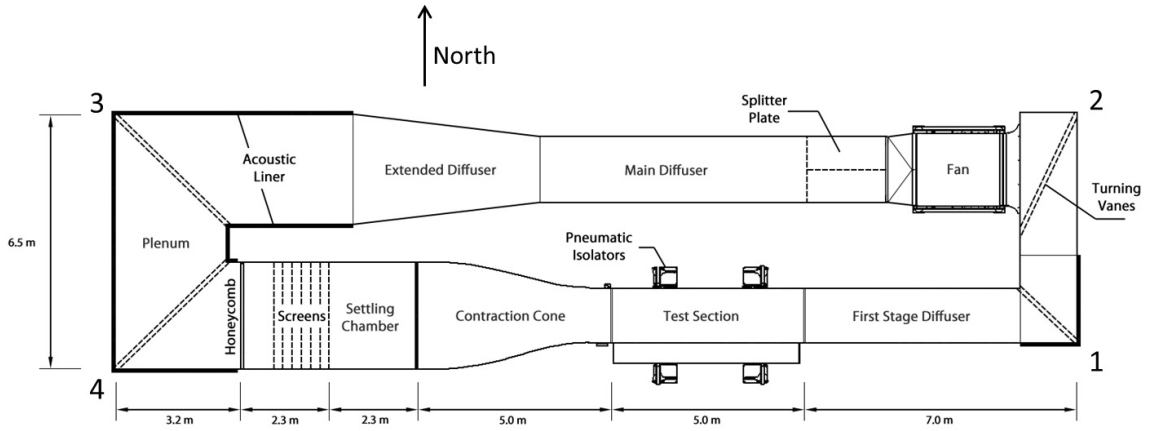

Figure 2.1: Overhead view of the Klebanoff–Saric Wind Tunnel

2.2 Fan and Motor

The tunnel is powered by an Emerson Industrial Controls 150 horsepower, variable speed 1750 maximum RPM direct current motor. The motor is connected to a Howden Buffalo nine-bladed, 6' diameter, adjustable-pitch axial fan through a belt drive system. With the fan installed, the maximum motor RPM is 1300. Eleven stators downstream of the fan remove fan-induced flow swirl. A nacelle and fairings surround the power transmission cartridge and drive belt, respectively. The fan sits inside of a metal housing that is not rigidly connected to any other part of the tunnel; flexible rubber couplings connect the fan housing at both the upstream and downstream ends. The fan housing is supported by the same steel structure that supports the motor. The motor sits directly underneath the fan housing, and the entire structure is surrounded by a plywood enclosure that is lined on the interior with egg crate acoustic foam.

In the current motor configuration, the maximum motor frequency is 21.7 Hz. The nine-blade fan produces blade passing noise at nine times the motor frequency with the maximum blade passing frequency (BPF) at 195 Hz. The tunnel is con-

trolled by adjusting motor RPM, so motor and blade passing frequencies change with test section speed and blockage.

2.3 Diffusers and Contraction Cone

The cross sectional area of the KSWT increases at three locations around its circuit: the main diffuser, the extended diffuser, and the first stage diffuser (see Fig. 2.1). The main diffuser and the extended diffuser have expansion angles of 12 degrees, while the first stage diffuser has an expansion angle of 10 degrees. Each diffuser has a full length splitter plate that halves the expansion and helps prevent unsteady separation bubbles. Two screens located in the main diffuser also promote attached flow. The contraction cone, located directly upstream of the test section, reduces the cross-sectional area of the tunnel by a factor of 5.33 and has an L/D of 1.25. The contraction is a fifth-degree polynomial shape with zero slope and zero curvature at both the upstream and downstream ends. The contraction cone is designed to prevent a separation bubble that can cause low frequency pressure oscillations.

2.4 Screens and Honeycomb

Several components along the test leg of the tunnel are specifically designed to lower turbulence levels. A sheet of aluminum honeycomb is located directly downstream of corner four. The honeycomb is made of hexagonal cells that are three inches long and 0.25 inch maximum width. The honeycomb is designed to straighten the flow and reduce large turbulence scales.

Seven tensioned screens, placed downstream of the honeycomb, promote mean flow uniformity and reduce turbulence scales. Each screen is made of 0.0065 inch diameter stainless steel wire arranged in a 30 wire/inch mesh. The screens are each separated by nine inches to allow spatial decay of disturbances between each screen.

The first three screens are butt welded while the final four are seamless to minimize additional disturbances added to the flow by the screens.

2.5 Acoustic Treatments and Active Noise Control

During the tunnel's reconstruction at Texas A&M, 37 Modex Broadband Panels from RPG Diffuser Systems were mounted in the plenum on the ceilings, walls, and floors. These panels are designed to eliminate sound in the 50 - 5000 Hz range. The main component of the panel is a thin steel plate backed with a sound absorbing spring material. Vibration and bending of the plate caused by acoustic pressure fluctuations are damped by the absorbing material. The plate and spring material are encased in a perforated metal casing that is only 4.25 inches deep; the small thickness makes these panels ideal for the space-constrained tunnel environment. The panels are placed near intersections of walls where the pressure fluctuations have the highest magnitude.

Dense, 4.25 inch thick open cell acoustic foam from dB engineering was installed around the acoustic panels. The thickness limits the frequency absorption range of the foam to greater than 150 Hz. Although lower frequencies are more important for receptivity experiments, the foam reduces overall noise while creating a flat tunnel wall between the panels and the foam.

Three acoustic panels and additional foam were installed in corner one. These treatments serve two purposes; first, they help remove upstream traveling fan and motor noise. Secondly, the acoustic treatments help remove downstream traveling noise from the test section and upstream traveling noise fron the fan and motor.

In addition to passive noise control treatments, an active noise control system was installed in the tunnel to remove upstream-traveling planar sound. The details of the active noise control setup are given by Kuester & White [33].

2.6 Traversing System

The KSWT includes a three-dimensional traverse designed for detailed boundary layer measurements in two- and three-dimensional boundary layers. The total travel of the traverse is 1300 mm in the x (streamwise) direction, 90 mm in the y (wall-normal) direction, and 180 mm in the z (spanwise) direction. Minimum steps are 12 μm in x, 1 μm in y and 2 μm in z. Typical boundary layer heights in this experiment vary from 5 to 10 mm, and velocity was measured at 40-70 points in the boundary layer using a hotwire. Movement of the traverse sting is automated using stepper motors for accurate positioning. The traverse sting is inserted into the flow through a slotted, movable plastic panel on the side of the test section. A pressure box surrounds the traverse to prevent flow entrainment through the access slot.

2.7 Tunnel Control and Data Acquisition

All measurements, including static pressure, dynamic pressure, tunnel air temperature, and hotwire signals are collected using three National Instruments USB data acquisition boards (Model USB-6211). Using three boards provides 24 differential analog inputs (-10 V to +10 V maximum range) for tunnel control and measurements. One of the boards is exclusively used to measure tunnel conditions (static pressure, dynamic pressure and temperature), while the other two boards are used for acquiring hotwire measurements. All aspects of tunnel control (motor rpm, data acquisition and traverse movement) are integrated in an in-house C++ routine initially created by Rob Downs and Brian Crawford. The code was later modified by Matt Kuester to include new boundary layer scan techniques that were implemented in this experiment. The control program uses static pressure, dynamic pressure and temperature information to set the motor RPM to maintain constant velocity, Reynolds number, or fan speed. The accuracy of the pressure transducers

and RTD allow velocity to be controlled to within ± 0.1 m/s.

2.8 Hotwire Anemometry

Constant temperature hotwire anemometry is the primary measurement technique used in this experiment. Dantec 55P15 hotwires (1.25 mm long, 5 μm diameter tungsten wire) are operated using an AA Labs anemometry system. The wires are operated at an overheat ratio of 1.8, while the gain and offset on the anemometer are set to maximize the range of the data acquisition system. The typical frequency response of the entire hotwire setup is 215 kHz, which is over an order of magnitude larger than the frequencies of interest in this experiment.

During a hotwire run, the data acquisition system collects data from two hotwires. One of the hotwires is in the freestream, while the second wire is located in the boundary layer. Both hotwires are calibrated daily using a non-linear King's Law fit according to the procedure described by White [34], which adjusts the hotwire output for changes in freestream temperature. During data analysis, the velocity measured by the boundary layer wire is normalized by the velocity measured by the freestream wire to remove the influence of very low frequency oscillations in the flow and account for small changes in freestream condition throughout a run.

The fluctuating velocity component from the boundary layer wire is measured by AC-coupling (1 Hz - 2.5 kHz with 30 dB gain for laminar boundary layers or 1 Hz - 5 kHz with 8-10 dB gain for turbulent boundary layers) the boundary-layer hotwire signal using a Kemo/Stewart VBF44 filter/amplifier. Although the primary quantity of interest in this experiment is the distortion of the mean flow due to the different surface roughness patterns, the fluctuating velocity component highlights regions of spatial inflection points in the flow and shows which areas of the flow are destabilized by the roughness.

3. EXPERIMENTAL SETUP AND PROCEDURE

This section describes the setup and execution of the experiment, from setup of the flat plate model in the KSWT to analysis of hotwire measurements. The section starts with a discussion of the flat plate model and the basic state boundary layer which is perturbed by the surface roughness. The second subsection describes the design and manufacturing of the roughness used in the experiment. The third subsection provides details about boundary layer hotwire scanning procedures. The section concludes with an explanation of the transient growth quantities that are calculated from the hotwire signals and the procedure to calculate the uncertainties associated with these quantities.

3.1 Brunswick Flat Plate Model

The roughness experiment is performed using the Brunswick flat plate; a diagram of the plate is shown in Fig. 3.1. The entire plate, including the flap, is 173.2 inches long and 53.3 inches wide. The plate is constructed with paper honeycomb covered in a 0.04 inch thick aluminum skin for a total thickness of 0.87 inches. The plate has a 13.5-inch-long elliptical leading edge and a trailing edge flap to control the leading edge stagnation point. The plate is polished to a surface finish of 0.32 μm rms to create a near-mirror finish. A flat plate was chosen for this experiment to create a near-Blasius boundary layer; this canonical base flow will allow the results from the experiment to be easily compared with theory and direct numerical simulations.

A rectangular hole was cut into the plate so different roughness configurations can be mounted flush with the plate surface. The hole is 9.0 inches by 11.0 inches and is located in the center of the plate, 33.4 inches downstream of the leading edge. The hole is located far enough upstream that turbulent wedges from the plate/wall

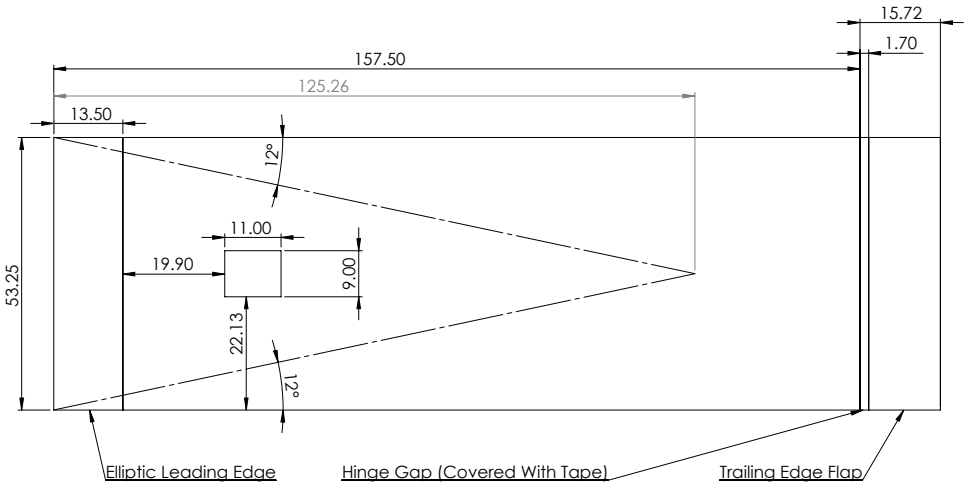

Figure 3.1: Brunswick flat plate (dimensions in inches)

intersection do not interfere with the experiment.

Different roughness configurations are tested by manufacturing roughness inserts and installing them in the hole in the plate. The roughness inserts are secured to a frame installed on the non-test side of the plate, and the insert is shimmed so the step between the top of the insert and the plate is less than 40 μm (as measured with a feeler gage). The gap between the insert and the plate is filled using Bondo to create a smooth interface between the plate and the roughness insert.

3.1.1 Streamwise Evolution of Basic State Boundary Layer

When the tunnel is set to a constant unit Reynolds number, a steady, near-zero pressure gradient boundary layer forms on the surface of the plate. Three different Reynolds numbers are used during this experiment in order to change the boundary layer height relative to the roughness height. Before preceding with measurements at a given Reynolds number, the boundary layer momentum thickness (θ) was measured using a hotwire at multiple streamwise locations. These measurements were made

at spanwise locations that are not affected by the surface roughness on the insert. A non-linear curve fit (Eq. 3.1) was then applied to define the boundary layer length scale (δ) over the entire plate.

$$\delta = \sqrt{\frac{x - x_{VLE}}{Re'}} = \frac{\theta}{0.664} \tag{3.1}$$

Figure 3.2 shows the x_{VLE}/Re' fit for all of the test conditions, while Table 3.1 lists the fit parameters and their associated uncertainties. The momentum thickness measurements and curve fit were performed for each Reynolds number, and the measurements were repeated when the second tunnel entry began. The distributed roughness only measurements (blue lines/symbols) were made in the first tunnel entry, while the discrete roughness only and combined roughness measurements (red lines/symbols) were performed during the second tunnel entry, later in the year. The Reynolds number for natural transition on this flat plate in this wind tunnel is greater than 2.4×10^6, so any transition observed in the experiment is associated with the roughness on the insert.

The presence of the discrete roughness during the second tunnel entry complicated the curve fit for δ. At the Middle Re' test condition, the roughness tripped the

Table 3.1: x_{VLE}/Re' fit parameters for each test condition

Roughness Configuration	Test Condition	Re', 1/mm	x_{VLE}, mm
Distributed	Low Re'	548.9 ± 3.2	125 ± 7
	Middle Re'	772.4 ± 4.0	77 ± 7
	High Re'	868.5 ± 7.7	144 ± 6
Discrete & Combined	Low Re'	544.3 ± 5.4	140 ± 11
	Middle Re'	690.5 ± 43.6	171 ± 45

boundary layer. Since the curve fit is only valid for a laminar, Blasius boundary layer, measurements could only be made over a limited streamwise domain where the boundary layer was not turbulent. The reduced number of points included in the fit increased the uncertainty of the fit parameters for this test condition. The uncertainties associated with each fit are incorporated into the uncertainty in Re_k for each roughness configuration, which is reported in Sections 4-6.

The same measurements used for the x_{VLE}/Re' fit are also used to evaluate the local pressure gradient. The shape factor of each boundary layer profile is computed and compared to the shape factor of a Blasius boundary (2.591). Boundary layers with a shape factor less than 2.591 are experiencing a favorable pressure gradient, while shape factors greater than 2.591 indicate an adverse pressure gradient. During the preliminary stages of the experiment, the plate was carefully aligned (using adjustable mounting brackets) to create a near-zero pressure gradient boundary layer.

Figure 3.3 shows the shape factor as a function of streamwise location for all of the test conditions. Because the shape factor is a very sensitive indicator of pressure gradient, the scatter of points at a single streamwise location can be large. In almost all of the cases, the mean shape factor at a streamwise location is 2.59 ± 0.05. At the location of the roughness, the boundary layer has a slightly favorable pressure gradient. Towards the downstream end of the measurement region, the pressure gradient becomes less favorable or slightly adverse. The shape factors from the first tunnel entry (blue dots) closely match the shape factors from the second tunnel entry (red squares).

3.1.2 Boundary Layer Spanwise Uniformity

In addition to the measurements at multiple streamwise locations, boundary layer scans were performed upstream of the roughness to evaluate the spanwise uniformity

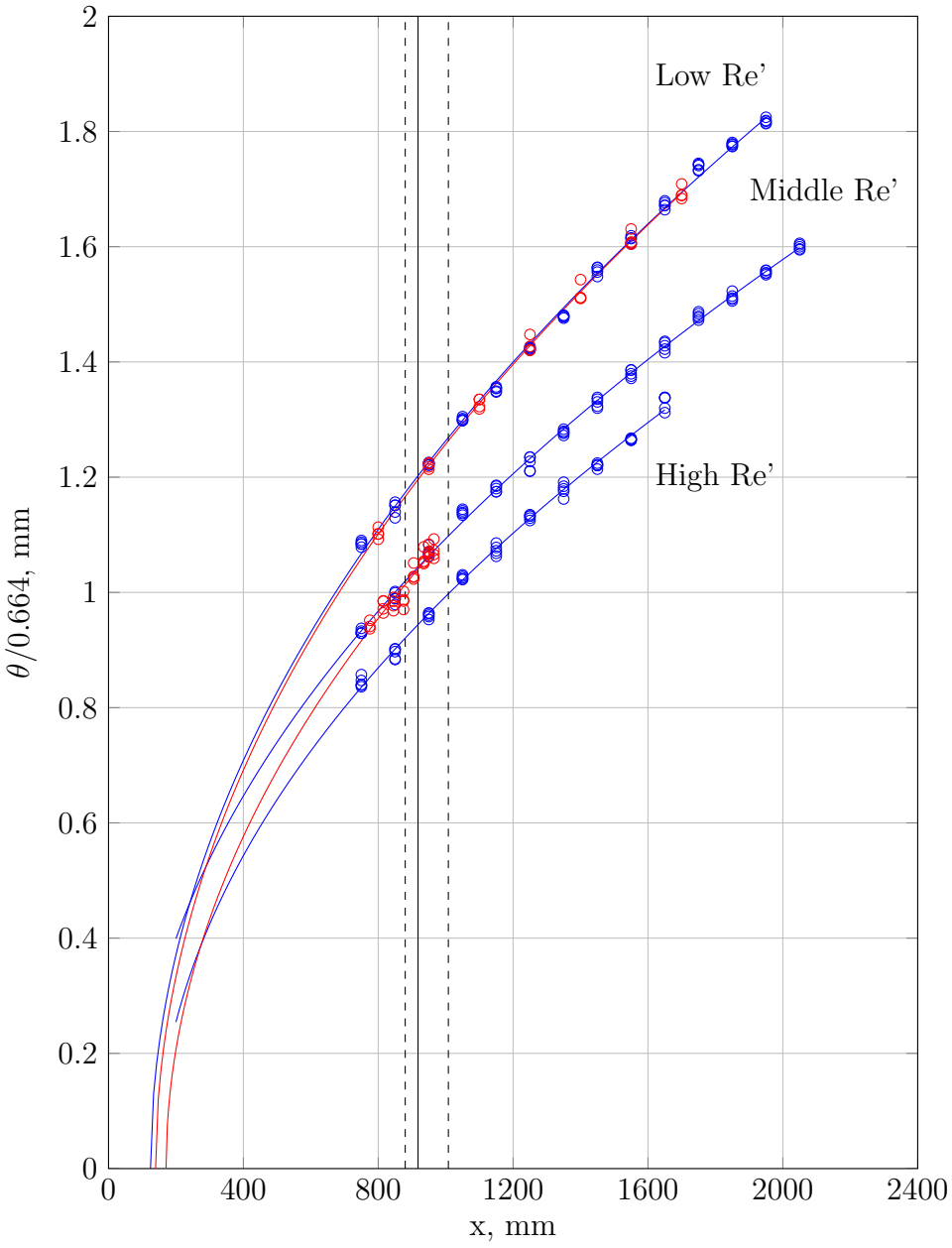

Figure 3.2: x_{VLE}/Re' fits for all test configurations. Blue circles represent measurements for the first entry (distributed roughness only), while red squares represent measurements for the second entry (discrete only & combined roughness). The solid black line shows the location of the discrete roughness element, while the dashed black lines show the location of the distributed roughness.

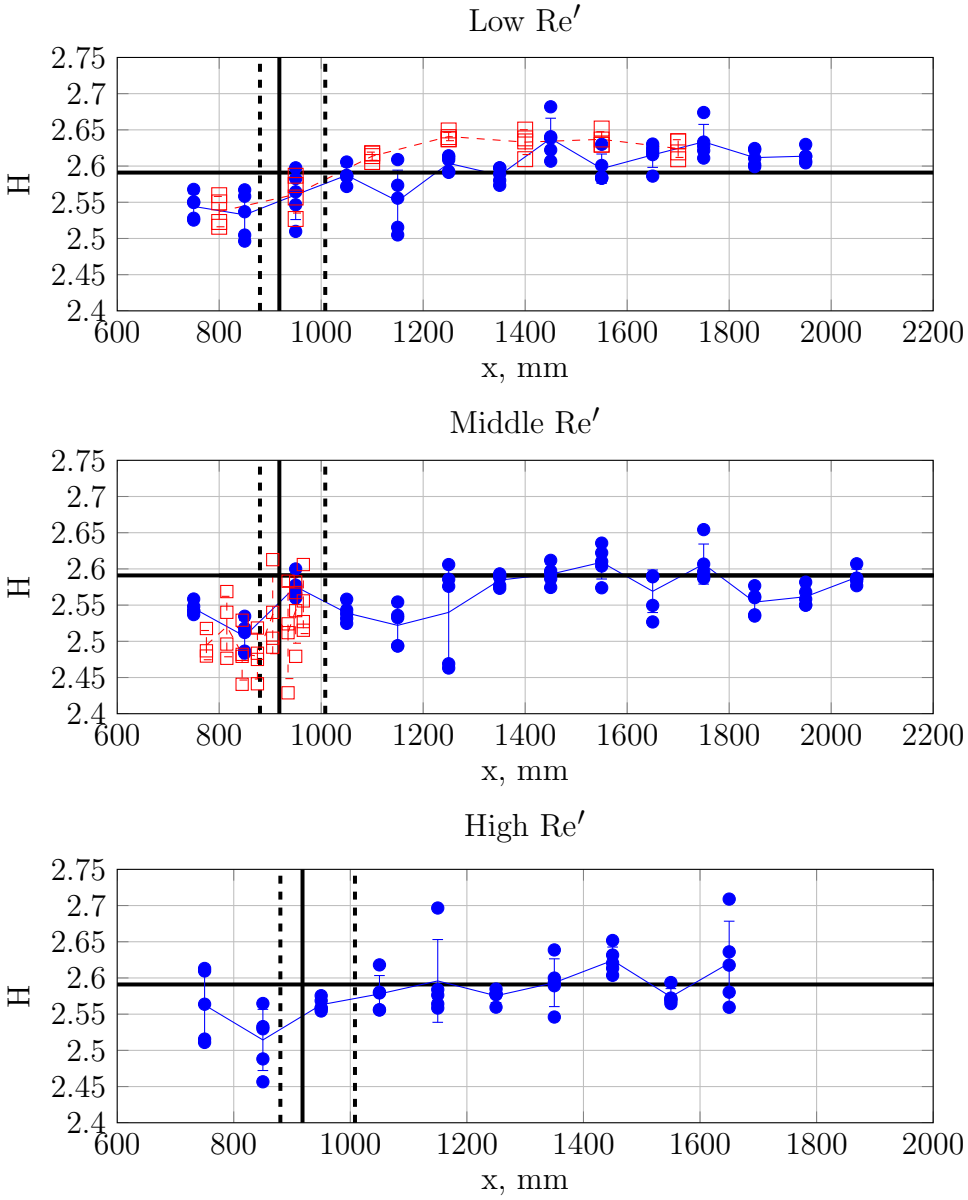

Figure 3.3: Boundary layer shape factor for the three different unit Reynolds number test conditions. The solid black line shows the location of the discrete roughness element, while the dashed black lines show the location of the distributed roughness. The horizontal black line shows the shape factor of a Blasius (zero pressure gradient) boundary layer. Symbols represent a measured boundary layer profile. Blue lines/circles are from the first test entry, red lines/squares are from the second test entry.

of the boundary layer. Ideally, the incoming boundary layer is perfectly uniform across the span. In reality, a number of factors, including the Bondo interfaces at the leading edge/plate junction and the leading edge of the roughness insert, create non-uniformity in the boundary layer upstream of the roughness.

Table 3.2 shows the spanwise mean and standard deviation of θ, δ^*, and H across the test region immediately upstream of the roughness for several of the test conditions/configurations. Figure 3.4 shows the spanwise variation of the basic state upstream of the roughness for one of the test configurations. In all of the configurations tested, the spanwise variations in θ, δ^* and H were less than 1.2%, with typical variations between 0.5% and 1.0%. The spanwise uniformity of the boundary layer upstream of the roughness reduces the patch-to-patch variability of the roughness wakes and increases the quality of the experiment.

Table 3.2: Boundary layer spanwise uniformity. The spanwise uniformity scan for the distributed roughness only and discrete roughness only roughness cases was performed at x = 870 mm, while the spanwise uniformity scan for the combined roughness case was performed at x = 865 mm.

Roughness Configuration	Test Condition	δ^*, mm	θ, mm	H
Distributed	Low Re'	1.978 ± 0.025	0.767 ± 0.006	2.579 ± 0.023
	Middle Re'	–	–	–
	High Re'	1.580 ± 0.024	0.613 ± 0.005	2.579 ± 0.034
Discrete	Low Re'	1.934 ± 0.022	0.760 ± 0.006	2.548 ± 0.023
	Middle Re'	–	–	–
Combined	Low Re'	1.853 ± 0.013	0.740 ± 0.005	2.503 ± 0.017
	Middle Re'	1.619 ± 0.024	0.650 ± 0.006	2.493 ± 0.028

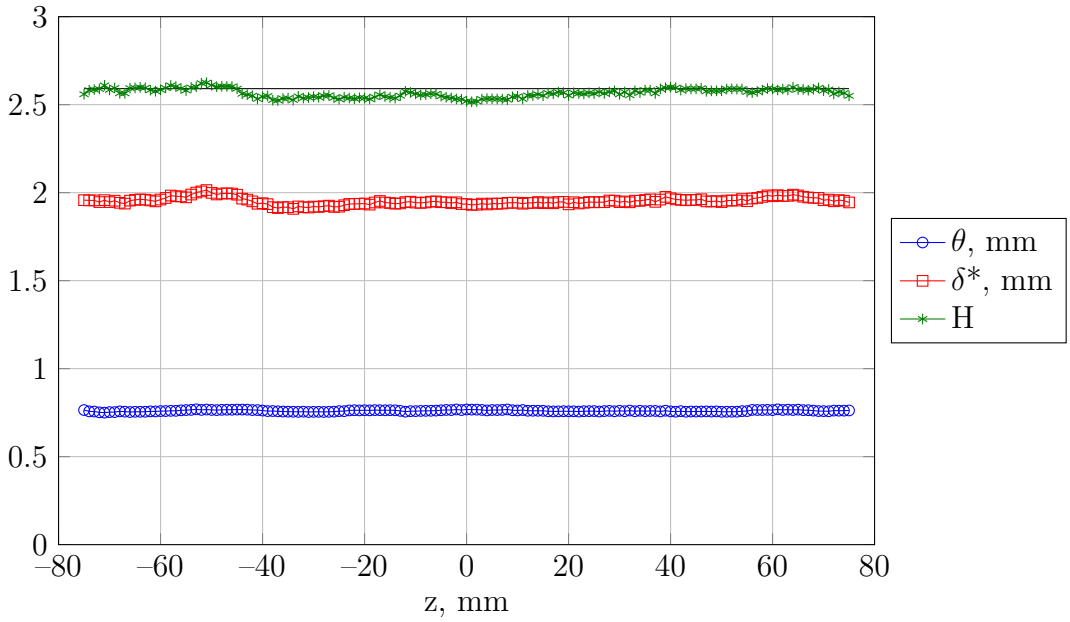

Figure 3.4: Spanwise uniformity of boundary layer integral quantities at x = 870 mm for low unit Reynolds number test condition with the distributed roughness configuration

3.1.3 Stagnation Point and Leading Edge Δp

The trailing edge flap on the model was deflected 8° to set the stagnation point on the test side of the plate to avoid leading edge separation. Figure 3.5 displays the differential pressure across the leading edge for different speeds and flap deflections; the positive Δp indicates that the stagnation point is on the test side of the plate.

3.1.4 Flow Angularity

Previous roughness-induced transient growth experiments have featured circular cylinder roughness elements, whose receptivity is not sensitive to flow angularity along the plate surface. In this experiment, the elongated patches of distributed roughness and non-symmetric discrete roughness dictate that flow angularity be measured and addressed.

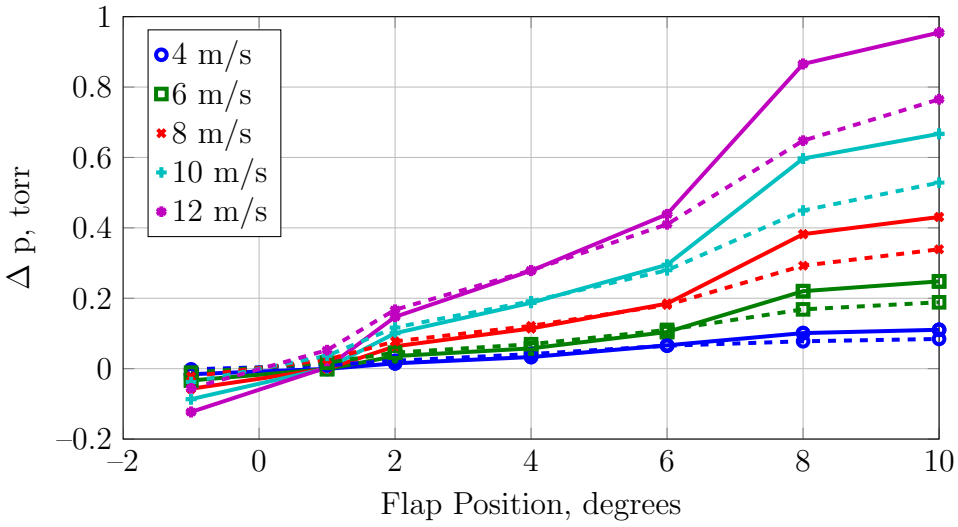

Figure 3.5: Differential pressure across the flat plate leading edge. Solid lines are measurements from the top pressure ports, while dashed lines are measurements from the bottom pressure ports.

Flow angularity along the plate surface was measured using two techniques. First, the laminar wake of a single cylindrical roughness element was visualized using naphthalene flow visualization. The wake was angled down 0.54° relative to the top of the roughness insert. Secondly, hotwire results from the second tunnel entry show that the wake of the discrete roughness elements is angled $\sim 0.3°$ relative to the traverse x-axis. These two results show that the flow angularity is small and most likely does not play a role in roughness receptivity for this experiment. The flow angularity is incorporated into the data analysis routines to make sure that the basic state boundary layer is defined at the appropriate spanwise location (in-between roughness wakes).

3.2 Roughness Design and Manufacturing

The roughness configurations utilized in this experiment are designed to have a known, manufacturable shape so the experimental setup could be duplicated using

direct numerical simulations. Three different roughness configurations (distributed roughness, discrete roughness, and combined roughness) were designed to investigate the "shielding" effect. The roughness was manufactured using rapid prototyping. Current and future work focuses on characterizing the as-built roughness in order to make high-quality comparisons between experiments and direct numerical simulations.

3.2.1 Distributed Roughness

The distributed roughness used in this experiment consists of a sum of cosine functions (see Eq. 3.2). The amplitudes ($A_{m,n}$) are selected from a normal distribution, while the phases ($\phi_{m,n}$) are selected from a uniform distribution on the interval [0,2π].

$$h(x,z) = \sum_{m=-M_r}^{M_r} \sum_{n=1}^{N_r} (\Delta(m,n))\, A_{m,n} \cos\left(\frac{2\pi n x}{\lambda_x} + \frac{2\pi m z}{\lambda_z} + \phi_{m,n}\right) \tag{3.2}$$

The roughness patch length (λ_x) is 128 mm, and the roughness patch width (λ_z) is 32 mm. The number of spanwise modes (M_r) is set to 10, while the number of streamwise modes (N_r) is set to 40. M_r and N_r are different by a factor of four because the length of the roughness patch is four times longer than the width of the patch. The amplitudes are weighted by the function $\Delta(m,n)$ (Eq. 3.3) to set the smallest roughness wavelength at $(0.0995)\lambda_z$. The weighting function also removes the purely streamwise roughness mode.

$$\Delta(m,n) = \begin{cases} 1 & \text{if } \left(\frac{n}{4}\right)^2 + m^2 \leq 10^2 + 1 \text{ and } m \neq 0 \\ 0 & \text{otherwise} \end{cases} \tag{3.3}$$

The roughness patch is then multiplied by a window function to create 8 mm

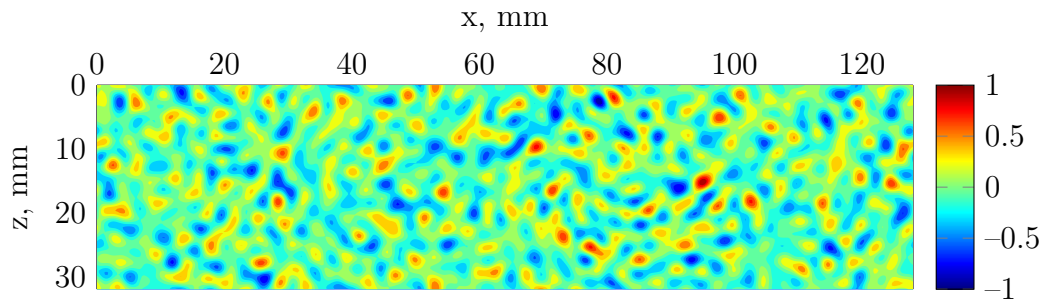

Figure 3.6: Roughness patch (k = 1 mm), before windowing

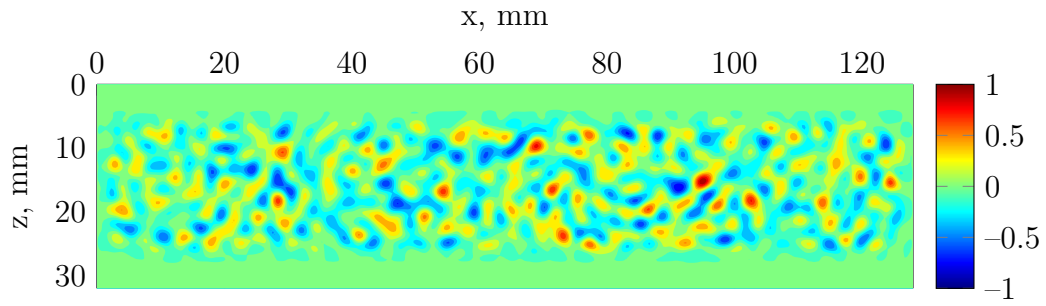

Figure 3.7: Roughness patch (k = 1 mm), after windowing

wide strips that run in the streamwise direction between roughness patches. These strips are used to locate the position of the wall during post-processing of hotwire scans. In addition to the roughness flats, the windowing function creates a 4 mm long cosine ramp into the "rough" section of the patch. Figures 3.6 and 3.7 show the pre- and post-windowed roughness patch.

The windowing function slightly alters the distribution of roughness wavelengths by introducing higher wavenumbers. Figure 3.8 shows the wavelength distribution of the roughness patch before the windowing function is applied, while Figure 3.9 shows the wavelength distribution of the final roughness patch. The largest amplitude roughness modes are shown in Table 3.3 (pre-windowing) and Table 3.4 (post-windowing).

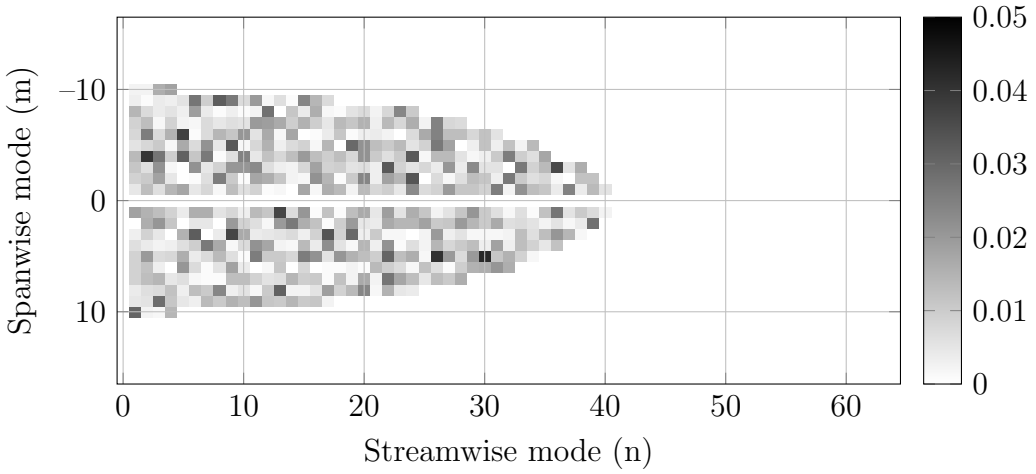

Figure 3.8: Roughness patch amplitudes (before windowing, k = 1 mm)

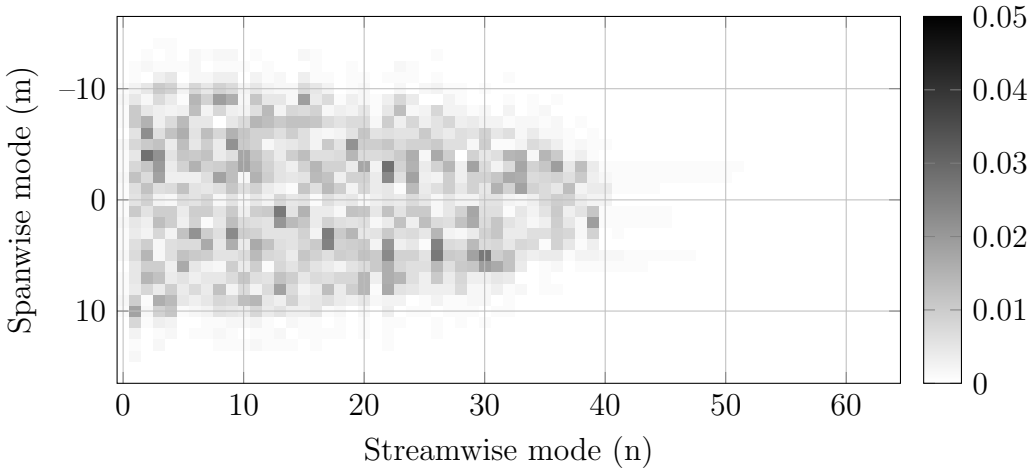

Figure 3.9: Roughness patch amplitudes (after windowing, k = 1 mm)

Table 3.3: Maximum roughness amplitudes (pre-windowing)

Spanwise Mode (m)	Streamwise Mode (n)	λ_z/m, mm	λ_x/n, mm	Normalized Roughness Amplitude
5	30	6.40	4.27	0.0418
5	26	6.40	4.92	0.0406
-4	2	-8.00	64.00	0.0393
-6	5	-5.33	25.600	0.0371
1	13	32.00	9.85	0.0363
3	9	10.67	14.22	0.0361
-3	36	-10.67	3.56	0.0353
-2	24	-16.00	5.33	0.0332

Table 3.4: Maximum roughness amplitudes (post-windowing)

Spanwise Mode (m)	Streamwise Mode (n)	λ_z/m, mm	λ_x/n, mm	Normalized Roughness Amplitude
-3	22	-10.67	5.81	0.0280
-4	2	-8.00	64.00	0.0280
5	30	6.40	4.27	0.0265
1	13	32.00	9.85	0.0263
5	26	6.40	4.92	0.0258
3	17	10.67	7.53	0.0250
4	26	8.00	4.92	0.0245
4	17	8.00	7.53	0.0243

3.2.2 Discrete Roughness

Dr. David Goldstein and his research group at UT Austin, who are performing immersed boundary direct numerical simulations (DNS) to match this experiment in the KSWT, helped drive the design of the roughness element. Earlier simulations of

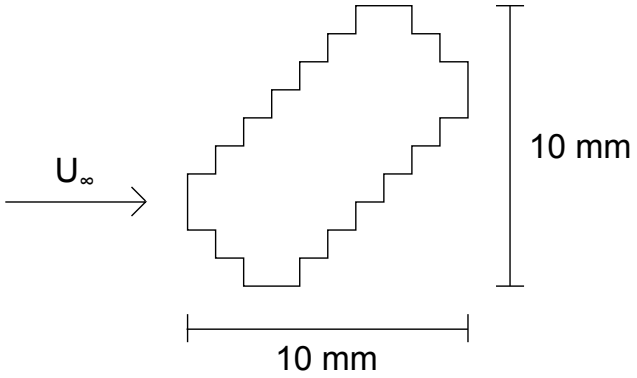

Figure 3.10: Top view of discrete roughness element

the flow around a circular-cylinder roughness element by Stephani & Goldstein [20] and Drews [30] showed that the symmetric circulation region downstream of the roughness element required prohibitively long run times to achieve a converged result. To prevent a symmetric circulation region, a slanted rectangle roughness design was chosen.

An overhead view of the roughness element is shown in Fig. 3.10. The rectangle is 10 mm long, 5 mm wide, and oriented at a 45° angle relative to the incoming flow. The edges of the rectangle are defined on a 1 mm × 1 mm grid so the geometry can easily be implemented in an immersed boundary DNS.

3.2.3 Combined (Distributed + Discrete) Roughness

The final roughness configuration is a combination of the distributed roughness patch and the discrete roughness element. Figure 3.11 shows this combined roughness configuration. The shape of the discrete roughness element is extruded up from the distributed roughness surface to create the discrete, angled rectangle in the middle of the distributed roughness patch.

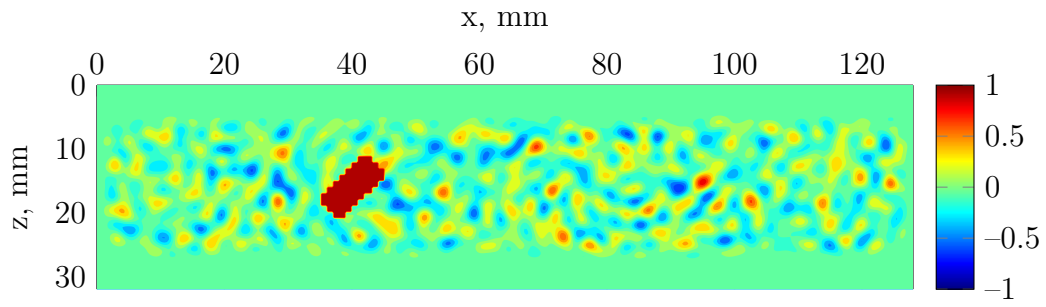

Figure 3.11: Combined roughness configuration ($k_{discrete}$ = 1.00 mm, $k_{distributed}$ = 0.85 mm)

3.2.4 Roughness Inserts, Roughness Manufacturing & Roughness Characterization

Three different roughness inserts were manufactured to test combinations of distributed and discrete surface roughness. The first insert featured two sets of three distributed roughness patches. The two sets of patches have the same geometry but different amplitudes. Multiple patches were placed side-by-side in the spanwise direction so measurements could be phase-lock averaged in span; however, only the inner two patches in each set could be reached with the hotwire traverse. Initially, the third patch was going to be reached using an additional hotwire holder that mounted to the sting; however, the hotwire holder created an upstream pressure effect that was interfering with measurements. For this reason, the additional hotwire was not utilized.

After the first tunnel entry, the design of the inserts was re-evaluated. Instead of featuring two sets of three roughness patches, the second (discrete roughness only) and third (combined roughness) inserts featured seven identical patches side-by-side in the spanwise direction. The traverse has enough throw in the spanwise direction to reach four of the roughness patches with this configuration. Increasing the number of roughness patches also increased the quality of the data by allowing for additional

spanwise averaging. Table 3.5 shows the amplitudes and streamwise locations of the different roughness configurations when installed in the plate, while Figs. 3.12, 3.13, and 3.14 show the manufactured roughness inserts.

Table 3.5: Distributed and discrete roughness heights

Roughness Type	Roughness Location, mm	k, mm
Distributed (Low A)	878–1006	0.60
Distributed (High A)		0.85
Discrete	918	1.00
Combined (Discrete / Distributed)	918 / 878–1006	1.00 / 0.85

All of the roughness used in this experiment was manufactured using rapid prototyping (RP). The inserts were made on a Stratasys Fortus 400mc machine. The machine lays down RP material in spanwise slices to build up the part. The distributed roughness only insert was made using 0.254 mm layers, while the discrete roughness and combined roughness inserts were made using 0.178 mm layers. Stylus profilometer measurements, shown in Fig. 3.15, show that the surface roughness of the RP material is 20-30 μm rms. Measurements in the spanwise direction show a predominant wavelength corresponding to the layer height with approximately 13 μm rms amplitude. A similar measurement in the streamwise direction shows a predominant wavelength (between 2.2 and 5.0 mm long, depending on the which insert was measured) with approximately 9 μm rms; this wavelength is related to how support material is laid while the part is being constructed. Because of the thick boundary layers used in this experiment ($\delta \sim 1.0$ mm), this streamwise wavelength is too short to serve as a receptivity mechanism for unstable T–S waves.

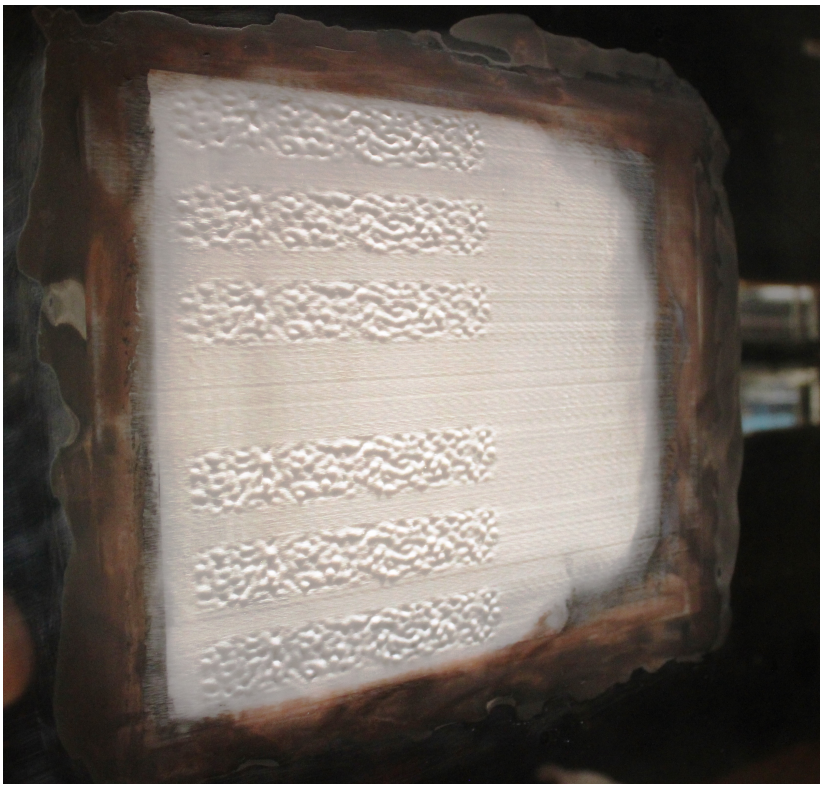

Figure 3.12: Distributed roughness only insert installed in the flat plate model. Flow travels from left to right.

Figure 3.13: Discrete roughness only insert. Flow travels from left to right.

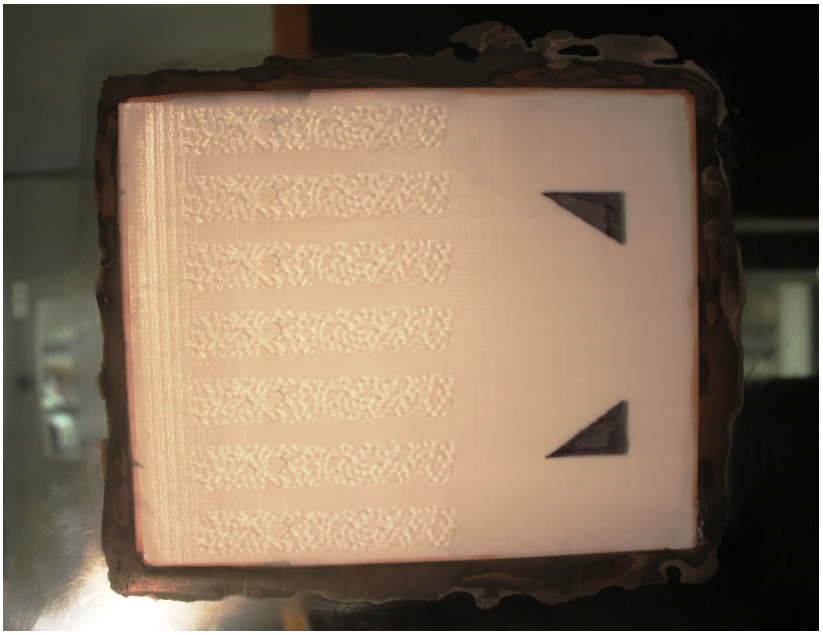

Figure 3.14: Combined roughness insert installed in the flat plate model. Flow travels from left to right.

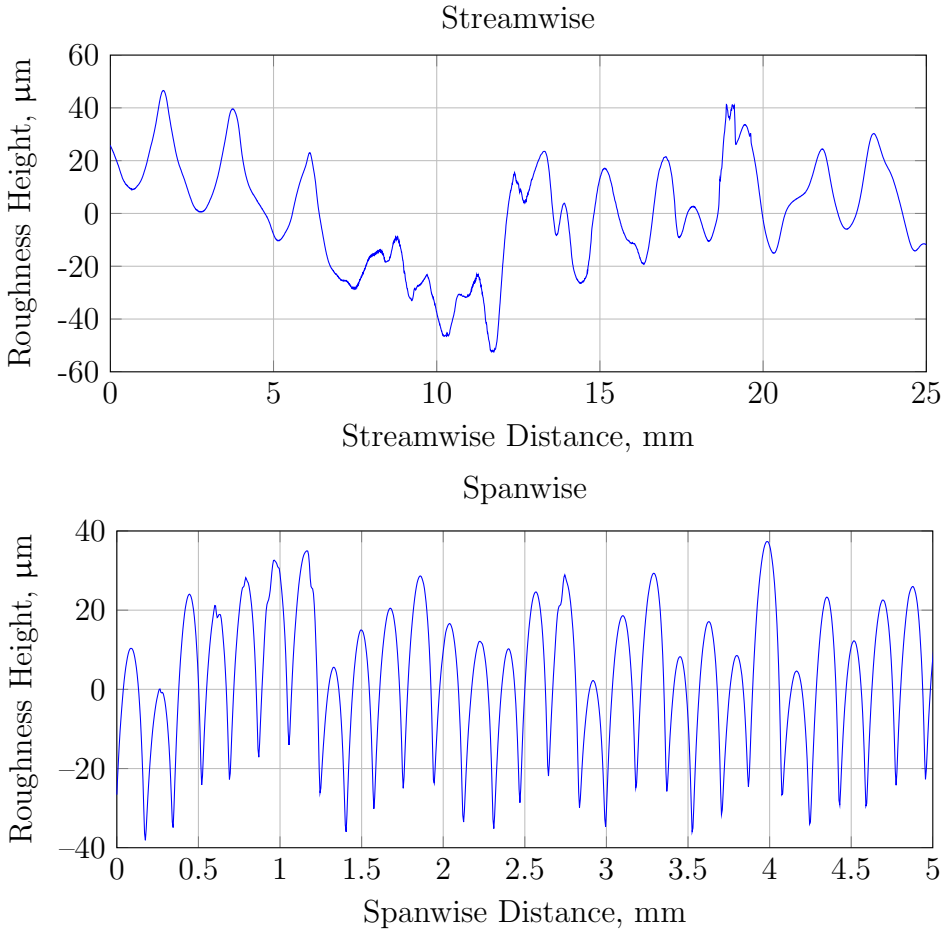

Figure 3.15: Surface roughness profiles of RP material in the streamwise (top) and spanwise (bottom) directions

In order to make high quality comparisons between DNS data and experiments, the roughness used for the wind tunnel experiments should be characterized. Characterizing the as-built roughness allows for a direct comparison between the roughness used in the wind tunnel experiment and the roughness implemented in a direct numerical simulation via an immersed boundary technique.

The roughness used in this experiment is too large to be measured by a typical stylus profilometer, and the RP material is too shiny to obtain accurate results using a laser profilometer. The one remaining tool available for characterizing the roughness

is a Mitutoyo Coordinate Measuring Machine (CMM) at the Oran W. Nicks Low Speed Wind Tunnel, located next door to the KSWT. The machine consists of a small-tipped stylus attached to a computer controlled traverse. The stylus is moved to a specified (x,z) location and then moved towards the roughness until the stylus comes in contact with the model.

The CMM was used to characterize the smaller amplitude distributed roughness patch ($k_{distributed}$ = 0.60 mm), and the results are shown in Fig. 3.16. Over 12000 data points were collected and compared to the as-designed roughness patch. The results show that the rapid prototyping machine accurately makes the roughness to within a 50 μm standard deviation with a maximum measured deviation less than 200 μm. The figure also shows that the predominant streamwise wavelength inherent to the RP material is responsible for a large portion of the manufacturing error.

Future work will focus on further characterization of the distributed and discrete roughness. A set of higher resolution measurements will provide details of how the rapid prototyping machine smooths out the edges of the roughness, while sparser scans over the entire insert will investigate any warping or large scale deformations in the roughness sheet.

3.3 Hotwire Scan Procedure

The primary measurement technique used in this experiment was hotwire anemometry. A hotwire scan consists of multiple boundary layer profiles, each measured at a different spanwise location. Each boundary layer profile is measured by starting the hotwire probe in the freestream and moving the probe towards the wall. The probe is stopped at discrete heights in the boundary layer to acquire data for a set amount of time (1.2 s for a laminar boundary layer, 2.0 s for a turbulent boundary layer) and then moved further towards the wall. The size of the step size is determined using

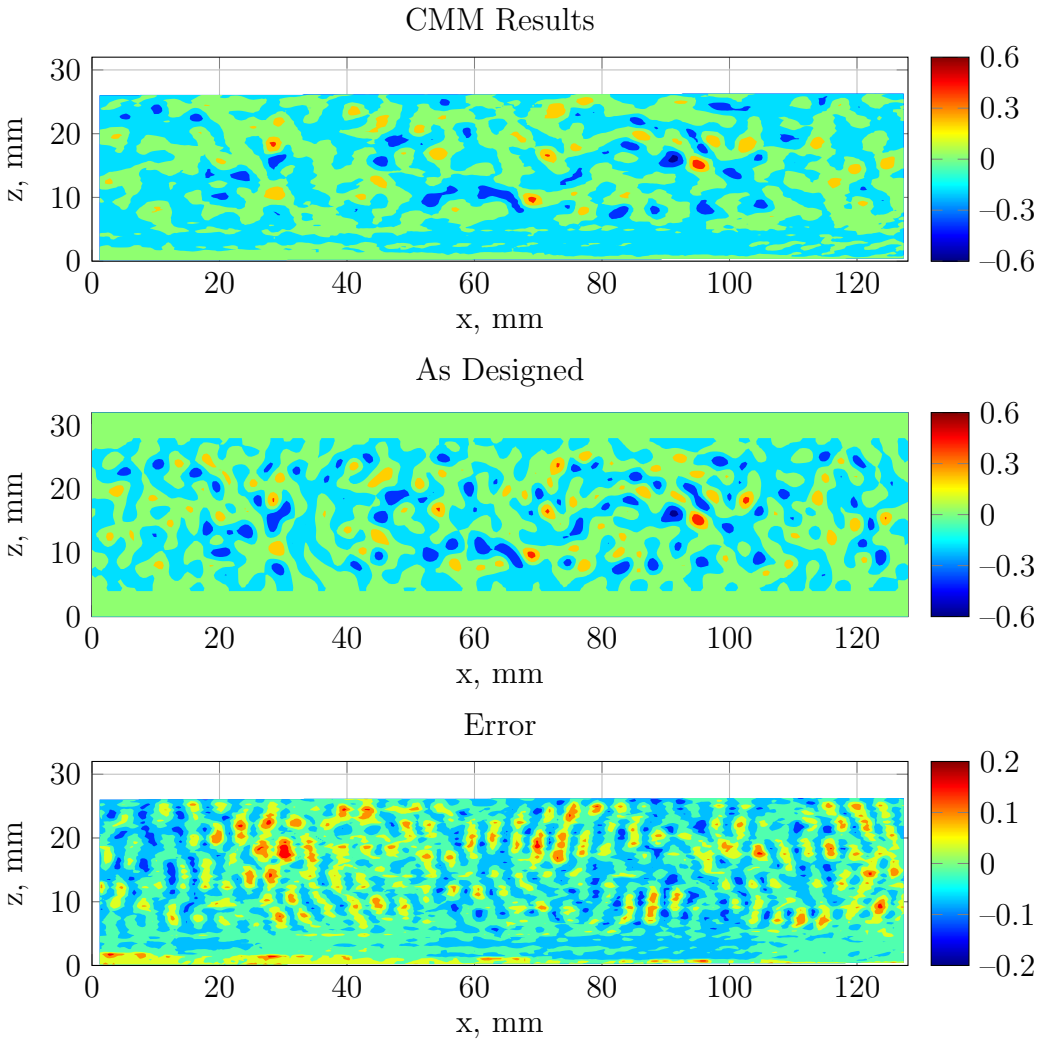

Figure 3.16: Coordinate measuring machine (CMM) results for the 0.60 mm distributed roughness patch. Units are in mm.

Eq. 3.4.

$$\Delta y = -(\Delta y)_0 \left(\frac{U_y}{U_e}\right)^{1.5} \tag{3.4}$$

In Eq. 3.4, U_y is the velocity measured in the boundary layer, U_e is the velocity at the edge of the boundary layer, and $(\Delta y)_0$ is the initial step size towards the wall. For most of the boundary layer scans, $(\Delta y)_0$ is defined using Eq 3.5.

$$(\Delta y)_0 = 0.3561\sqrt{\frac{x - x_{VLE}}{Re'}} \tag{3.5}$$

The profile is stopped when U_y/U_e drops below a cutoff value. For scans of laminar boundary layers downstream of the roughness field, this cutoff is 10%. When a scan is over distributed roughness, the hotwire is brought as close as possible to the roughness without running the wire into the wall; this leads to velocity cutoffs between 16% and 25%. When turbulent boundary layers are being measured, the cutoff is set between 25% to 30% due to the thinness of the laminar sublayer. After the profile is stopped, the probe is moved back to the starting position. The probe is then moved 1 mm in span, and the next boundary layer profile is measured. This procedure continues until a set number of spanwise locations have been measured (65 for the distributed roughness only configuration and 129 for the discrete roughness only and combined roughness configurations.)

Each profile typically starts 5 mm outside of the boundary layer. When a scan occurs over distributed roughness or includes turbulent profiles, the "small step size" option is activated. While operating in this mode, the program will automatically switch to 10 μm steps when the normalized velocity drops below a set threshold. This velocity threshold is set 3-6% higher than the cutoff velocity. This feature ensures

that data is collected in the near-wall region without taking large step sizes, which could lead to a collision between the hotwire and the surface.

Each hotwire measurement corresponds to a particular (y,z) location in the traverse coordinate frame. During a hotwire run, the exact location of the wall is not known, which is why a velocity cutoff is utilized. The transformation from the traverse coordinate system to the wall coordinate system takes place during post-processing using a technique developed by White & Ergin [35].

The location of the wall is estimated at selected spanwise locations by assuming a linear boundary layer profile in the near-wall region and extrapolating the profile to the y value where U = 0. This extrapolation is performed in (or downstream of) the roughness flats, where the flow is least disturbed by the roughness. An example of this wall extrapolation is shown in Fig. 3.17.

During the second tunnel entry, a new feature was added to the control program which lowers the velocity cutoff to a lower value (typically 10%) in the roughness flats where a higher velocity cutoff is not required. This helps to eliminate bias error from estimating the wall location using measurements far away from the wall. Appendix A lists the test matrices from the experiment, which include information about velocity cutoffs, small step size cutoffs, and roughness flat locations/cutoffs.

A parabolic spanwise fit is then applied to the extrapolated wall locations; an example fit is shown in Fig. 3.18. The spanwise fit allows the wall location to be defined at spanwise locations where y_{wall} cannot be estimated using extrapolation. The spanwise fit also removes any scatter in the data while accounting for any misalignment between the traverse and the wall.

The presence of surface roughness complicates the definition of the wall location. In this work, the location of the wall is defined as y = 0. Below the velocity cutoff, each velocity profile is interpolated linearly to the location of the wall (U = 0 at

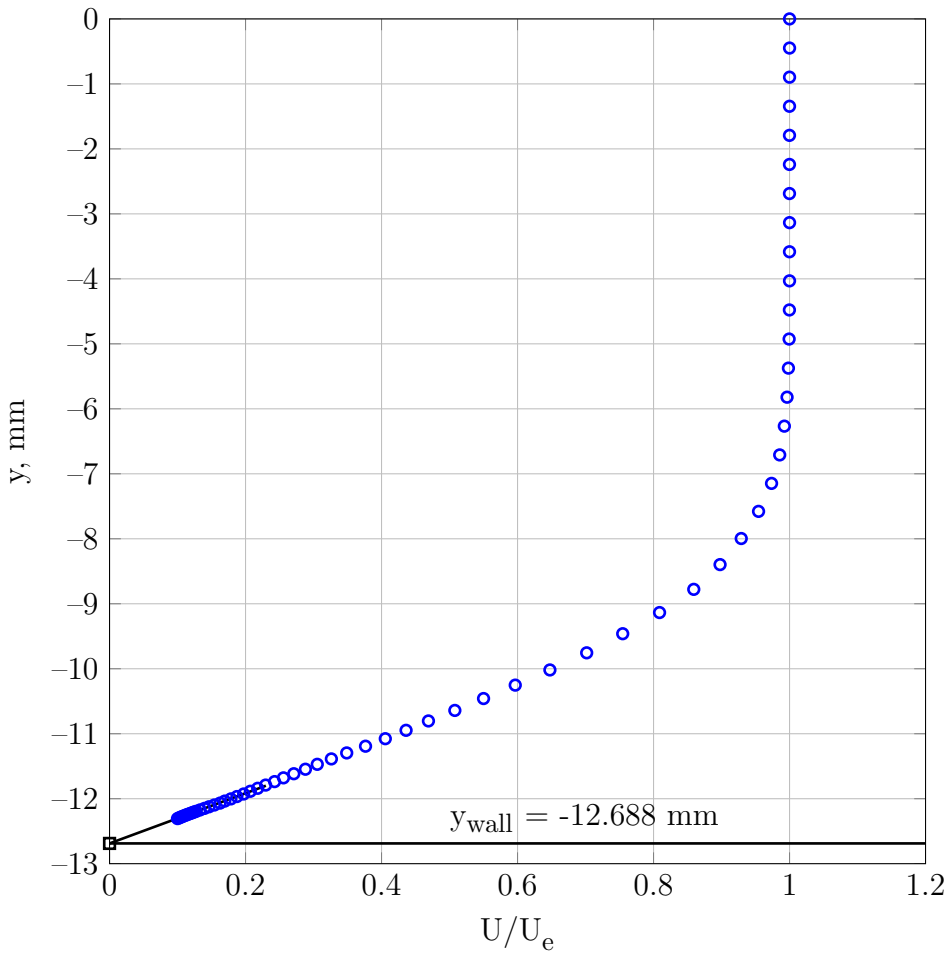

Figure 3.17: Sample wall extrapolation. Boundary layer profile measured at x = 1000 mm, in between roughness patches.

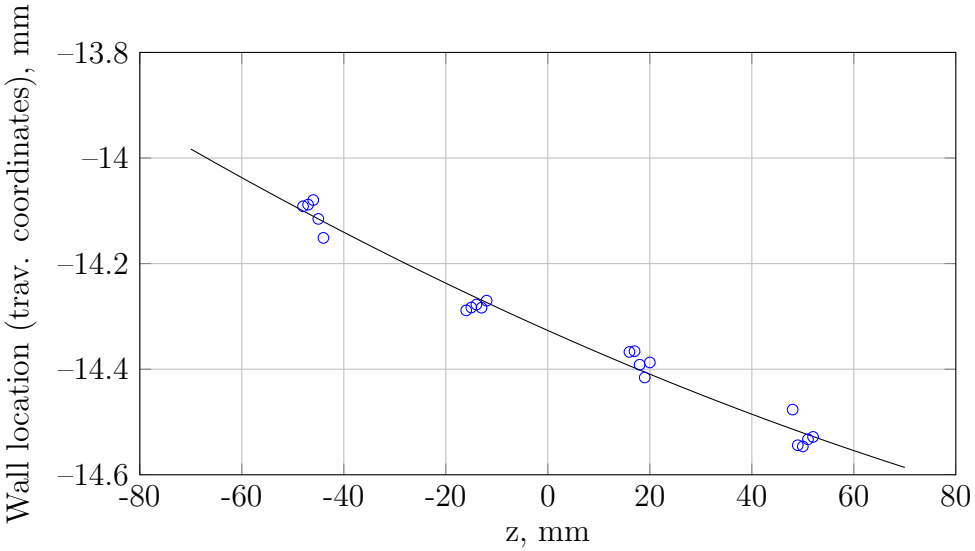

Figure 3.18: Spanwise wall fit for discrete roughness only configuration, low Reynolds number condition at x = 1500 mm.

y = 0). In actuality, the no-slip/no-penetration condition occurs at y = h(x, z), where h(x, z) represents the roughness topography. Resolving this discrepancy and finding a way to incorporate the non-zero wall location while characterizing the flow over distributed roughness is a challenging problem that needs to be addressed in future distributed roughness receptivity experiments.

Boundary layer scans were performed at multiple streamwise locations (between 12 and 22) for each roughness configuration tested. The measurements at different streamwise locations show how the transient growth energy spatially evolves above and downstream of the roughness.

3.4 Data Analysis

The majority of the analysis in this dissertation focuses on steady velocity disturbances. For most of the different configurations/conditions tested, the roughness creates a laminar wake which consists of high- and low-speed streaks in the lower

portion of the boundary layer. These streaks are quantified by defining a basic state boundary layer (the steady boundary layer that exists without the effect of roughness) and evaluating how the streaks perturb the boundary layer from this basic state.

The basic-state profile $U_c(y)$ is calculated by averaging the profiles that are in-between or downstream of the flats between roughness patches; these are the same profiles that are used to extrapolate the location of the wall. This average profile should be the least affected by the roughness and most indicative of the undisturbed boundary layer. The flow behind the roughness patches is then phase-locked averaged across the span to create a representative flow field ($U(y,z)$) downstream of a single roughness patch. For the distributed roughness results, the representative flow field is the average of two roughness wakes. For the discrete roughness and combined roughness configurations, the representative flow field is the average of four roughness wakes.

The steady boundary-layer disturbance field (Eq. 3.6) is defined as the deviation from the basic-state normalized by the edge velocity.

$$U'(y,z) = \frac{U(y,z) - U_c(y)}{U_e} \tag{3.6}$$

The root-mean-square of the steady-disturbance profiles ($U'_{rms}(y)$) is taken in the spanwise direction to quantify how the boundary layer has been distorted by the surface roughness. The total disturbance energy is then defined as

$$E_{dist} = \frac{1}{\delta}\int_0^\infty U'_{rms}(y)^2 dy \tag{3.7}$$

where δ is defined by Eq. 3.1. δ is defined locally at each streamwise location and

changes as the boundary evolves in the streamwise direction.

In addition to the total disturbance profile, individual roughness wavelengths are also analyzed. Because the disturbance field is phase-lock averaged in span, we assume that the disturbance is periodic along the primary roughness wavelength ($\lambda_z = 32$), and thus, a Discrete Fourier Transform (DFT) is appropriate (shown in Eq. 3.8).

$$B\left(y, \lambda_k/m\right) = \frac{1}{32}\sum_{j=0}^{31} U'(y, z_j)e^{-2\pi i z_j m/\lambda_k} \tag{3.8}$$

In Eq. 3.8, $z_j = j(\Delta z)$. Boundary layer profiles are acquired every 1 mm in span, so the Fourier Transform is performed over 32 points. The disturbance profile associated with a particular spanwise wavelength (Eq. 3.9) is then calculated by evaluating the amplitude of the DFT at the given height in the boundary layer. The normalization factor in Eq. 3.9 includes Kronecker deltas in order to satisfy Parseval's theorem.

$$U'_{rms}(y, \lambda_k/m) = \sqrt{(2 - \delta_{m(0)} - \delta_{m(16)})B\left(y, \lambda_k/m\right) B^*\left(y, \lambda_k/m\right)} \tag{3.9}$$

The disturbance energy at a particular wavelength (Eq. 3.10) is then calculated by integrating the squared rms velocity profile associated with that wavelength in the wall-normal direction.

$$E_{\lambda_k/m} = \frac{1}{\delta}\int_0^\infty \left(U'_{rms}(y, \lambda_k/m)\right)^2 dy \tag{3.10}$$

As a consequence of the normalization of $U'_{rms}(y, \lambda_k/m)$ and $E_{\lambda_k/m}$, the total disturbance energy is equal to the sum of the disturbance energies in each of the

integer modes:

$$E_{dist} = \sum_{m=0}^{16} E_{\lambda_k/m} \tag{3.11}$$

3.5 Uncertainty Analysis

The uncertainty analysis of hotwire measurements is a key part of this dissertation. The steady velocity disturbances measured in this experiment are small. On top of this, the differences in the flow downstream of different roughness configurations can be even smaller than the disturbance itself. Quantifying the uncertainty associated with these measurements provides a way to compare different roughness configurations and determine if the difference in the flows is statistically significant. Quantifying the uncertainty in the transient growth disturbance profiles and energies will also allow for meaningful comparisons between this experiment, DNS, and theory.

Initially, Monte Carlo simulations were used to simulate different hotwire calibrations and wall location fits based on the covariance matrices of these fits. These results showed that the uncertainty in the transient growth quantities due to hotwire calibration and wall finding was small compared to patch-to-patch variability in the flow downstream of each periodic roughness patch. To this end, further attempts to quantify the uncertainty in these measurements have focused on the patch-to-patch variability.

The starting assumption of the uncertainty analysis is that the velocity at each point in the averaged flow field ($U(y,z)$) is assumed to be part of a normal distribution of possible points. The flow field downstream of each roughness patch is one realization in this distribution, so we measure two (distributed roughness only) or four (discrete roughness only and combined roughness configurations) realizations of

this distribution. Under this assumption, we can express the uncertainty in the mean of our measurements (the steady velocity disturbance that we are interested in) by calculating the standard error of the population sample; this is shown in Eq. 3.12.

$$\sigma_{U'(y,z)} = \sqrt{\frac{1}{N}\frac{\sum_{j=0}^{N-1}(U'_j(y,z) - U'(y,z))^2}{N-1}} \tag{3.12}$$

In Eq. 3.12, N is the number of roughness wakes that are measured, and $U'_j(y,z)$ is the steady velocity disturbance field created by roughness patch j. The uncertainty in $U'(y,z)$ can be propagated through the equations to find the variance associated with $U'_{rms}(y)$. This variance, shown in Eq. 3.13, quantifies the uncertainty of the total disturbance profile.

$$\sigma^2_{U'_{rms}(y)} = \left(\frac{1}{32}\frac{1}{U'_{rms}(y)}\right)^2 \sum_{i=0}^{31}\left(U'(y,z_i)\right)^2\left(\sigma_{U'(y,z_i)}\right)^2 \tag{3.13}$$

Figure 3.19 shows an example U'_{rms} disturbance profile with error bars calculated using Eq. 3.13. The red lines in Fig. 3.19 show the disturbance profiles of each roughness wake calculated individually; because this measurement was made in the wake of the discrete roughness elements, four red profiles are shown. The uncertainty at each point was modeled using a normal distribution, but Fig. 3.19 shows that the error associated with U'_{rms} is not random in the wall-normal direction. Some of the disturbance profiles are consistently larger than the average profile, while some of the profiles are consistently smaller.

To better capture this bias in the integrated disturbance energies, the normal distribution is not propagated through the wall-normal integration step. Instead, upper (Eq. 3.14) and lower (Eq. 3.15) uncertainty bounds are placed on the energies by introducing a positive or negative bias before integration. This procedure pro-

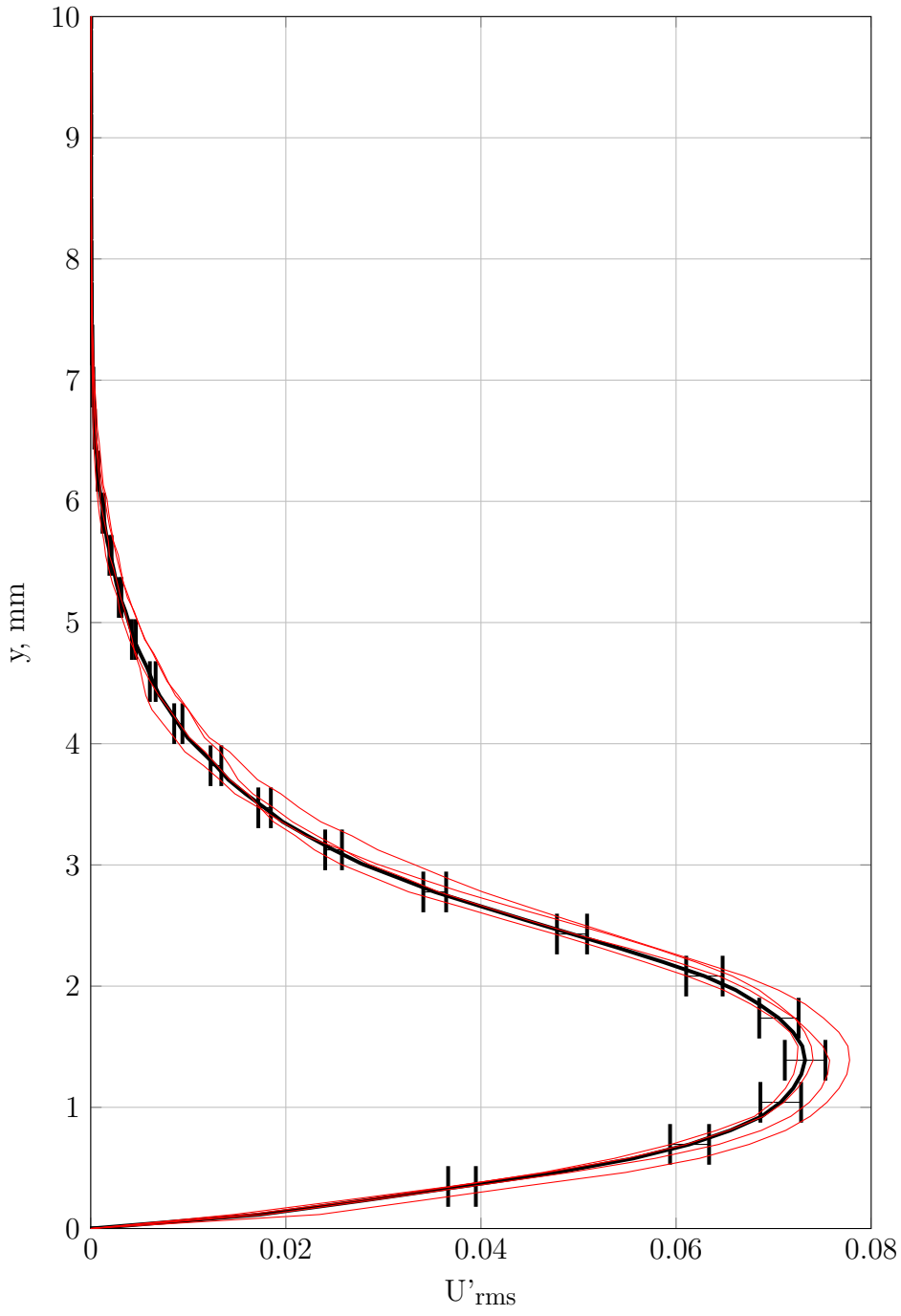

Figure 3.19: Total disturbance profile (U'_{rms}) for the discrete roughness only configuration, low Reynolds number condition at x = 1000 mm. The black lines represent the averaged disturbance profile, while the red lines show the disturbance profiles of the wake behind each roughness patch is analyzed individually.

duces uncertainties that are representative of the data quality and give numerical significance to the results based on the patch-to-patch variability of the flow field.

$$E^{+}_{dist} = \frac{1}{\delta}\int_0^{\infty}(U'_{rms}(y) + \sigma_{U'_{rms}(y)})^2 dy \tag{3.14}$$

$$E^{-}_{dist} = \frac{1}{\delta}\int_0^{\infty}(U'_{rms}(y) - \sigma_{U'_{rms}(y)})^2 dy \tag{3.15}$$

A similar procedure is used to calculate the uncertainties associated with disturbance profiles and integrated energies at individual spanwise wavelengths. The variance associated with the Fourier coefficient ($\sigma^2_{B(y,\lambda_k/m)}$, shown in Eq. 3.16) can be calculated by propagating the uncertainty associated with $U'(y,z)$ through Eq. 3.8.

$$\sigma^2_{B(y,\lambda_k/m)} = \left(\frac{1}{32}\right)^2 \sum_{i=0}^{31} \sigma^2_{U'(y,z_j)} \tag{3.16}$$

The variance associated with the Fourier coefficients can then be used to calculate the variance associated with the disturbance profile at a particular spanwise wavelength ($\sigma^2_{U'_{rms}(y,\lambda_k/m)}$, shown in Eq. 3.17) using Eq. 3.9.

$$\sigma^2_{U'_{rms}(y,\lambda_k/m)} = \left(2 - \delta_{m(0)} - \delta_{m(16)}\right)\sigma^2_{B(y,\lambda_k/m)} \tag{3.17}$$

Finally, upper (Eq. 3.18) and lower (Eq. 3.19) bounds for the integrated energy are calculated by adding a positive or negative bias to the disturbance profile before integration.

$$E^{+}_{\lambda_k/m} = \frac{1}{\delta}\int_0^{\infty}(U'_{rms}(y,\lambda_k/m) + \sigma_{U'_{rms}(y,\lambda_k/m)})^2 dy \tag{3.18}$$

$$E^{-}_{\lambda_k/m} = \frac{1}{\delta}\int_0^{\infty} (U'_{rms}(y, \lambda_k/m) - \sigma_{U'_{rms}(y,\lambda_k/m)})^2 dy \tag{3.19}$$

This procedure for calculating uncertainty does not account for the uncertainty associated with δ, which is in the denominator of all of the integrated energies. The uncertainty in δ can be calculated by investigating the covariance matrix of the x_{VLE}/Re' fit shown in Eq. 3.1. This uncertainty is small but non-negligible, and should be accounted for when comparing the results to direct numerical simulations.

4. DISTRIBUTED ROUGHNESS

The first roughness configuration tested was the distributed roughness by itself. Two sets of three patches were built onto the roughness insert, and the insert was installed in the flat plate model. The distributed roughness started 878 mm downstream of the leading edge and ended 1006 mm downstream of the leading edge. The hotwire traverse was able to reach two of the three roughness patches for each set, so the hotwire measurements are phase-locked averaged in span over two roughness patches.

The initial test matrix included measurements of the wake created by the lower-amplitude roughness at multiple Reynolds numbers (Re_k values from ∼50 to ∼115, where Re_k is defined by Eq. 4.1); however, the velocity disturbance was too small to make meaningful measurements for the low amplitude, low speed cases. Table 4.1 shows the final test conditions that were selected.

$$Re_k = \frac{U_{y=k}k}{\nu} \tag{4.1}$$

Conditions 3 & 4 feature the same freestream speed with different roughness heights, while conditions 1 & 4 feature similar Re_k values using different freestream speeds. The uncertainty associated with Re_k incorporates the uncertainty due to the unit Reynolds number/virtual leading edge fit and the uncertainty in the manufactured roughness height.

4.1 Contour Plots

For each of the four conditions, twenty hotwire scans were performed to measure the roughness wake. Nine of these scans occurred over the distributed roughness,

Table 4.1: Test conditions for distributed roughness only test configuration

Condition	Unit Reynolds Number, 1/mm	Max Roughness Height, mm	Re_k
1	548.9	0.85	113 ± 15
2	772.4	0.85	182 ± 21
3	868.5	0.85	230 ± 27
4	868.5	0.60	115 ± 19

while eleven more scans characterized the mid- and far-wakes. On the simplest level, the hotwire results can be summarized by noting that the distributed roughness creates very small disturbances.

Figure 4.1 shows velocity contours colored by $100u'_{rms}$ for all four test conditions at x = 1000 mm, which is above the downstream end of the distributed roughness. The envelope of the distributed roughness patch is drawn in white for reference. Two small ripples are seen in each velocity contour, near z = -5 mm and z = 3 mm. The disturbances are easier to see in the third contour plot, which is from the highest Re_k condition. All four contours have a very low level of unsteadiness; only condition 3 shows an increased level of unsteadiness associated with the roughness wake. Overall, the contours show that the disturbances created by the distributed roughness are small.

Figure 4.2 shows velocity contours for all four test conditions at x = 1400 mm, which is in the far-wake. All four contours show small amplitude high-speed streaks near z = -4 mm and z = 0 mm that increase in strength with Reynolds number. None of the contours show a significant increase in u'_{rms} associated with the low- and high-speed streaks in the roughness wake. The distributed roughness is only tickling the bottom part of the boundary layer, and the disturbances are extremely small.

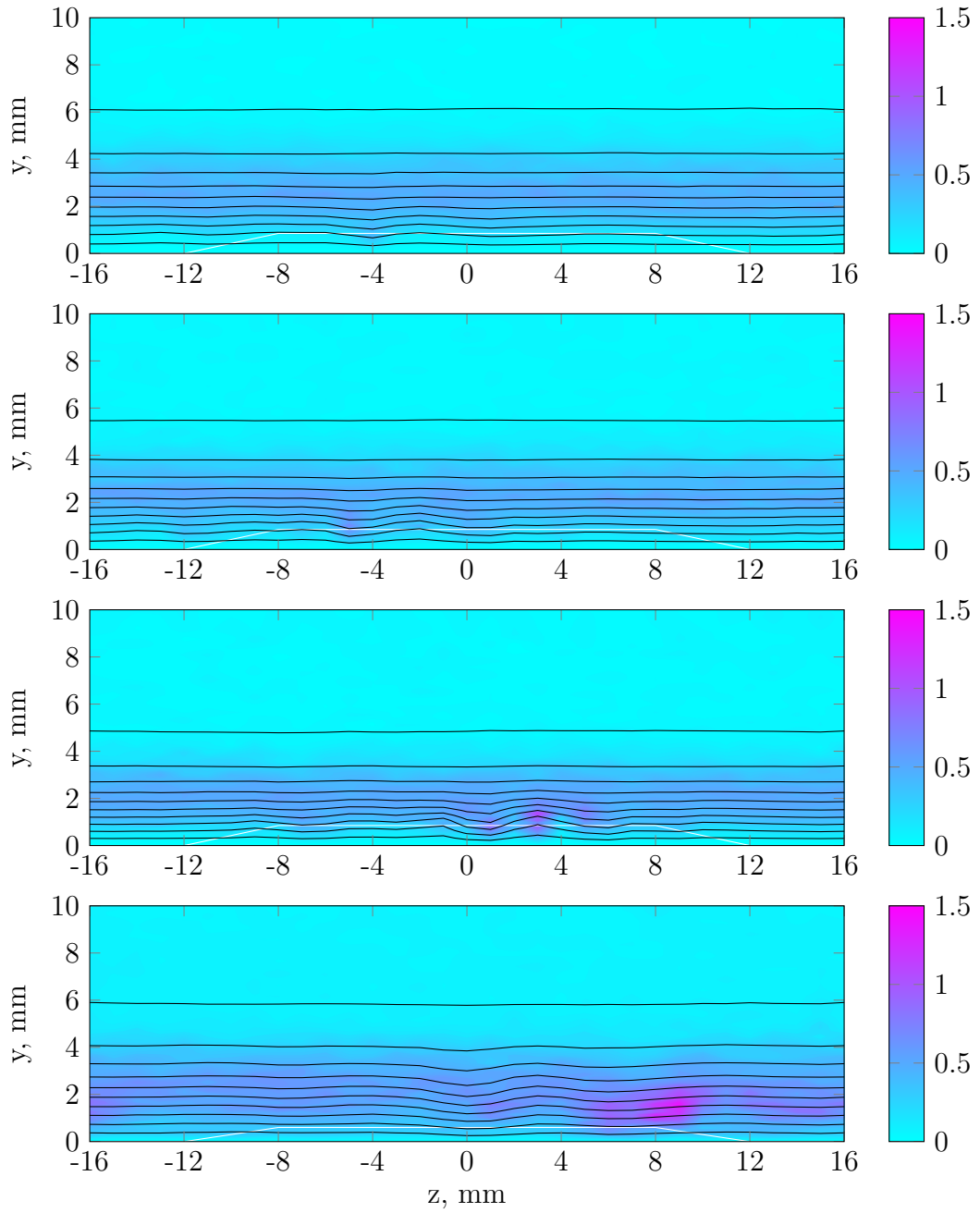

Figure 4.1: Contour plots of steady streamwise velocity (10% increments) colored by $100u'_{rms}$ at x = 1000 mm for conditions 1 (top) through 4 (bottom)

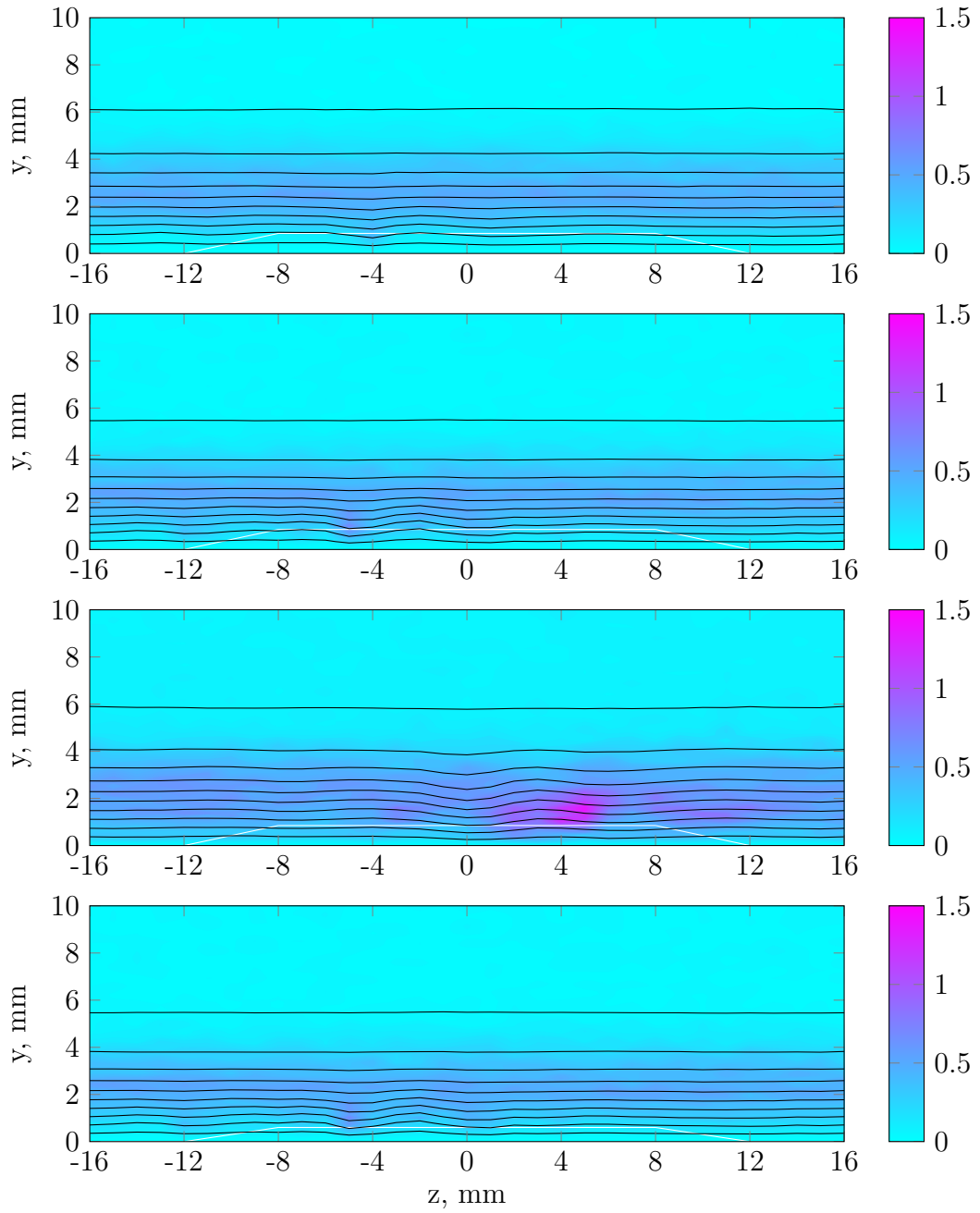

Figure 4.2: Contour plots of steady streamwise velocity (10% increments) colored by $100u'_{rms}$ at x = 1400 mm for conditions 1 (top) through 4 (bottom)

4.2 Disturbance Profiles

The steady disturbance profiles describe the magnitude of the roughness' effect on the flow. Figure 4.3 shows the disturbance profiles for all four conditions at x = 1000 mm. The peak disturbance occurs near the maximum roughness height for each configuration (0.85 mm for configurations 1-3 and 0.60 mm for condition 4.) As expected, the area under the curves for conditions 1 and 4 is similar because they have similar values of Re_k. As Re_k is increased (condition 1 to condition 2 to condition 3), the peak rms disturbance increases to almost 4% of the freestream speed.

Figure 4.4 shows the disturbance profiles for the same configuration in the far-wake, at x = 1400 mm. These profiles show the lift-up effect described by Landahl [5]; the profiles have broadened in the wall-normal direction, and the location of the maximum disturbance has moved away from the wall. The maximum amplitude of the disturbance profiles also decreased compared to the profiles at x = 1000 mm.

One of the main concepts of transient growth is the redistribution of streamwise momentum in the boundary layer. Streamwise vorticity pulls high-momentum fluid from the top of the boundary layer to the bottom of the boundary layer, while low-momentum fluid near the wall is pulled towards the edge of the boundary layer. The redistribution of momentum can be quantified by decomposing the roughness wake into different spanwise modes and analyzing the m = 0, or spanwise invariant, disturbance mode. This mode describes the change in the mean velocity in the roughness wake relative to undisturbed boundary layer.

According to Eq. 3.9, the m = 0 mode disturbance ($U'_{rms}(y, \lambda_k/0)$) is always positive. In reality, the m = 0 mode can be created by either a low-speed disturbance or a high-speed disturbance. To distinguish between the two types of disturbances,

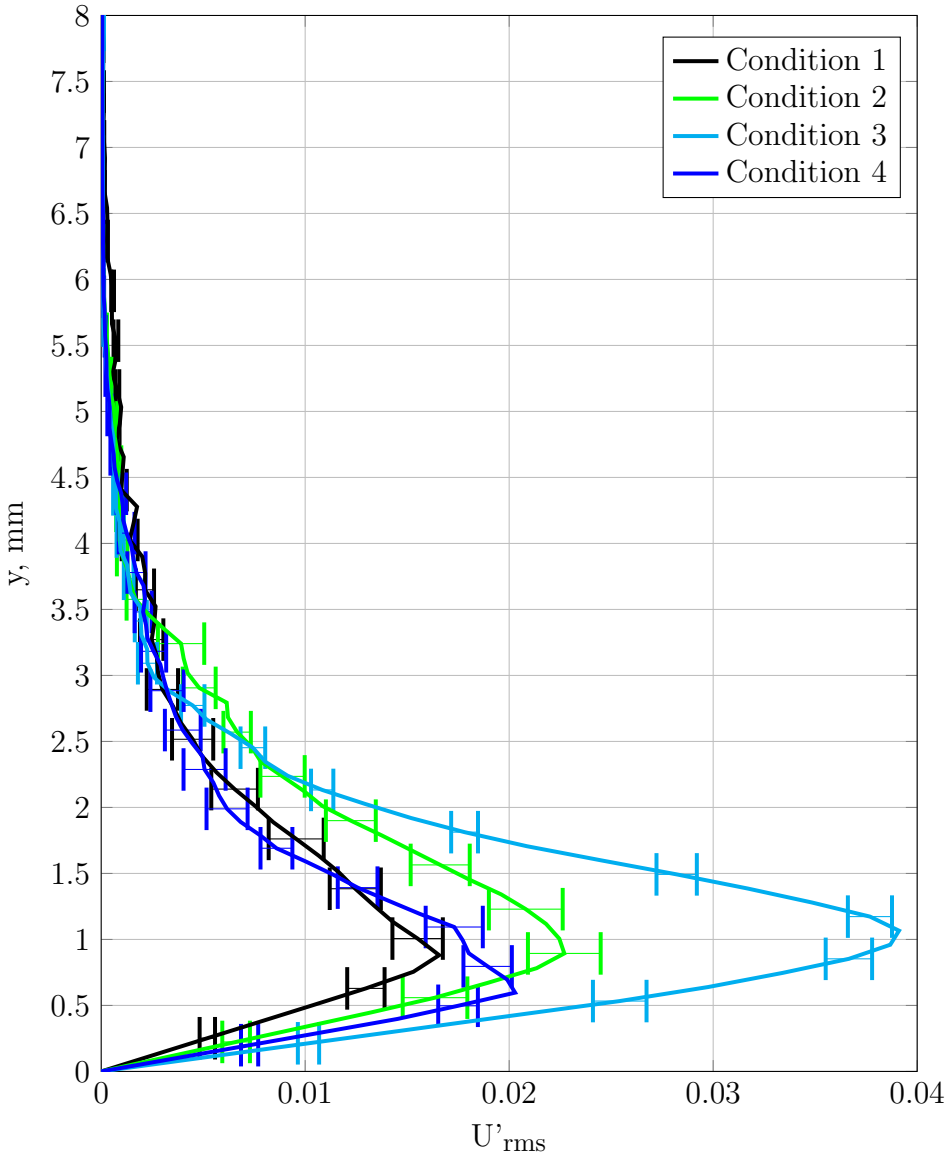

Figure 4.3: Total steady disturbance profiles at x = 1000 mm for all four distributed roughness configurations

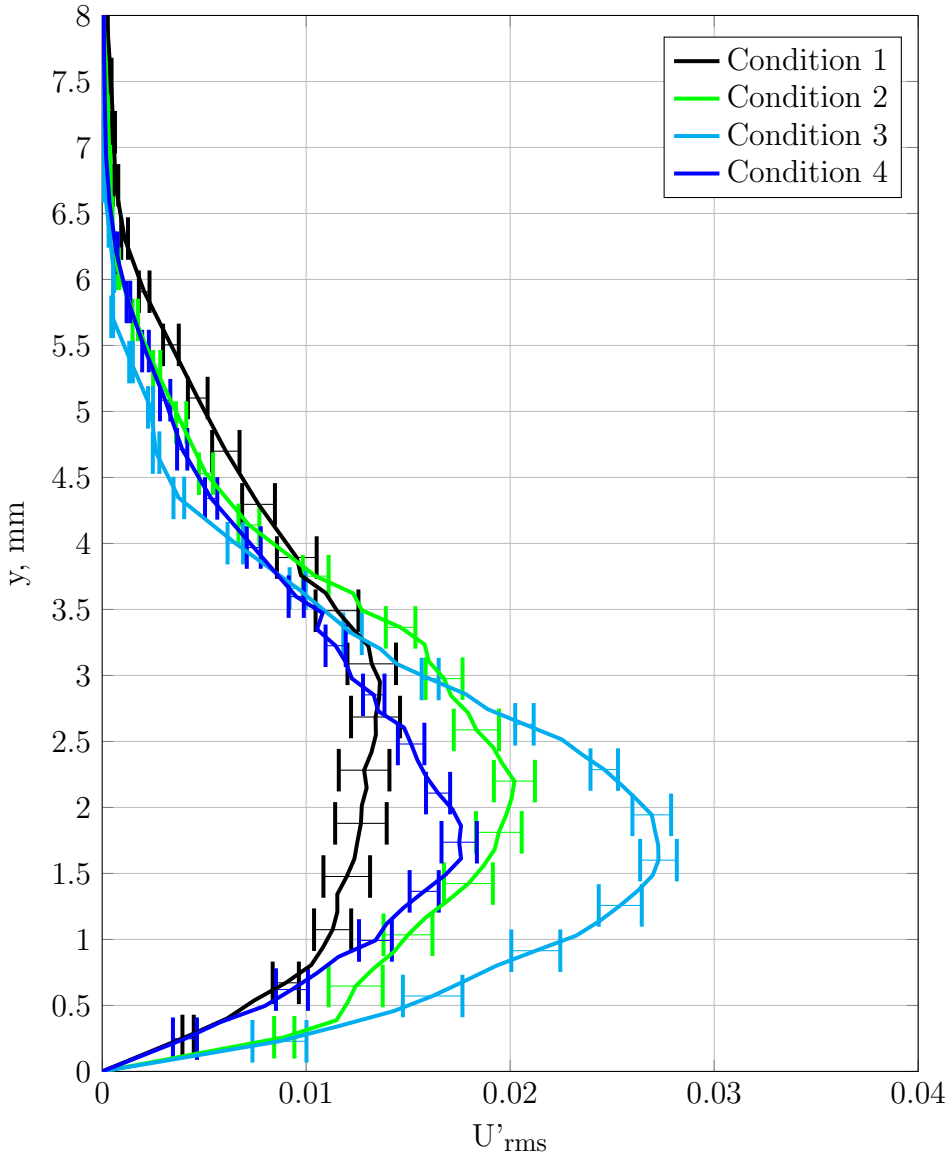

Figure 4.4: Total steady disturbance profiles at x = 1400 mm for all four distributed roughness configurations

U'_{mean} is defined by setting m to 0 in the Fourier transform shown in Eq. 3.8, which is equivalent to taking the spanwise mean of $U'(y, z)$.

$$U'_{mean}(y) = \frac{1}{32} \sum_{i=0}^{31} U'(y, z_i) \tag{4.2}$$

Because of the definition of the Fourier transform and the normalization of the energy associated with the m = 0 mode, $U'_{rms}(y, \lambda_k/0)$ is just the absolute value of U'_{mean}.

$$U'_{rms}(y, \lambda_k/0) = \sqrt{\left(U'_{mean}(y)\right)^2} \tag{4.3}$$

A positive U'_{mean} disturbance indicates that the roughness wake has a higher mean velocity than the undisturbed boundary layer, while a negative U'_{mean} disturbance indicates that the presence of the roughness has slowed down the flow relative to the undisturbed boundary layer. A negative U'_{mean} disturbance could also indicate that the boundary layer has been displaced away from the wall, similar to what was observed by Reshotko & Leventhall [24].

Figure 4.5 shows U'_{mean} profiles at different streamwise locations for the second roughness condition ($Re_k = 183$). The jaggedness in the profiles can be attributed to the small disturbance being measured and the small number of spanwise averages. At x = 900 mm and x = 950 mm, which are above the distributed roughness, the U'_{mean} disturbance is negative near the wall, which indicates that the distributed roughness is slowing down the fluid at the bottom of the boundary layer. Towards the end of the distributed roughness (x = 1000 mm), streamwise vorticity has begun pulling high momentum fluid towards the wall to create a positive U'_{mean} disturbance above y = 1 mm. Further downstream, at x = 1200 mm and x = 1400 mm, there is no distributed

roughness to slow down the fluid near the wall, and the size of the velocity excess in the roughness wake has increased. The three other roughness configurations are not shown, but all three show the same trends in the U'_{mean} profiles.

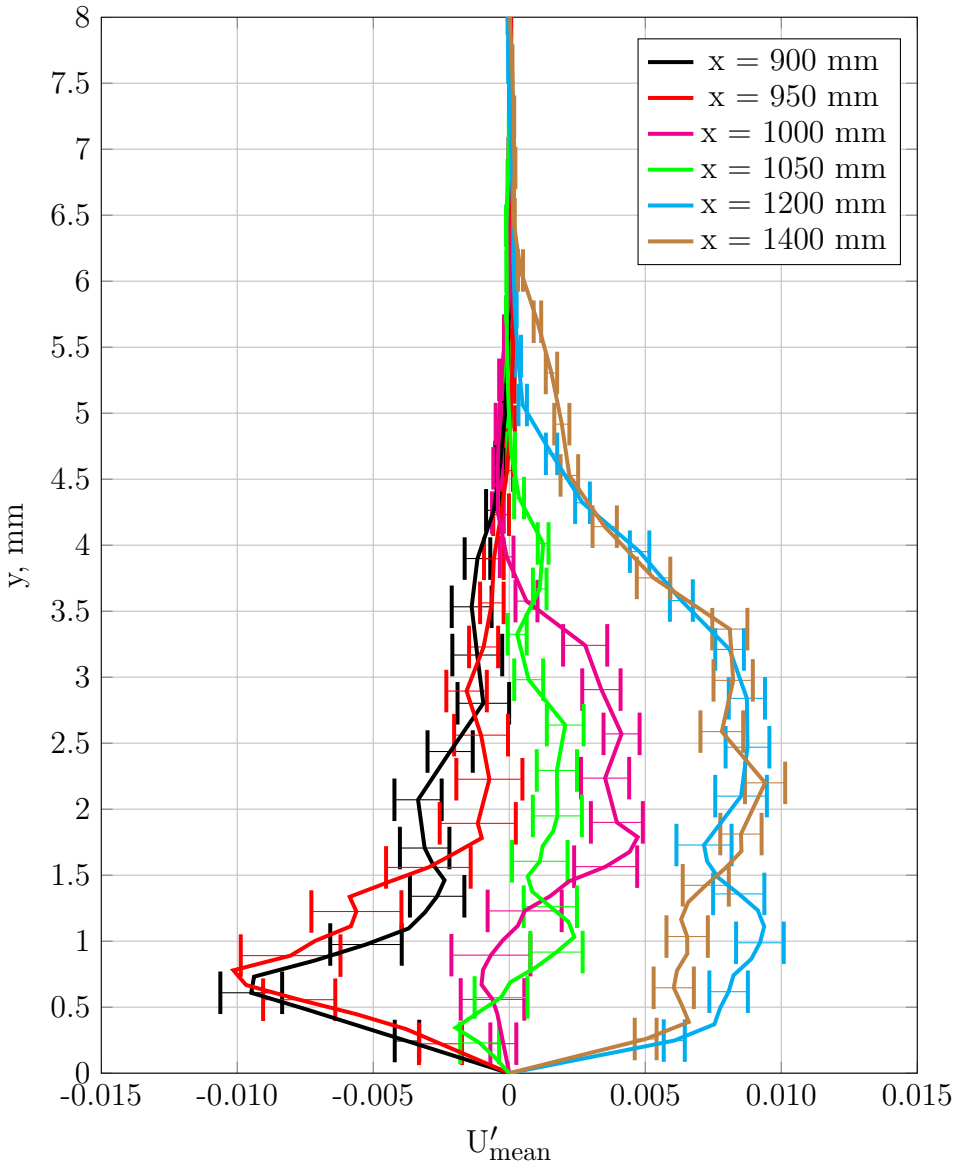

Figure 4.5: U'_{mean} profiles at multiple streamwise locations for the distributed roughness configuration at the second test condition ($Re_k = 182$)

.

4.3 Disturbance Energy

Figure 4.6 shows the streamwise evolution of the disturbance energy for the second Reynolds number condition. The abscissa is the streamwise distance downstream of x_r (= 918 mm, the location where the discrete roughness element would be) normalized by the boundary layer length scale (from Eq. 3.1) at $x = x_r$. The distributed roughness excites disturbances over a wide range of spanwise wavelengths; the first nine modes (m = 0 through m = 8) are shown in this figure. The total energy grows over the distributed roughness and slightly increases directly downstream of the roughness before slowly decaying in the far-wake. Over the distributed roughness, all of the modes grow at a fast rate. Downstream of the roughness, some of the modes continue to grow while other modes begin to decay. The shorter spanwise wavelength modes (m = 7 and m = 8) immediately begin to decay. The m = 4 though m = 6 modes all grow over a short distance before decaying, and the m = 0, m = 1, and m = 2 modes either grow slowly or remain almost constant in the far-wake. Longer spanwise wavelength modes reach their maximum energy farther downstream than shorter wavelength modes. The results for the other roughness conditions are similar; the relative amplitude of the different spanwise modes changes, but all of the qualitative trends seen for this condition also apply to the other conditions.

Optimal growth theory dictates that the m = 2 or m = 3 mode should experience the most growth; however, both the m = 2 and m = 3 modes experience relatively small growth compared to the other wavelengths. This further highlights the need to better understand receptivity. Receptivity sets both the initial amplitudes and the growth rates for the different spanwise disturbances, so the distributed roughness must not provide a receptive environment for transient growth of the m = 3 mode. This is an interesting result due to relative strength of $\lambda_z/3$ roughness modes

contained in the distributed roughness patch (see Table 3.4.)

For modeling purposes, we would like to understand how roughness-induced disturbances scale with roughness height and freestream speed. White et al. [14] showed that the disturbance energy created by an array of cylindrical roughness elements scaled with $\mathrm{Re}_{\mathrm{k}}^2$, and Downs et al. [28] concluded that the disturbance energy created by patches of distributed roughness also scales with $\mathrm{Re}_{\mathrm{k}}^2$. In contrast, Reshotko & Tumin [36] developed a transient-growth-based transition model for hypersonic flows that scales the input disturbance energy according to the roughness height, and they were able to apply this model successfully for hypersonic zero-pressure gradient and stagnation point flows.

Figure 4.7 shows the total disturbance energy scaled by $\mathrm{Re}_{\mathrm{k}}^2$ for all four conditions, which incorporate different roughness heights and freestream speeds. The $\mathrm{Re}_{\mathrm{k}}^2$ scaling works well in the near- and mid-wake, but the points in the far-wake are highly scattered. Adding additional points to this plot that feature a larger disturbance (increasing Re_{k} beyond 230) and include more spanwise averages (possibly four averages instead of two) would further elaborate on this scaling issue.

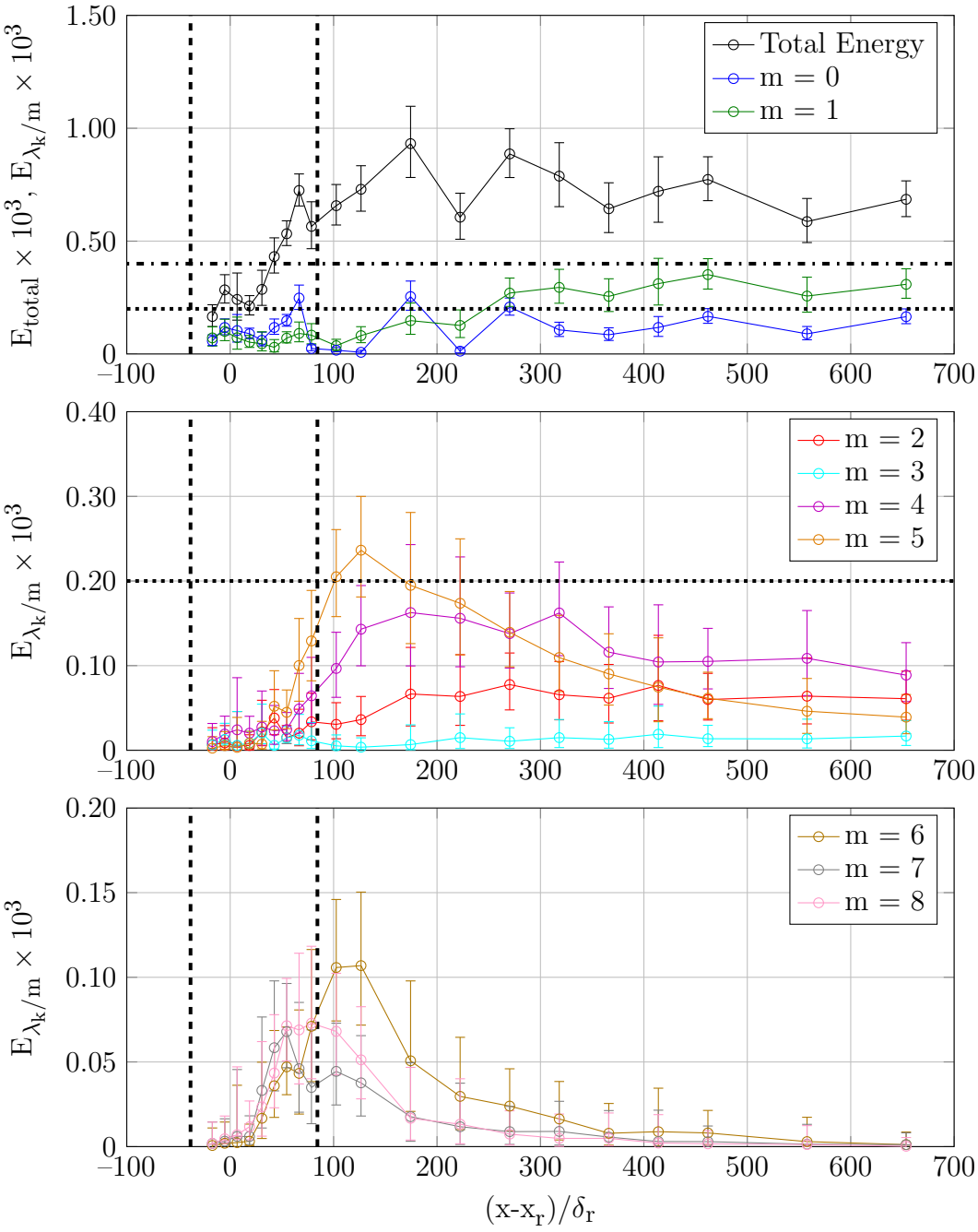

Figure 4.6: Streamwise energy evolution of steady disturbance energy for the second distributed roughness condition ($Re_k = 182$). The vertical dashed lines indicate the location of the distributed roughness, while the horizontal lines indicate the scaling of the second (dot-dash) and third (dotted) figures.

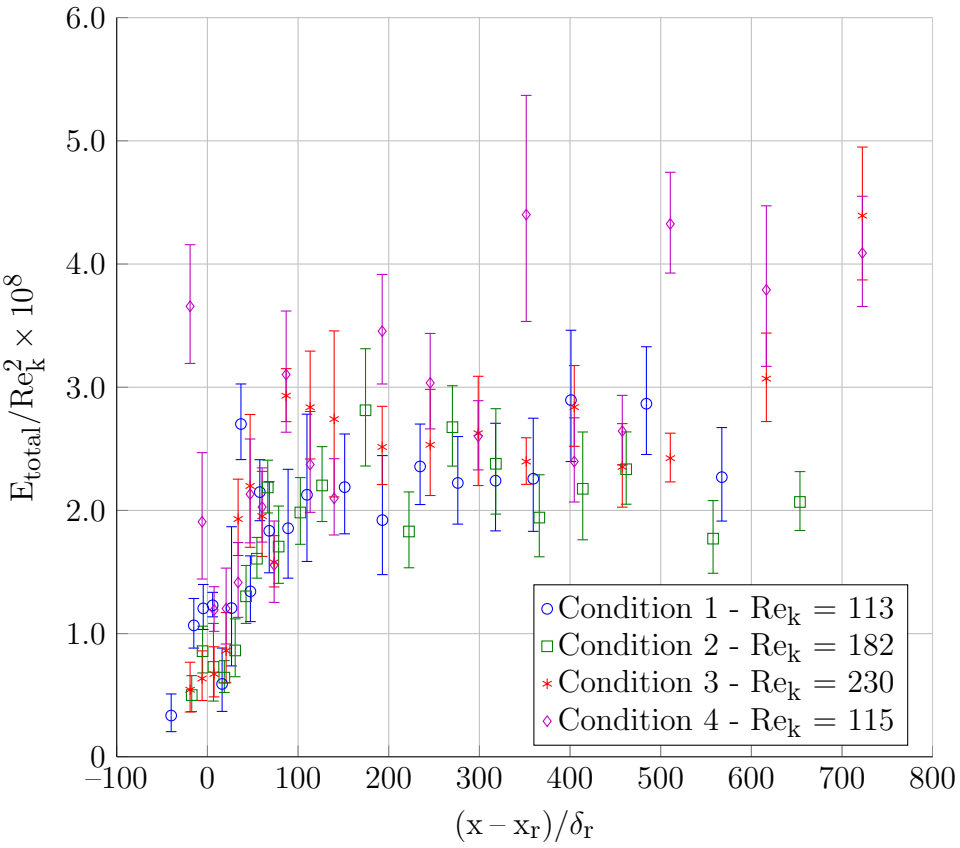

Figure 4.7: Total energy scaling for all four distributed roughness test conditions

5. DISCRETE ROUGHNESS

The second roughness tested was the discrete roughness only configuration, which consisted of 10 mm × 5 mm slanted rectangles placed 918 mm downstream of the plate leading edge.

Naphthalene flow visualization and hotwire measurements were used to analyze the wake of this roughness at two different Reynolds numbers. The lower Reynolds condition ($Re_k = 151$) produced a laminar wake, while the higher Reynolds number condition ($Re_k = 220$) produced a wake that forms a turbulent wedge ∼15 boundary layer thicknesses downstream of the roughness. Table 5.1 shows the details of the two test conditions.

5.1 $Re_k = 151$ Condition

For the $Re_k = 151$ condition, the tunnel was set to the same unit Reynolds number as the lowest Reynolds number condition for the distributed roughness configuration (Condition 1 as shown in Table 4.1.) At this Reynolds number, the slanted rectangles produce a laminar roughness wake.

Table 5.1: Test conditions for discrete roughness only test configuration

Condition	Unit Reynolds Number, 1/mm	Discrete Roughness Height, mm	Re_k
Low Re'	544.3	1.00	151 ± 12
Medium Re'	690.5	1.00	220 ± 22

5.1.1 Naphthalene Flow Visualization

Naphthalene flow visualization was used to see the effect of the roughness on wall shear stress. Downs [37] provides a thorough explanation of this technique, which is briefly described here.

Naphthalene, the main component in moth balls, is dissolved in acetone to create a near saturated solution (approximately 1 part naphthalene to 4 parts acetone by weight.) The solution is then sprayed onto the flat plate model using a pressure sprayer set to 25–30 psi. If applied correctly, the acetone evaporates within seconds and leaves a thin coating of naphthalene on the model surface. The tunnel is then set to a constant Reynolds number condition, and the naphthalene begins to sublimate at a rate proportional to the wall shear stress. Regions of higher shear stress (turbulent regions or regions with high-speed streaks) sublimate within a few minutes, while regions with lower shear stress (laminar regions or regions with low-speed streaks) remain coated in naphthalene much longer. Once the flow is fully visualized, the tunnel is run at a fast speed to enhance the naphthalene sublimation rate.

The acetone solution used for this technique could potentially dissolve the rapid-prototyping material used to construct the roughness. To avoid this issue, parts of the roughness insert were covered in 64 μm thick orange Kapton tape. The tape was precisely laid down to prevent any steps/gaps in the application. The thickness of the tape is very small compared to the thickness of the boundary layer; the Re_k of the 2D step created by the tape is less than 1; thus, the tape is assumed to have no effect on the structure of the boundary layer.

Figure 5.1 shows a picture of the flow visualization for the $\mathrm{Re}_k = 151$ condition. The asymmetry of the roughness is clearly seen in the near wake; the leading edge of the roughness creates a high-speed region behind the lower portion of the slanted

rectangle. The interaction of the flow past the leading edge and the flow past the trailing edge then creates a low-speed region behind the trailing edge. The wake straightens into a single low-speed and single high-speed streak that move straight downstream. The width of the streaks spreads slightly far downstream, but they remain compact and do not interact with each other. The streaks persist hundreds of boundary layer thicknesses downstream and do not directly lead to transition at this Reynolds number.

5.1.2 Contour Plots

Hotwire scans were performed at 19 streamwise locations to characterize the transient growth initiated by the slanted rectangles. Figure 5.2 shows contour plots of streamwise velocity as measured by the hotwire scans. The contour levels are 10% of the freestream speed, and the coloring shows the unsteady disturbance amplitude ($100u'_{rms}$). In the near wake region (at x = 935 mm), the contours show that the wake is mostly constrained within the outline of the discrete roughness element, which is shown with the white lines. As the wake extends downstream, a clear pair of low- and high-speed streaks form behind the roughness element, and the streaks affect the contours higher in the boundary layer. At x = 1700 mm, the effect of the streaks can be seen far away from the wall, at the edge of the boundary layer.

In addition to the lift-up effect, the spanwise wavelengths in the wake change as the wake evolves in the streamwise direction. The contour plots from far downstream show a large amplitude, long wavelength disturbance, but the contour plots from the near-wake show a compact disturbance comprised of several wavelengths. These hotwire contour plots agree with the naphthalene flow visualization shown in Fig. 5.1; the wake consists of a high-speed and low-speed pair of streaks that gradually broaden in the spanwise direction farther downstream.

Figure 5.1: Naphthalene flow visualization of discrete roughness geometry ($Re_k = 151$)

Over the extent of the domain, the unsteadiness remains almost constant. Increased unsteadiness is observed at regions with higher levels of wall-normal and spanwise shear stress, but the boundary layer remains laminar. Towards the end of the measurement domain, the unsteadiness in the wake increases slightly; however, hotwire scans further downstream show that the streaks do not lead to transition within the streamwise region that can be observed with the current experimental setup.

5.1.3 Disturbance Profiles

Figure 5.3 shows total disturbance profiles (U'_{rms}) at several different streamwise locations. These profiles confirm the presence of the lift-up effect; as the wake evolves in the streamwise direction, the peak of the disturbance profile shifts away from the wall while the disturbance profile broadens in the wall-normal direction.

An interesting aspect of these profiles is the peak disturbance amplitude. In the near-wake, the maximum spanwise rms disturbance is ~ 0.85. In the mid-wake region (at x = 950 mm), the maximum rms disturbance drops to ~ 0.68 before increasing to 0.75-0.80 in the far-wake. The change in the peak disturbance amplitude in the mid-wake can be explained by examining profiles of U'_{mean}, which are shown in Fig. 5.4. At x = 928 mm, the U'_{mean} profile is negative, which indicates a velocity deficit. This velocity deficit decreases quickly as the wake moves downstream; by x = 950 mm ($\sim$ four boundary layer thicknesses downstream), high momentum fluid has been pulled down from the top of the boundary into the bottom of the boundary layer. This momentum transfer causes a zero in the profile near y $\sim$ 0.5 mm, indicating that the high-speed streak penetrates farther down into the boundary layer than the low-speed streak. In the far wake, the entire U'_{mean} profiles becomes positive, which indicates a velocity excess due to the momentum transfer. These results are consistent with the

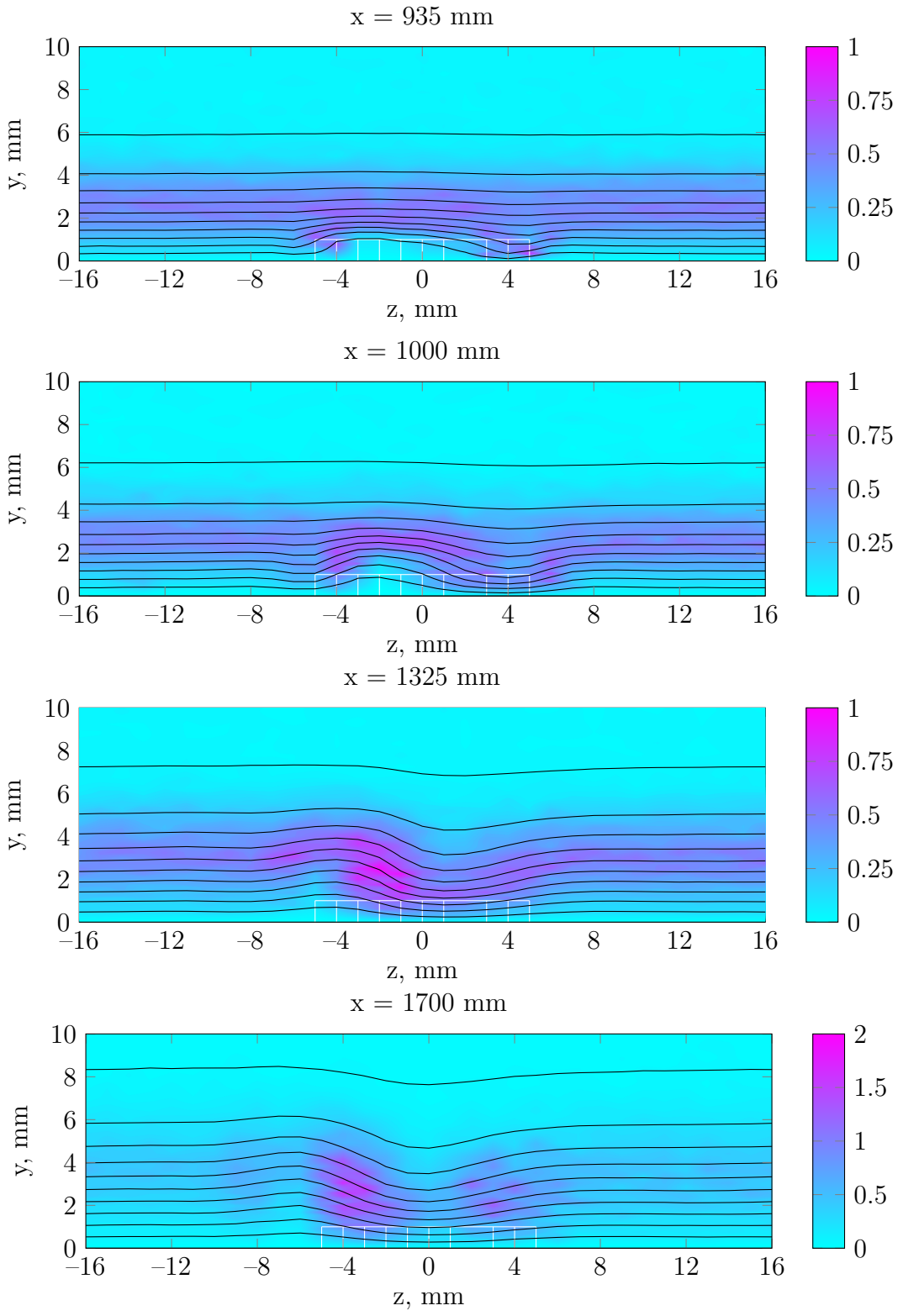

Figure 5.2: Contour plots of steady streamwise velocity (10% increments) colored by $100u'_{rms}$ at four streamwise locations for the discrete roughness only configuration at the $Re_k = 151$ condition.

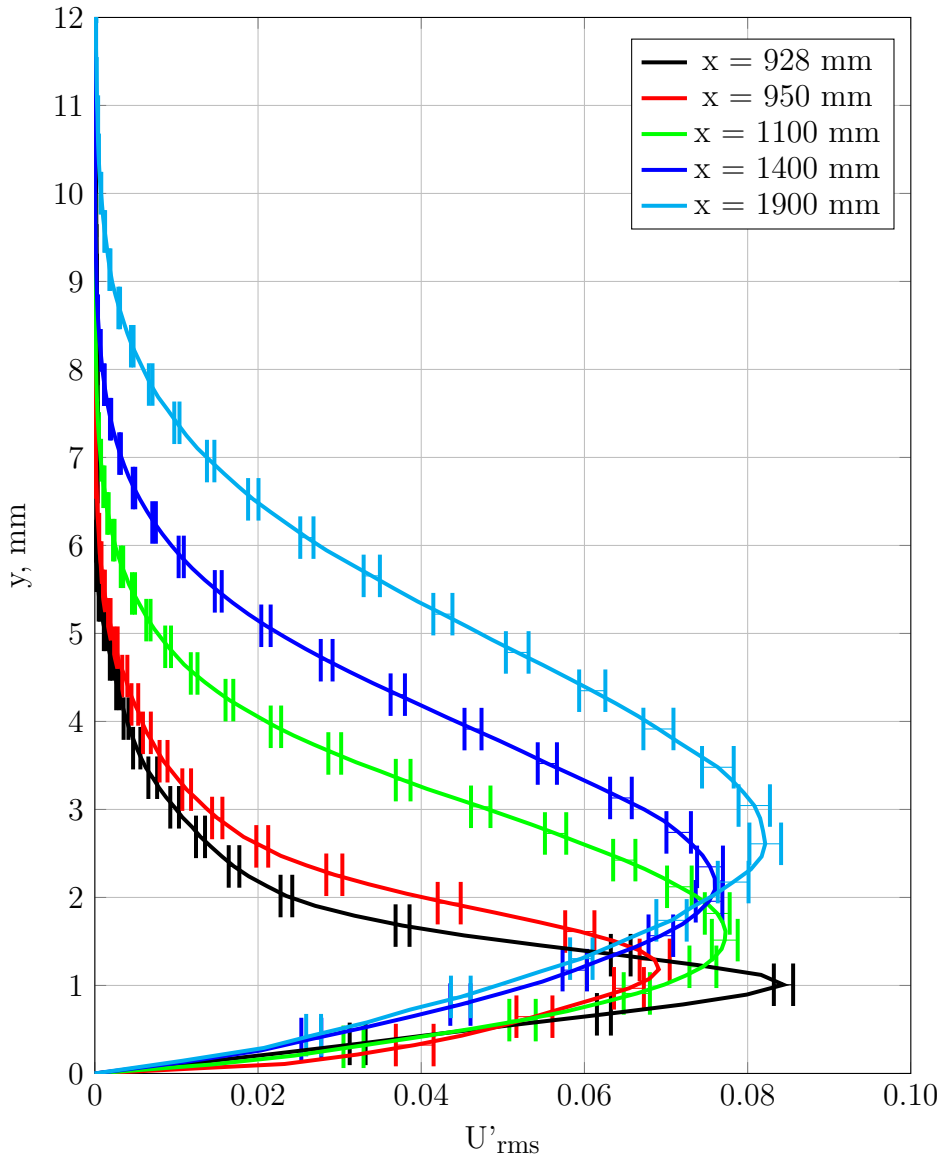

Figure 5.3: Total disturbance profiles at multiple streamwise locations for the discrete roughness only configuration at the $Re_k = 151$ condition.

observations of Kendall [25], who observed similar results with the velocity defect downstream of a small sand-grain roughness in a flat plate boundary layer.

Figures 5.5 and 5.6 show the disturbance profiles of the first six spanwise modes at x = 950 mm and x = 1400 mm, respectively. At x = 950 mm, several modes have strong amplitudes. Disturbances at longer spanwise wavelengths have larger amplitudes higher in the boundary layer ($\sim$ 1-1.5 mm away from the wall), while disturbances at shorter spanwise wavelengths reach their maximum amplitude lower in the boundary layer ($\sim$ 0.5-1 mm away from the wall). At x = 1400 mm, in the far wake, the disturbance profiles are much broader and all reach their maximum amplitude at the same height in the boundary layer. The longer wavelength disturbances have grown larger than the shorter wavelength disturbances, which are decaying by this streamwise location.

5.1.4 Steady Disturbance Energy

Figure 5.7 shows the integrated disturbance energy for the $Re_k = 151$ condition. The total disturbance energy grows in the near- and mid-wake before reaching a near constant value near 0.0105 in the far wake. At the end of the measurement domain, the disturbance energy begins to increase as the m = 0 and m = 1 disturbances continue to grow.

The energy at individual spanwise wavelengths reveals different types of transient growth patterns. The m = 0 and m = 1 modes decay before growing further downstream, while the m = 2, m = 3, and m = 4 modes grow in the near- and mid-wake before remaining constant (m = 2) or decaying (m = 3 and m = 4) further downstream.

The order with which the different disturbance wavelengths reach their maximum amplitude is consistent with transient growth theory. The shortest wavelength shown

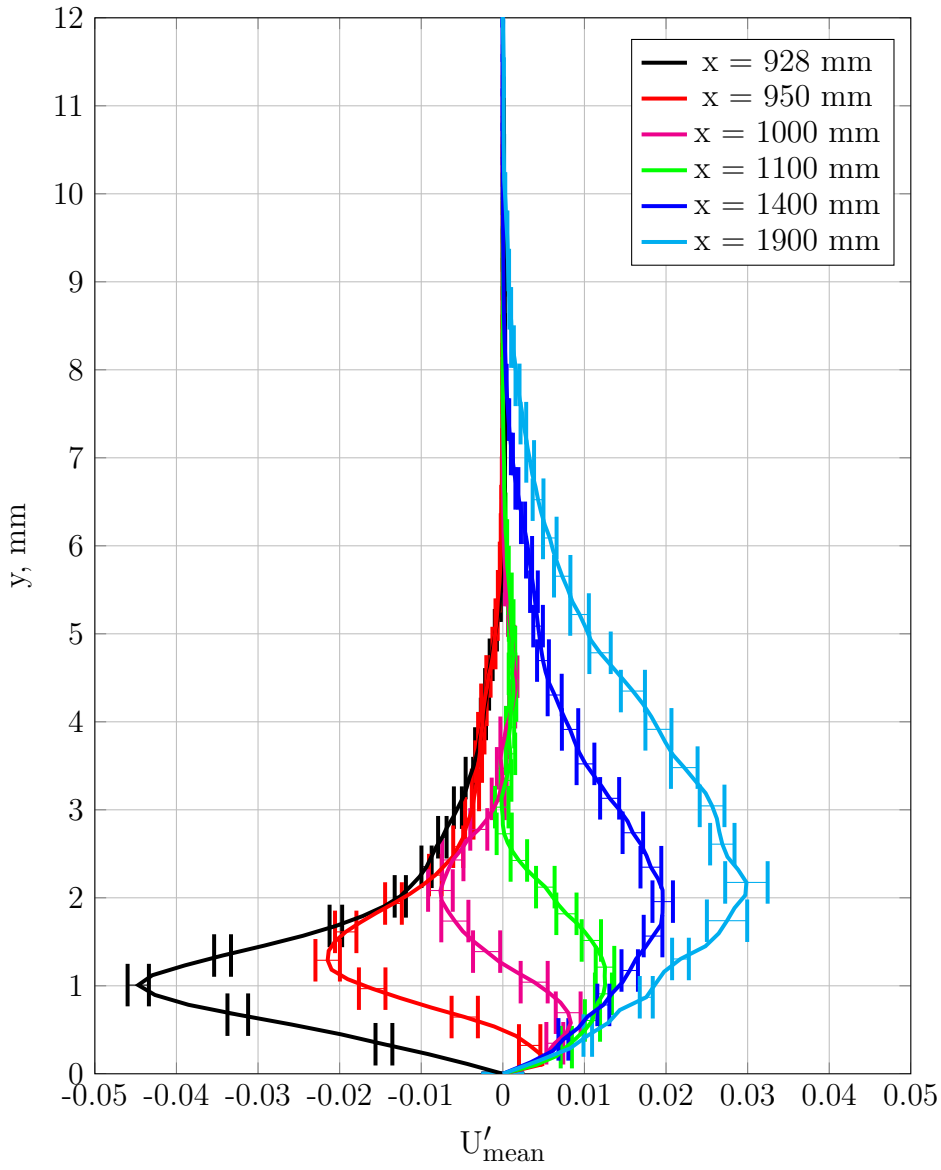

Figure 5.4: U'_{mean} profiles at multiple streamwise locations for the discrete roughness only configuration at the $Re_k = 151$ condition.

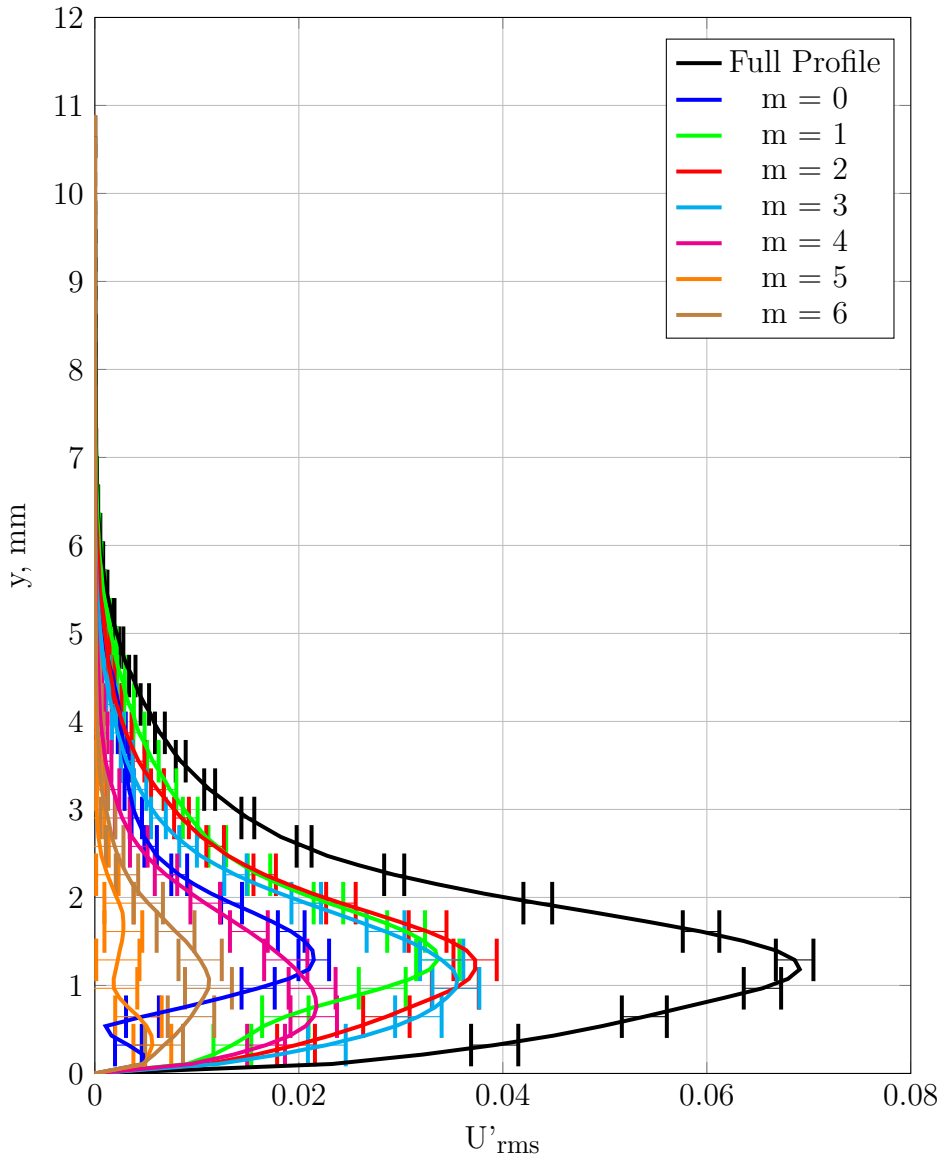

Figure 5.5: Disturbance profiles of different spanwise modes at x = 950 mm for the discrete roughness only configuration at the $Re_k = 151$ condition.

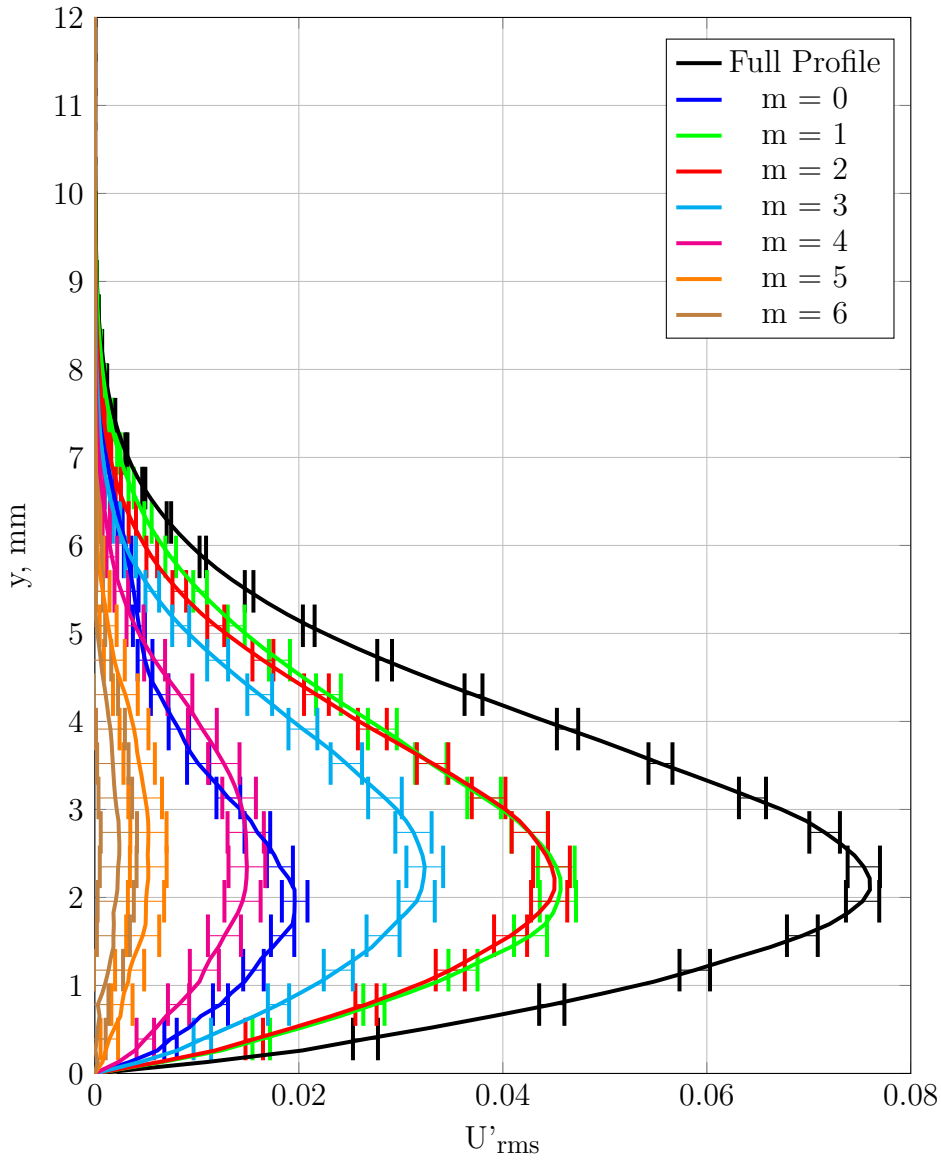

Figure 5.6: Disturbance profiles of different spanwise modes at x = 1400 mm for the discrete roughness only configuration at the $Re_k = 151$ condition.

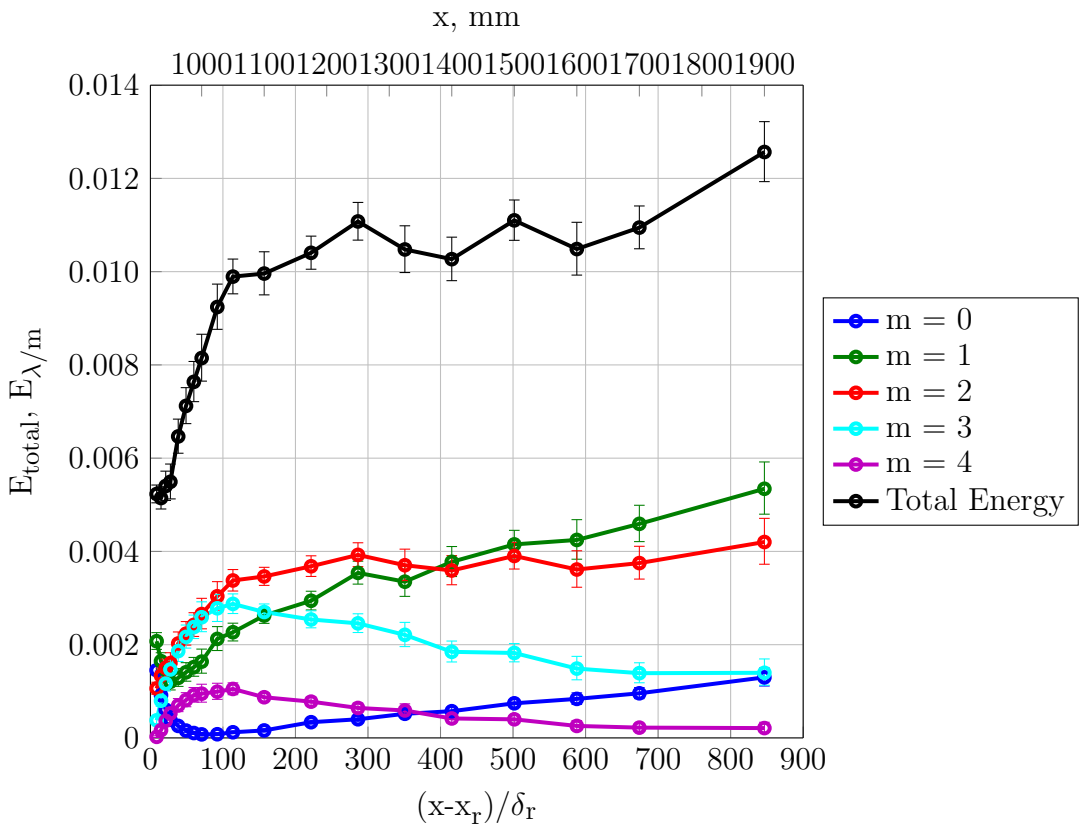

Figure 5.7: Streamwise evolution of disturbance energy for the discrete roughness only configuration at the $Re_k = 151$ condition. δ_r is the boundary layer length scale (as defined by Eq. 3.1) at the discrete roughness location.

(m = 4, or λ = 8 mm) is the first wavelength to reach maximum amplitude near $(x–x_r)/\delta_r = 100$. Each progressively longer spanwise wavelength reaches a maximum amplitude further downstream; in fact, the m = 1 mode is still growing at the end of the measurement domain. The m = 0 mode decays in the near-wake and grows in the far wake as high-speed fluid is pulled from the top of the bottom boundary layer towards the wall.

The m = 5, m = 6, and m = 7 modes also show measurable transient growth, but at much smaller amplitude than the disturbances at longer spanwise wavelengths. Figure 5.8 shows the integrated energy for these modes. Interestingly, even these

shorter spanwise wavelength show varying patterns of transient growth. The m = 5 mode shows a decay-grow-decay profile, while the m = 6 and m = 7 modes show a grow-decay profile. This further highlights the need to understand roughness receptivity at different spanwise wavelengths.

5.2 $Re_k = 220$ Condition

For the $Re_k = 220$ condition, the tunnel was set to the same unit Reynolds number as the middle Reynolds number condition for the distributed roughness configuration (Condition 2 as shown in Table 4.1). At this Reynolds number, the slanted rectangles produce a roughness wake that forms a turbulent wedge ∼15 boundary layers downstream.

5.2.1 Naphthalene Flow Visualization

Figure 5.9 shows naphthalene flow visualization for the discrete roughness configuration at the $Re_k = 220$ condition. The naphthalene shows a low-speed region in the wake of the slanted rectangles. Around x = 980 mm, the wake begins to show an alternating pattern of low and high speed streaks. Near x = 1050 mm, the roughness wake begins to spread like a turbulent wedge. The origin of the wedge can be traced back to x = 996 mm. The flow visualization shows a dogtooth pattern on the edges of the wedge which make defining a spreading angle difficult. By x = 1116 mm, the turbulent wedges have spread across the 32 mm periodicity, and the boundary layer is turbulent across the entire span. The structure of the near-wake and turbulent wedges is extremely consistent across the span

5.2.2 Contour Plots

Eleven hotwire scans were performed at multiple streamwise locations to characterize the flow above and downstream of the roughness. Figures 5.10 and 5.11 show

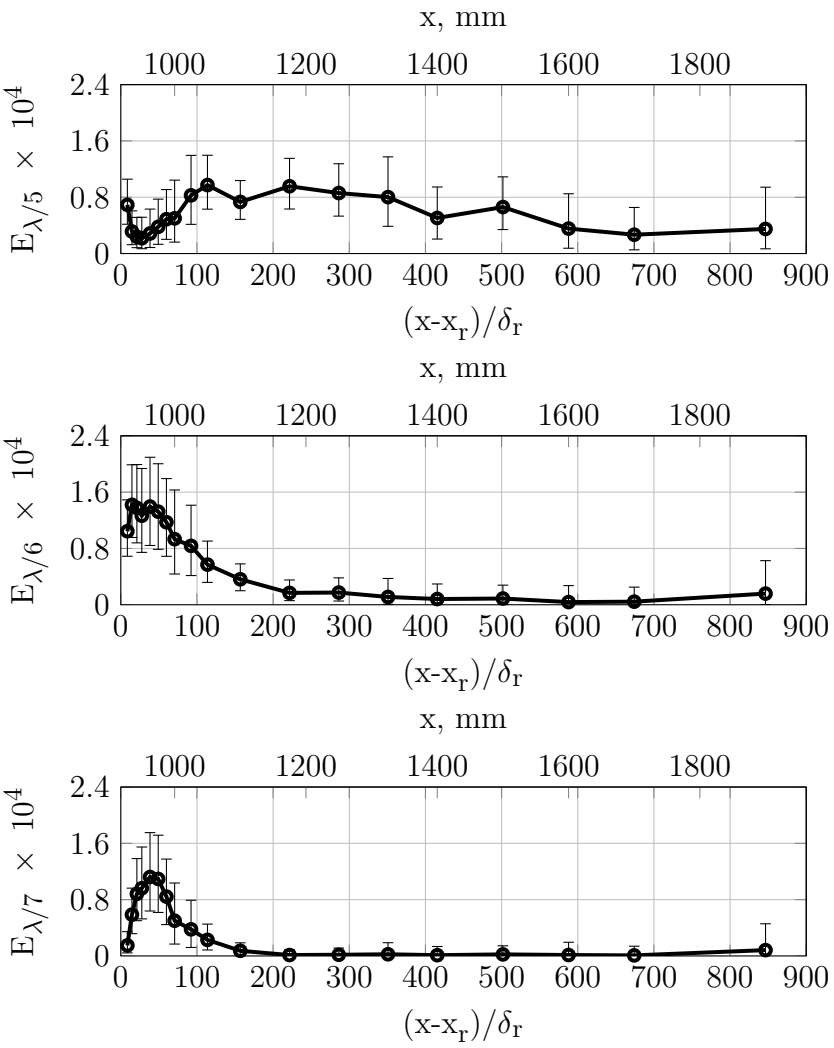

Figure 5.8: Streamwise evolution of disturbance energy for the m = 5 (top), m = 6 (middle), and m = 7 (bottom) spanwise wavelengths for the discrete roughness only configuration at the $Re_k = 151$ condition.

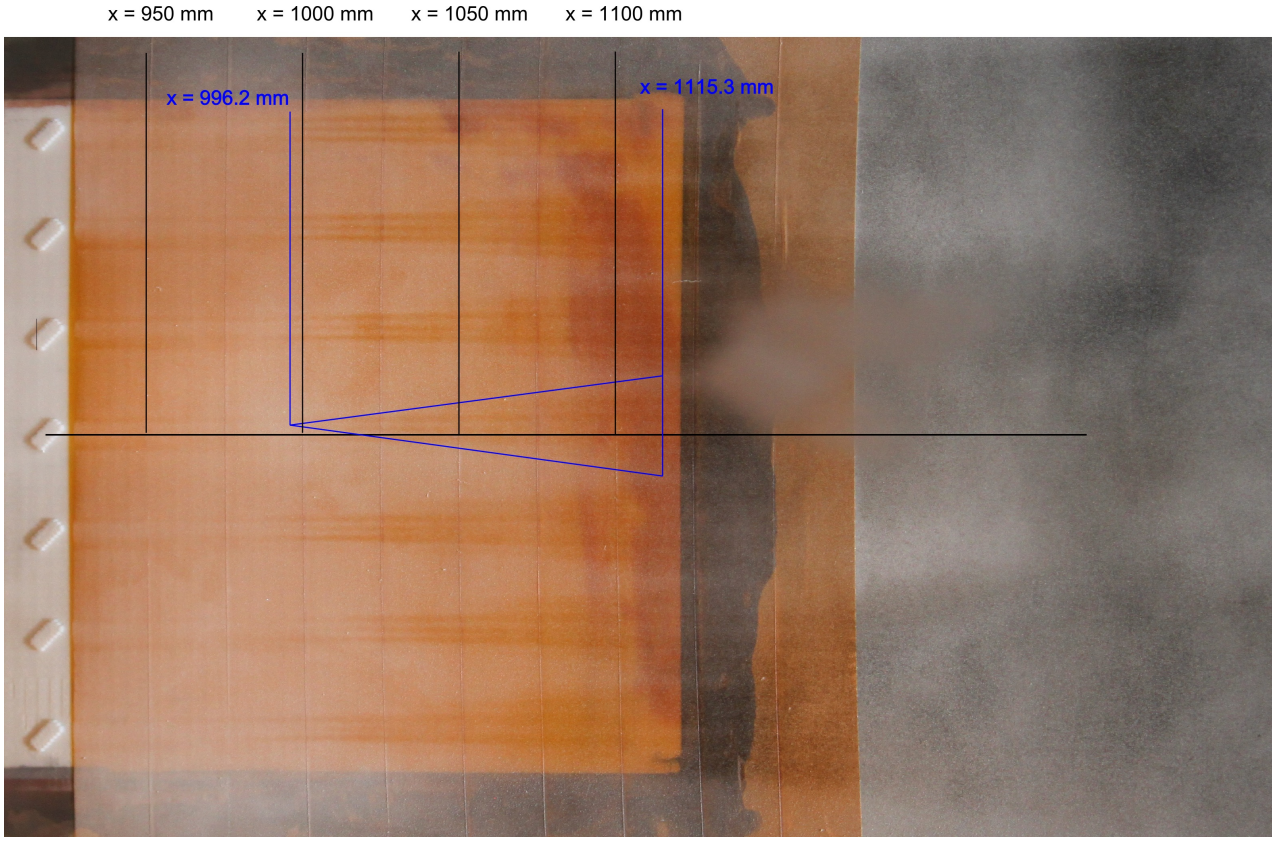

Figure 5.9: Naphthalene flow visualization of discrete roughness geometry ($\mathrm{Re_k} = 220$)

velocity contours at multiple streamwise locations. The structure of the mean flow in the near wake is very similar to the $Re_k = 151$ condition; however, the maximum unsteadiness grows from 1.6% to 2.5% between x = 928 mm and x = 950 mm. The increased unsteadiness is centered around the points in the flow with large amounts of spanwise and wall-normal shear, particurally along the low-speed streak. By x = 975 mm, the unsteadiness along the low speed streak has grown to 12% of the freestream speed.

The naphthalene visualization showed that the origin of the turbulent wedge is at x = 996 mm; the velocity contour measured at x = 1000 mm shows the beginning of the turbulent wedge. The low- and high-speed streaks that are seen in the flow visualization are also observed in the hotwire measurements at x = 1000 mm. The wedge continues to spread as it moves downstream; the contour plots at x = 1050 mm and 1100 mm show the growth of the wedge. Although a large portion of the boundary layer at x = 1100 mm is fully turbulent, the variation in the boundary layer height across the span is significant. The unsteadiness is largest at the edges of the turbulent wedge, and the interior structure of the wedge consists of relative low- and high-speed streaks that extend from the wall to the freestream.

5.2.3 Disturbance Profiles

Disturbance profiles further highlight the structure of the boundary layer before the turbulent wedge forms. Figure 5.12 shows total disturbance profiles at multiple streamwise locations before the boundary layer begins to transition. The structure of the profiles changes as you move from the near-wake to the mid-wake. First, the disturbance profile near the wall becomes more full; this is seen by comparing the profiles at x = 928 mm and x = 942.5 mm. The fullness of the profile near the wall eventually forms a second peak in the profile, which is seen in the profile at x =

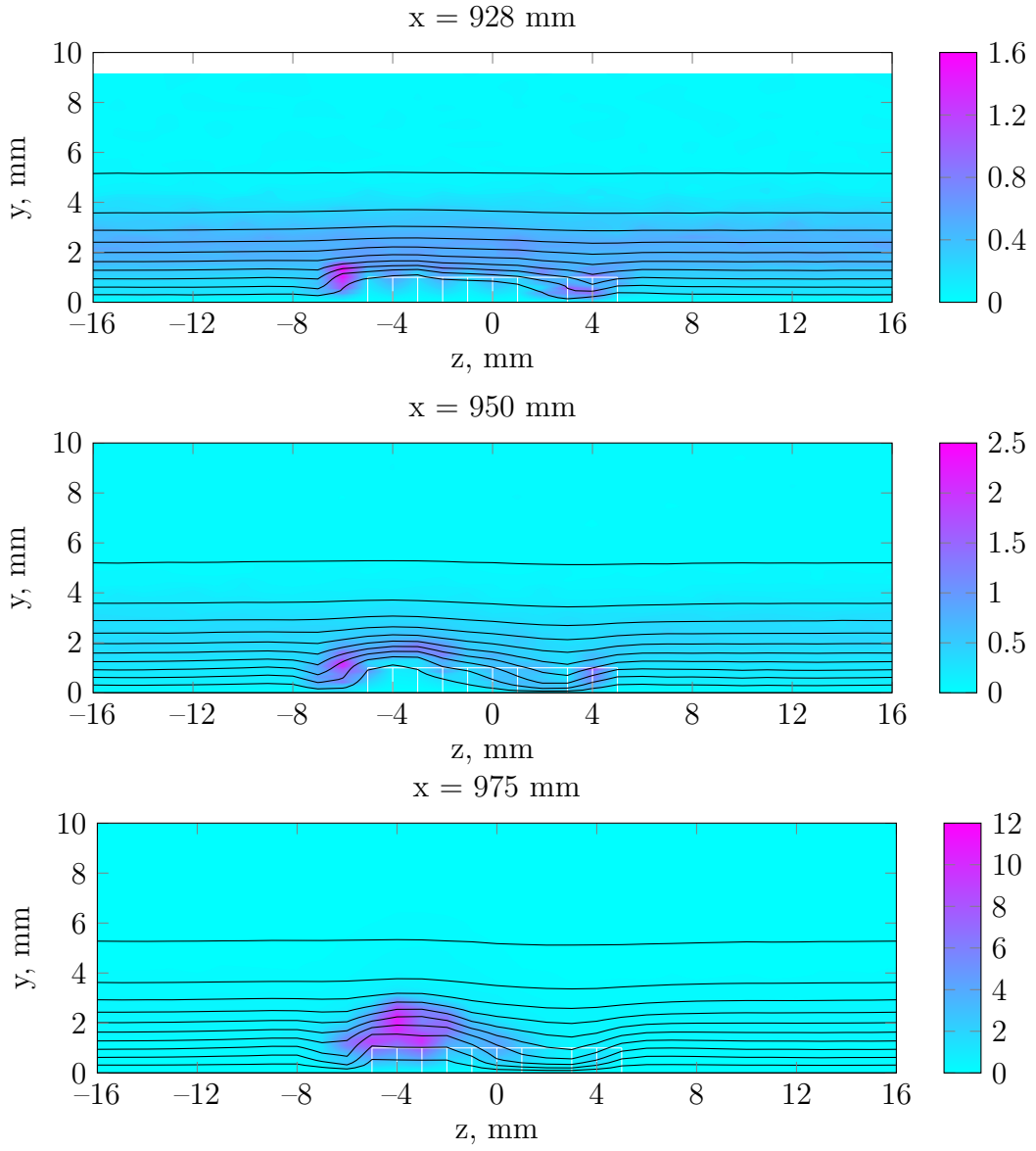

Figure 5.10: Contour plots of steady streamwise velocity (10% increments) colored by $100u'_{rms}$ at three streamwise locations for the discrete roughness configuration at the $Re_k = 220$ condition.

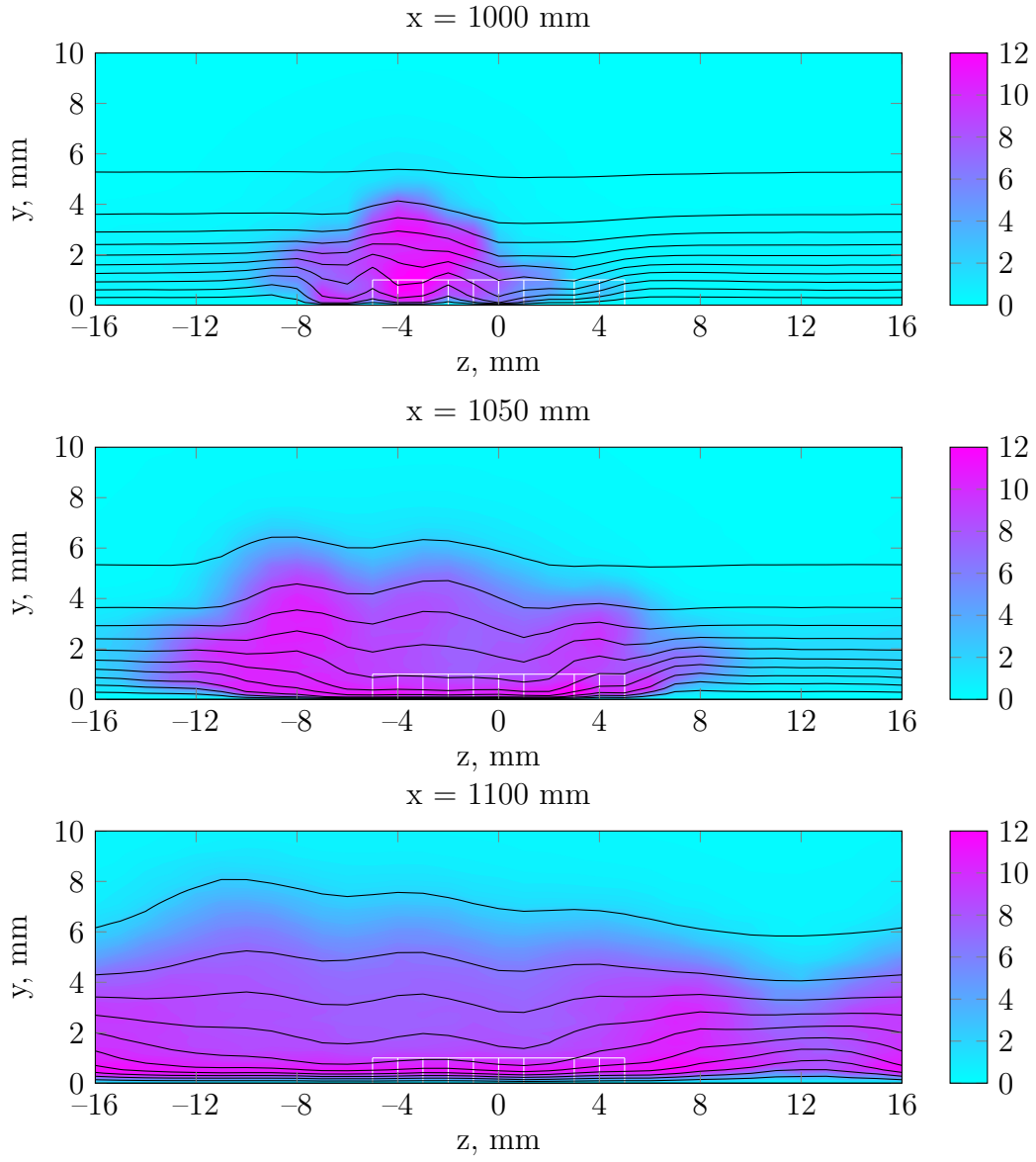

Figure 5.11: Contour plots of steady streamwise velocity (10% increments) colored by $100u'_{rms}$ at three additional streamwise locations for the discrete roughness configuration at the $Re_k = 220$ condition.

962.5 mm. At x = 975 mm, the two peaks in the disturbance profiles have almost combined into a single, broad peak. The double-peak structure in the profile may be an indication of non-linearity in the disturbance, which is not surprising considering that a turbulent wedge forms less than 25 mm downstream of these profiles.

Figure 5.13 shows disturbance profiles for the first six spanwise wavelengths at x = 928 mm. The total disturbance profile peaks at y = 1 mm, and the disturbances at the longest spanwise wavelengths also peak at y = 1 mm. The profiles for the shorter wavelengths disturbances do not have typical mode shapes; instead, their profiles are wavy and include multiple peaks.

Figure 5.14 shows disturbance profiles for the different spanwise wavelengths further downstream at x = 962.5 mm. At this streamwise location, several wavelengths have large amplitude disturbances over a large portion of the boundary layer (0.5 mm to 1.7 mm away from the wall. All of the wavelengths contribute to both the lower and higher peaks in the disturbance profile, and the lower peak in the profile sits just below the crossover point in the m = 0 profile.

Figure 5.15 shows the U'_{mean} disturbance profile at different streamwise locations. In the near wake, U'_{mean} is negative due to the velocity deficit downstream of the discrete roughness. As the wake evolves downstream, the high speed streak begins to penetrate to the bottom of the boundary layer, which leads to a crossover point in the profile. By x = 987.5 mm, the high-momentum fluid brought down into the boundary layer leads to a positive m = 0 profile. The turbulent wedge forms shortly downstream from the last profile shown.

5.2.4 Steady & Unsteady Disturbance Energy

Figure 5.16 shows the streamwise energy evolution of the different spanwise modes. The different spanwise wavelengths show different transient growth pat-

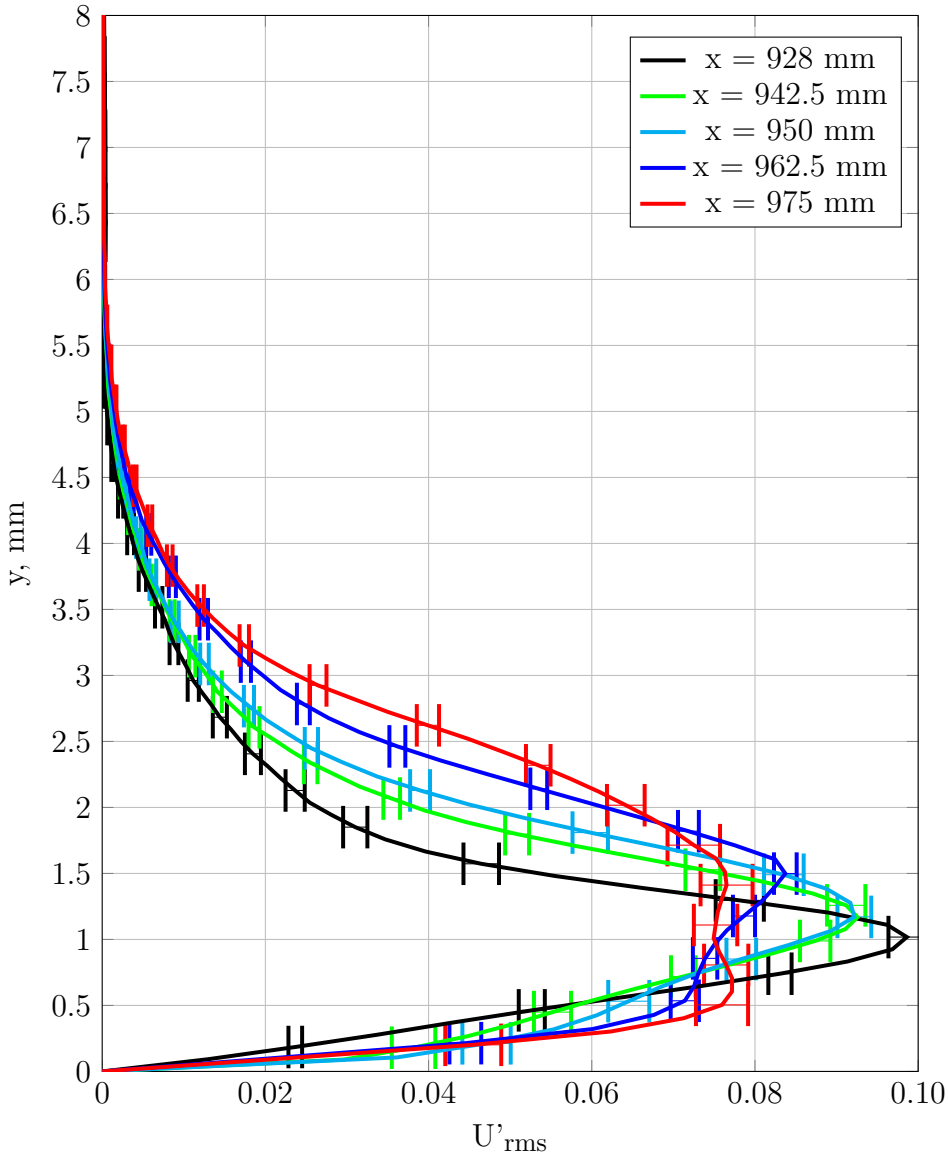

Figure 5.12: Total disturbance profiles at multiple streamwise locations for the discrete roughness only configuration at the $Re_k = 220$ condition.

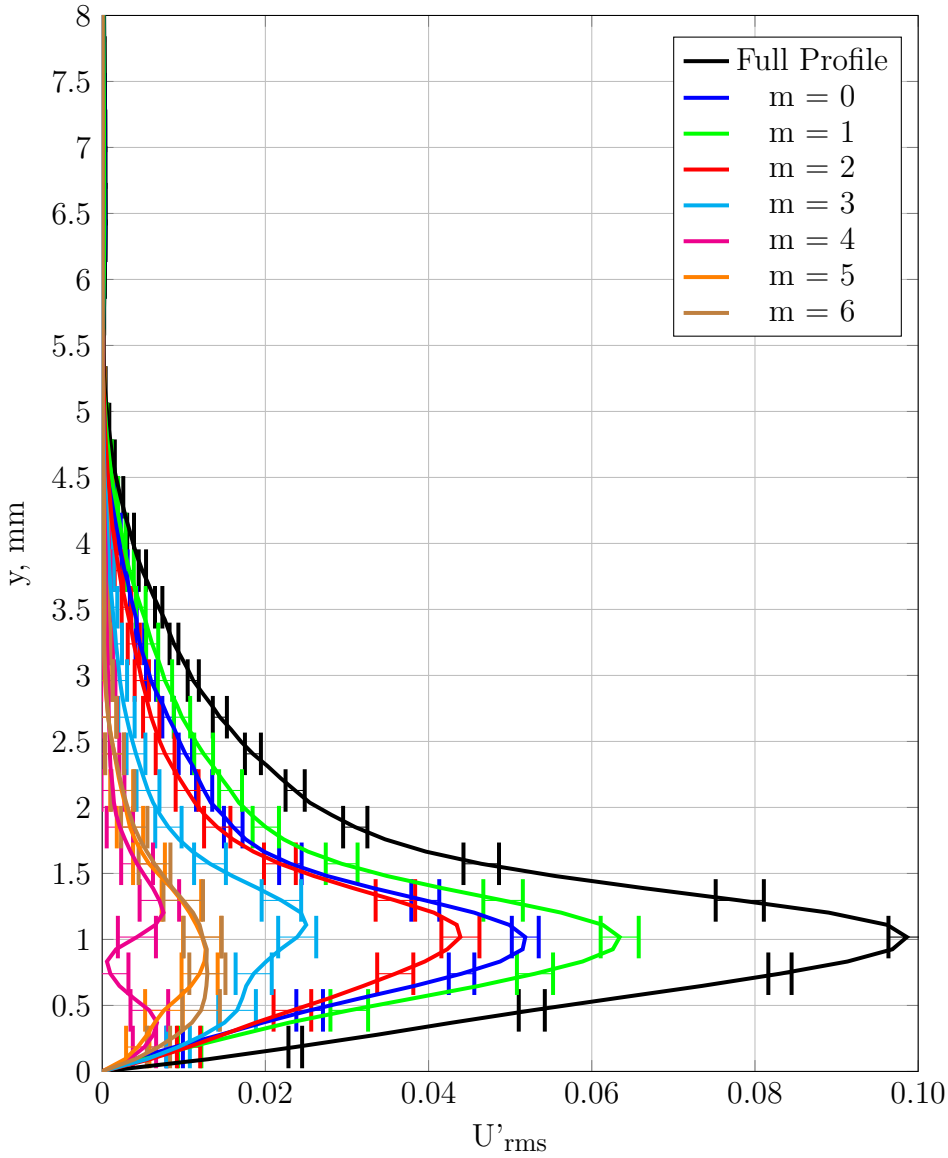

Figure 5.13: Disturbance profiles of different spanwise modes at x = 928 mm for the discrete roughness only configuration at the $Re_k = 220$ condition.

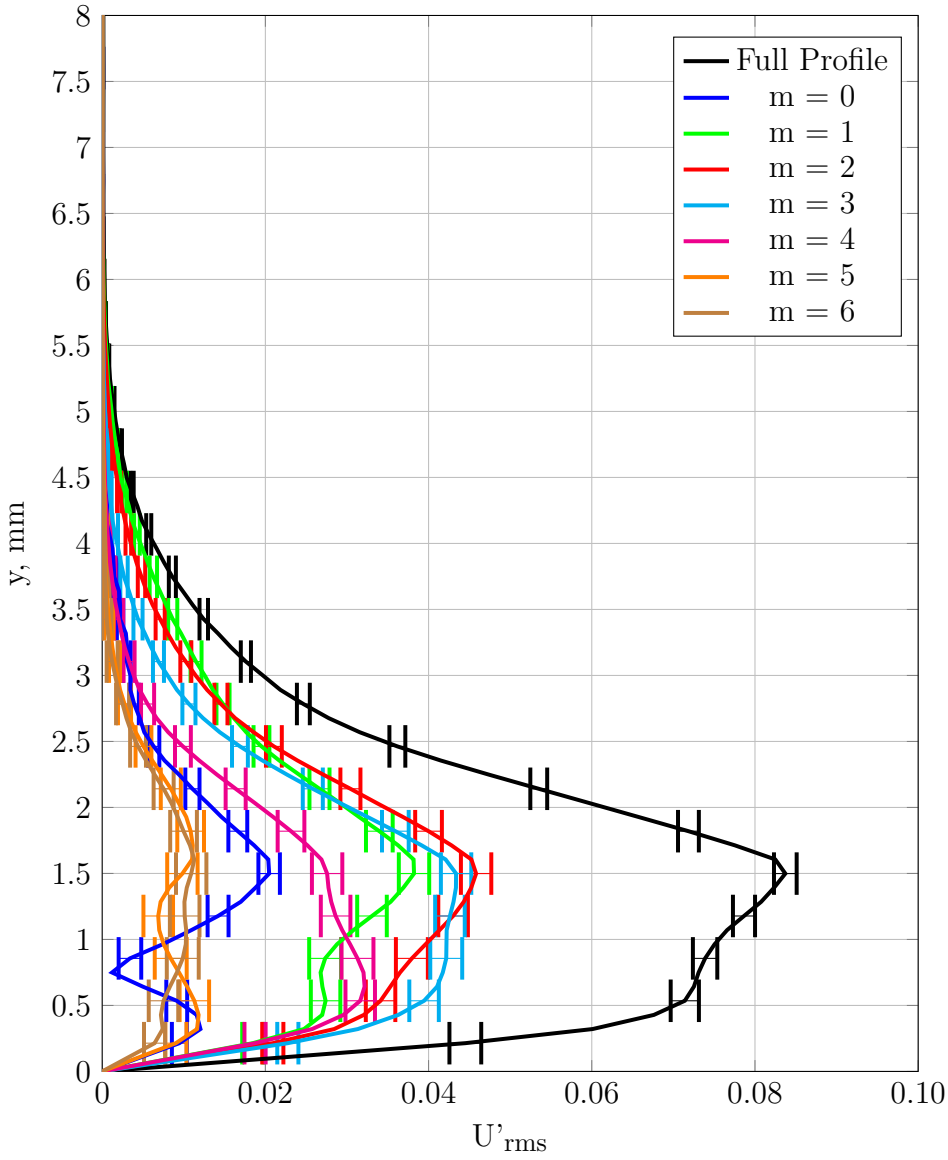

Figure 5.14: Disturbance profiles of different spanwise modes at x = 962.5 mm for the discrete roughness only configuration at the $Re_k = 220$ condition.

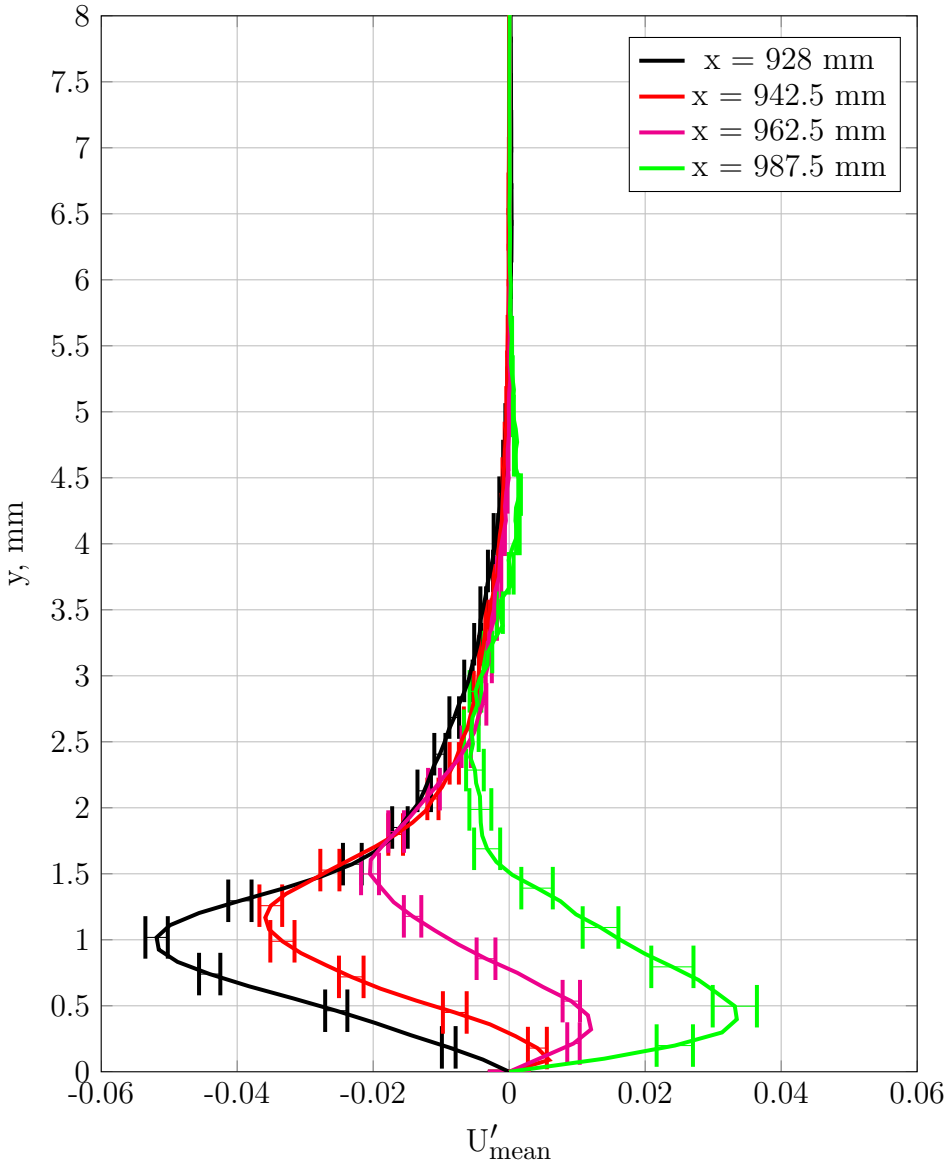

Figure 5.15: U'_{mean} profiles at multiple streamwise locations for the discrete roughness only configuration at the $Re_k = 220$ condition.

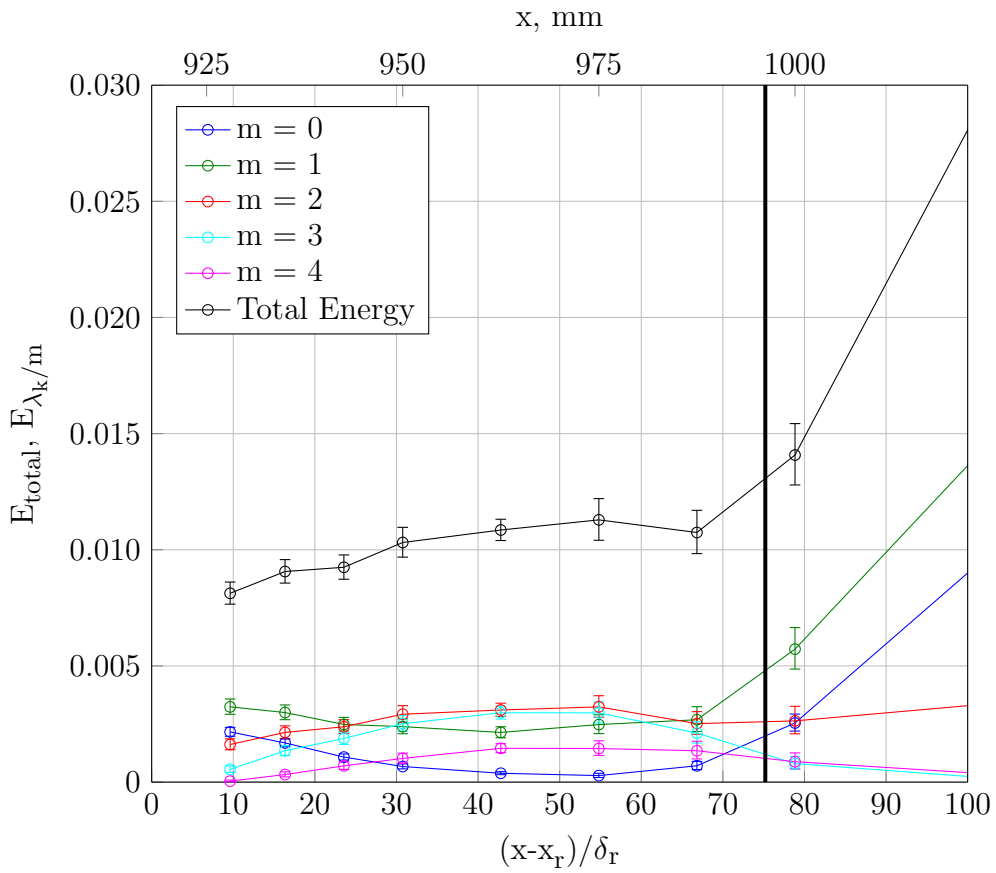

Figure 5.16: Streamwise evolution of disturbance energy for the discrete roughness configuration at the $Re_k = 220$ condition. The solid vertical line indicates the origin of the turbulent wedge.

terns; the m = 0 and m = 1 modes initially decay and then begin to grow, while the shorter wavelengths modes grow before beginning to decay. As the m = 0 and m = 1 modes begin to grow, the turbulent wedge forms and begins to spread.

During the hotwire scans, the time history of each data point is recorded in order to analyze the temporal disturbance frequencies in the roughness wake. At the $Re_k = 151$ condition, the unsteadiness is small; thus, a spectral analysis of the time histories does not provide significant information about the wake. At the $Re_k = 220$ condition, the wake undergoes a secondary instability that leads to transition. This

instability is analyzed by evaluating the temporal power spectra for each hotwire measurements and quantifying the rms unsteadiness associated with the instability's frequency band.

The temporal power spectrum for each point is calculated by the procedure outlined by Press [38], which includes windowing of the signal and spectrum averaging. The power spectrum is normalized so the sum of the energy in all of the frequency bins equals the square of the rms unsteadiness.

$$\sum \mathrm{PSD} = (\mathrm{u}'_{\mathrm{rms}})^2 \tag{5.1}$$

Figure 5.17 shows the temporal power spectrum of fluctuations at (y = 1.7 mm, z = -3 mm), which is near the center of the transitioning roughness wake. At this point in the (y,z) plane, a range of secondary instabilities is seen between 200 Hz and 700 Hz as the wake evolves and transitions to turbulence. Harmonics of the 200-700 Hz range are also seen at higher frequencies.

The unsteadiness between 200 Hz and 700 Hz is extracted by examining the components of the normalized power spectra between those two frequencies.

$$\mathrm{u}'_{\mathrm{rms,200–700}} = \sqrt{\sum_{\mathrm{f=200Hz}}^{\mathrm{700Hz}} \mathrm{PSD}} \tag{5.2}$$

Figure 5.18 shows colored contour plots of the velocity fluctuations between 200 and 700 Hz. At x = 928 mm, a low level of unsteadiness occurs directly behind the roughness element. By x = 962.5 mm, the unsteadiness has grown and is centered around the low speed streak near z = -3 mm. At x = 1000 mm, the unsteadiness outlines the core of the turbulent wedge rather than showing the secondary instability.

These contours of unsteadiness between 200 and 700 Hz can be created for an

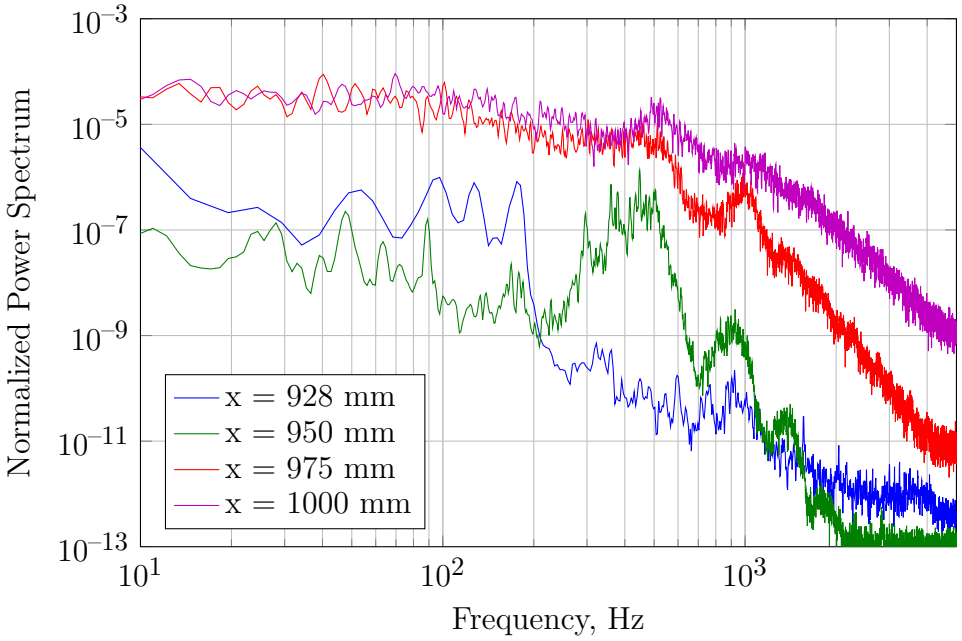

Figure 5.17: Normalized temporal power spectrum near y = 1.7 mm, z = -3 mm at multiple streamwise locations for the discrete roughness only configuration at the $Re_k = 220$ condition

arbitrary frequency band; examining frequencies in a narrow frequency band will make direct comparisons between secondary instability mode shapes at particular temporal frequencies and the unsteadiness observed in the experiment possible.

The total unsteadiness associated with the 200-700 Hz frequency band ($E_{unsteady}$) is calculated by integrating $\left(u'_{rms,200–700}\right)^2$ in the spanwise and normal directions.

$$E_{unsteady} = \left(\frac{1}{\lambda_z}\right)\left(\frac{1}{\delta}\right)\int_0^{\lambda_z}\int_0^{\infty}(u'_{rms,200–700})^2 dydz \tag{5.3}$$

Figure 5.19 shows the growth of $E_{unsteady}$ in the roughness wake. In the near-wake, the instability only grows slightly. In the mid-wake, the instability grows exponentially. $E_{unsteady}$ continues to grow at a slower rate up to the streamwise location where the turbulent wedge forms.

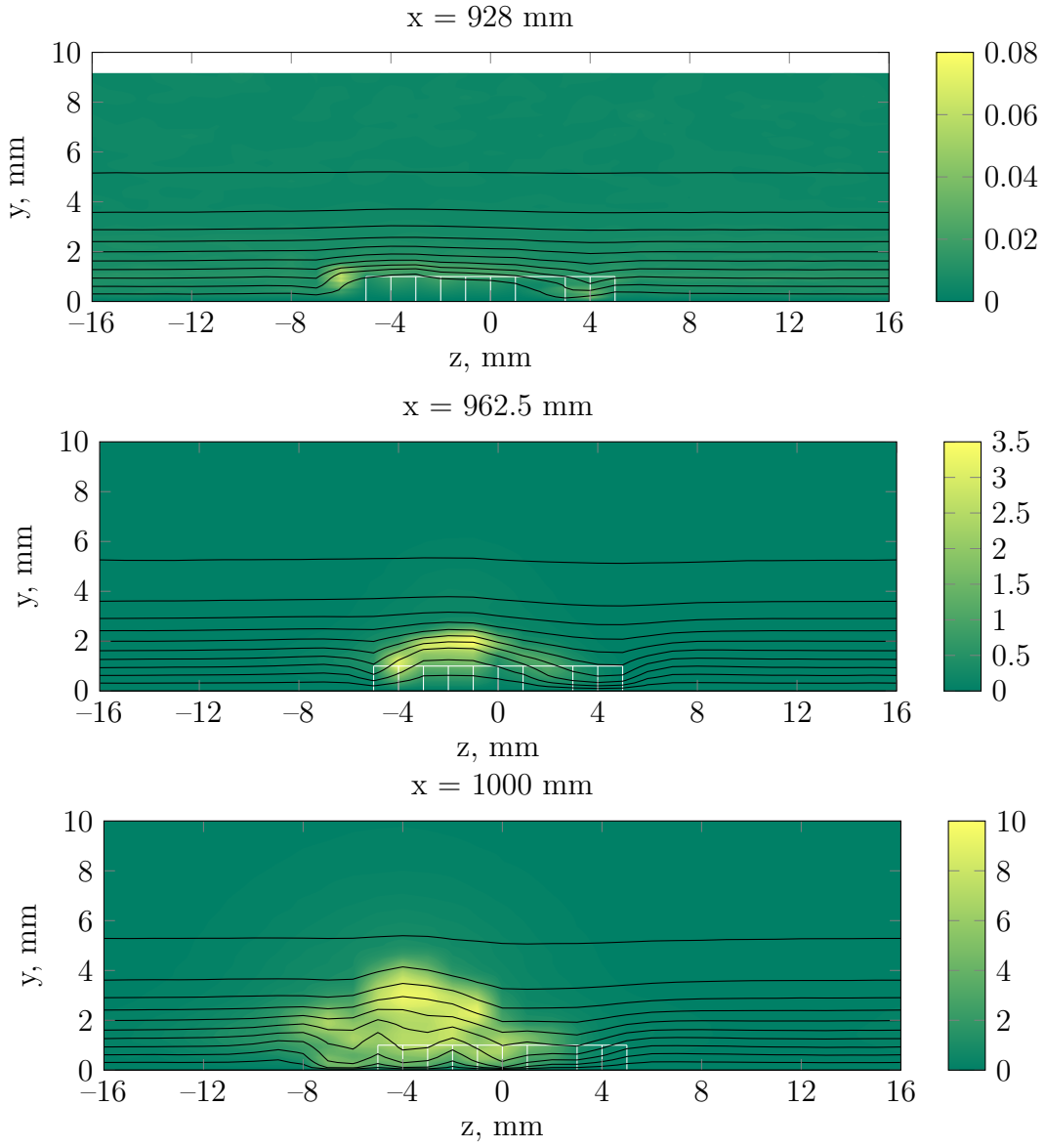

Figure 5.18: Contour plots of steady streamwise velocity (10% increments) colored by $100u'_{rms,200–700}$ at three streamwise locations for the discrete roughness configuration at the $Re_k = 220$ condition.

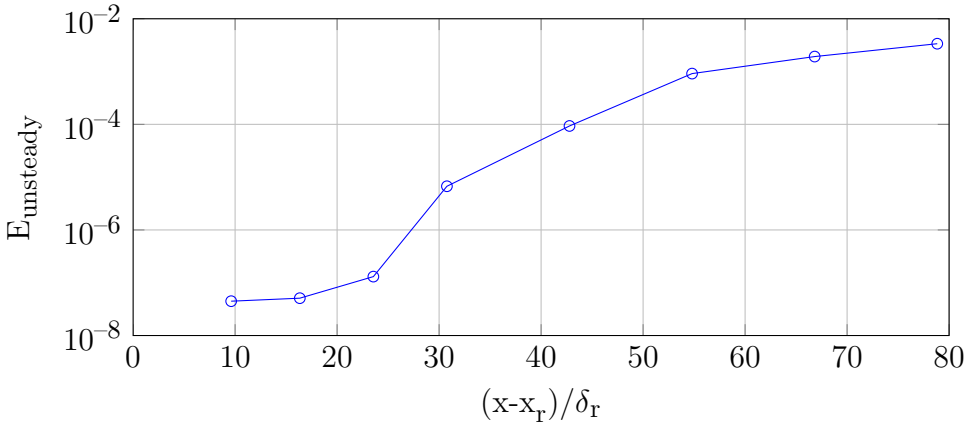

Figure 5.19: Unsteady disturbance energy for the discrete roughness configuration at the $Re_k = 220$ condition

The exponential growth rate of these secondary instabilities has implications for transition control; in order to prevent transition from occurring for this roughness configuration/condition, the mean flow would need to be modified to the point that the growth rate of these instabilities is almost zero. This concept is further examined in Section 7.

6. COMBINED (DISTRIBUTED AND DISCRETE) ROUGHNESS

The third roughness configuration tested was the combination of the discrete roughness and the distributed roughness patch. The distributed roughness begins 878 mm downstream of the leading edge, while the discrete roughness is centered 918 mm downstream of the leading edge.

Naphthalene flow visualization and hotwire measurements were used to analyze the wake of this roughness at two different Reynolds numbers. The lower Reynolds condition ($Re_k = 151|113$) produced a laminar wake, while the higher Reynolds number condition ($Re_k = 220|163$) produced a wake that forms a turbulent wedge $\sim$17 boundary layer thicknesses downstream of the discrete roughness. Table 6.1 shows the details of the two test conditions, which were chosen to match similar test conditions with the different roughness configurations.

6.1 $Re_k = 151|113$ Condition

For the $Re_k = 151|113$ condition, the tunnel was set to the same unit Reynolds number as the lowest Reynolds number condition for the distributed roughness configuration (Condition 1 as shown in Table 4.1) and the lower Reynolds number condition for the discrete roughness configuration (shown in Table 5.1). At this Reynolds

Table 6.1: Test conditions for combined roughness test configuration

Condition	Unit Reynolds Number, 1/mm	Distributed Roughness Height, mm	Discrete Roughness Height, mm	Re_k - Distributed	Re_k - Discrete
Low Re'	544.3	0.85	1.00	113 $\pm$ 16	151 $\pm$ 12
High Re'	690.5	0.85	1.00	163 $\pm$ 19	220 $\pm$ 22

number, the combination of the slanted rectangles and distributed roughness produces a wake similar to the wake observed from the discrete roughness configuration at the same Reynolds number.

6.1.1 Naphthalene Flow Visualization

Figure 6.1 shows naphthalene flow visualization of the combined roughness configuration at the $Re_k = 151|113$ condition. The distributed roughness was covered while the naphthalene spray was being applied to prevent erosion of the rapid-prototyping material. Downstream of the distributed roughness, a complex wake forms that includes a number of high- and low-speed regions. Further downstream, the wake evolves into a single high- and low-speed streak pair, which was observed in the far-wake of the discrete roughness only configuration (shown in Fig. 5.1).

6.1.2 Contour Plots

Hotwire scans were performed at multiple streamwise locations to characterize the transient growth initiated by the combination of the distributed and discrete roughness. Two hotwire scans were performed above the distributed roughness but upstream of the discrete roughness. Eight additional scans were performed over the distributed roughness but downstream of the discrete roughness. Finally, eleven scans were performed downstream of the distributed roughness to characterize the far-wake.

Figure 6.2 shows contour plots of streamwise velocity colored by $100u'_{rms}$. At x = 935 mm, the contours are dominated by the near-wake of the slanted rectangle. By x = 1000 mm, a clear set of low- and high-speed streaks have formed, with increased unsteadiness along the top of the low-speed streak and the bottom of the high-speed streak. In the far-wake, the shorter wavelength disturbances have decayed, and the streaks have broadened in span to influence the area between z = -10 mm and z =

Figure 6.1: Naphthalene flow visualization of combined roughness geometry ($\mathrm{Re_k} = 151|113$)

7 mm. Qualitatively, the contours are similar to the contours shown for the discrete roughness only configuration in Fig. 5.2.

6.1.3 Disturbance Profiles

Figure 6.3 shows total disturbance profiles at multiple streamwise locations, both above and downstream of the distributed roughness. The profiles again show the qualitative behavior of transient growth; the peak disturbance moves away from the wall further downstream while the area under the curve grows between the near-wake and the mid-wake.

The same plot for the discrete roughness only configuration (Fig. 5.3) shows a much larger disturbance profile at x = 928 mm. Part of this difference may be caused by the different cutoff velocities used in the hotwire measurements. For the discrete roughness configuration, the hotwire was used to get near-wall measurements with a velocity cutoff of 10%. With the distributed roughness, the velocity cutoff was set at 18% to avoid running the hotwire into the roughness. The difference in cutoff velocities means that less information is collected in the combined roughness case. With less data near the wall, the disturbance profile will be underestimated if the peak disturbance occurs below the location where the velocity cutoff stops the probe [28]. As the peak of the disturbance profile moves farther away from the wall, the difference in velocity cutoffs becomes less important.

Figure 6.4 shows the first six spanwise disturbance modes at x = 950 mm, while Fig. 6.5 shows the same modes at x = 1400 mm. At x = 950 mm, the modes with longer spanwise wavelengths (m = 1 through m = 3) peak 1.5 mm away from the wall, while shorter wavelength modes peak closer to the wall. The disturbance energy is spread amongst several different modes.

Further downstream, at x = 1400 mm, all of the modes peak approximately 2.4

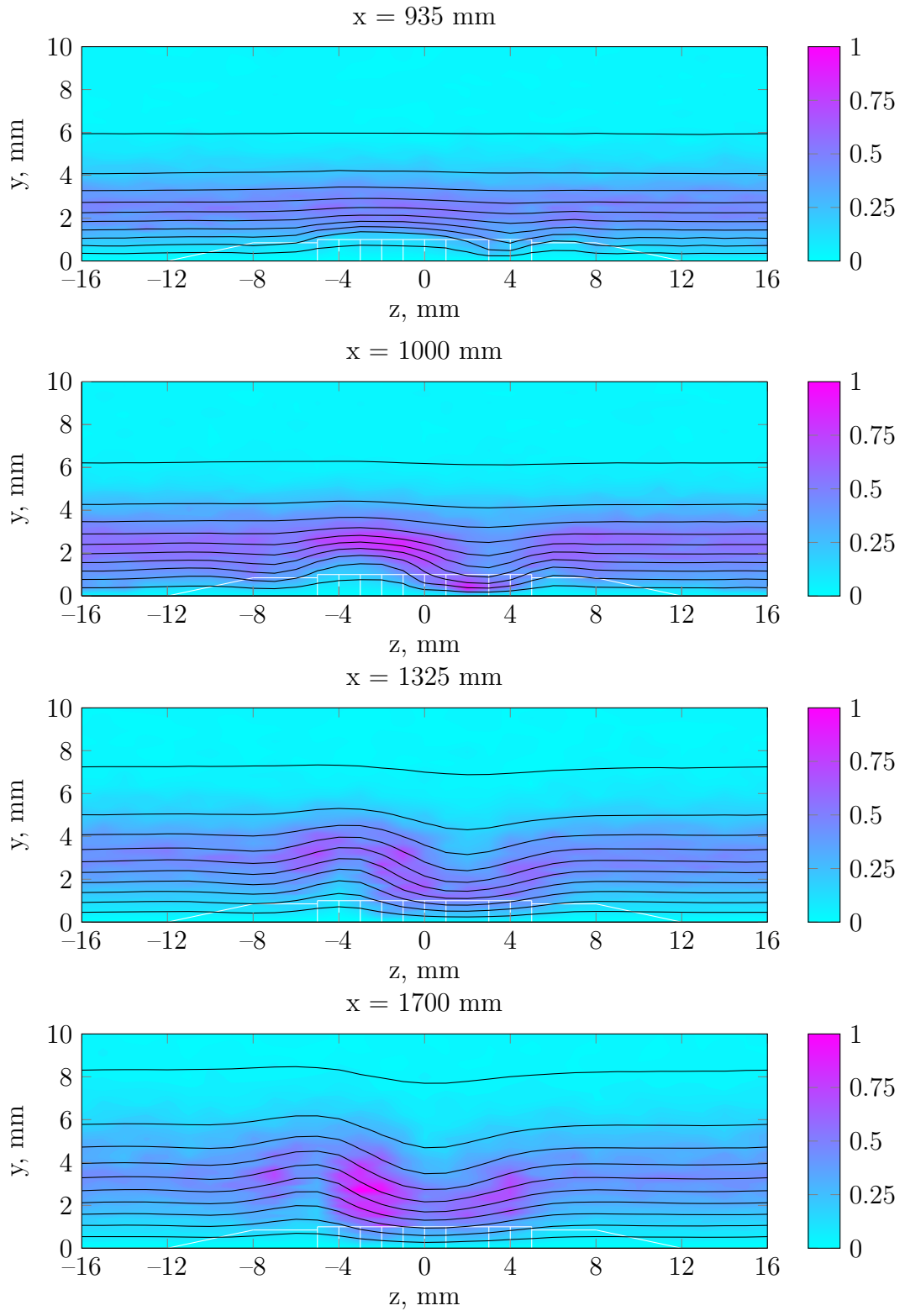

Figure 6.2: Contour plots of steady streamwise velocity (10% increments) colored by $100u'_{rms}$ at four streamwise locations for the combined roughness configuration at the $Re_k = 151|112$ condition.

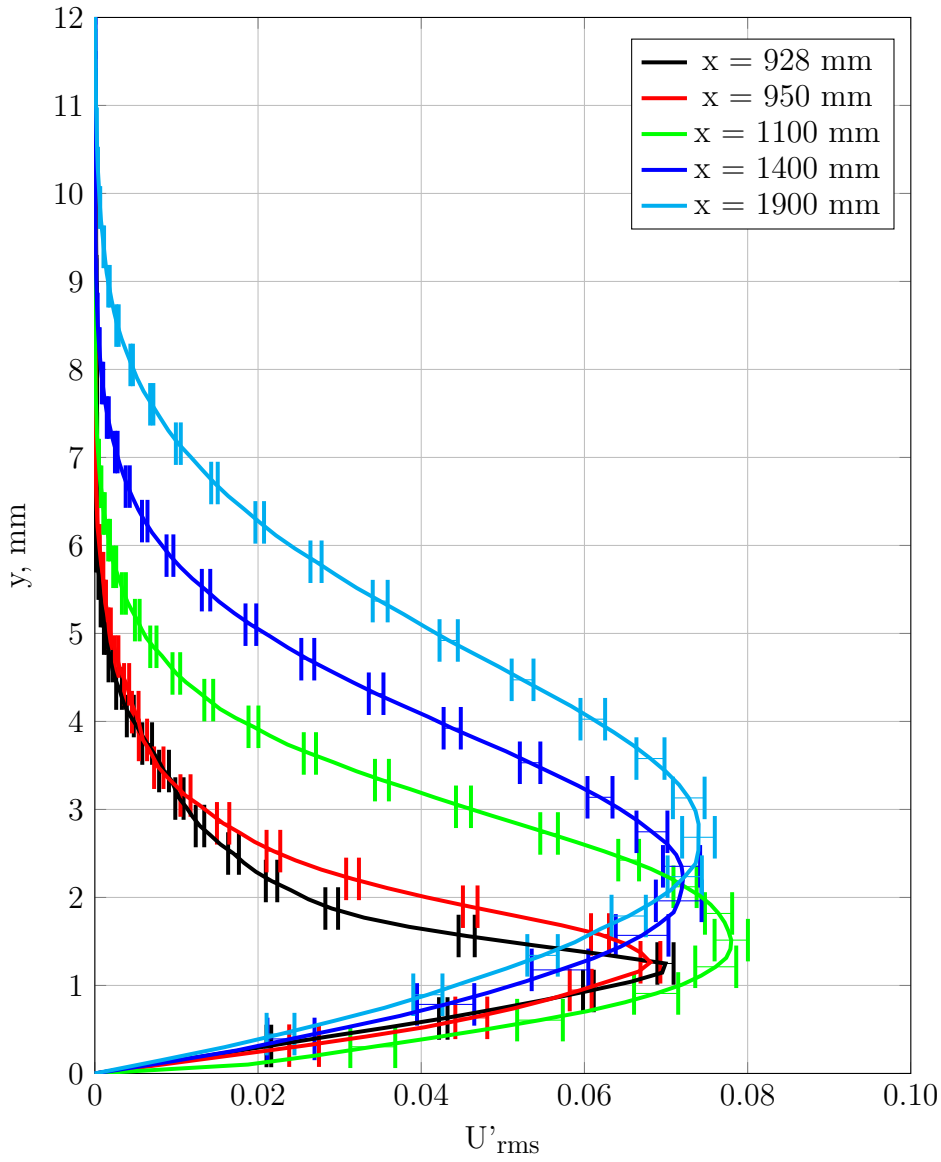

Figure 6.3: Total disturbance profiles at multiple streamwise locations for the combined roughness configuration at the $Re_k = 151|112$ condition.

mm away from the wall. In the discrete roughness only configuration (Fig. 5.6), the m = 1 and m = 2 modes have the largest amplitude, but in the combined roughness configuration (Fig. 6.5), the m = 1 through m = 3 modes all have similar amplitudes. The presence of the distributed roughness has changed the distribution of energy between the different spanwise wavelengths.

The signs and magnitudes of the U'_{mean} profiles further highlights the differences between the two roughness configurations. Figure 6.6 shows the U'_{mean} profiles for the combined roughness configuration, while Fig. 5.4 shows the same plot for the discrete roughness only configuration. The mode is negative at x = 928 mm due to the velocity deficit in the near-wake, but switches sign in the far-wake due to redistribution of streamwise momentum. This pattern occurs for both roughness configurations, but the streamwise location where the profile switches from deficit to excess is different between the two configurations. The presence of the distributed roughness prevents the high-speed streak from penetrating far down into the boundary layer, which is indicates a smaller transfer of high momentum fluid to the bottom of the boundary layer. The x = 1000 mm profile for the combined roughness case barely shows a zero in the profile, while the x = 1000 mm profile in the discrete roughness case shows the presence of the high-speed streak near the wall.

6.1.4 Steady Disturbance Energy

Figure 6.7 shows the streamwise energy evolution of the first five spanwise modes and the total disturbance energy. The beginning and end of the distributed roughness is shown using the dashed vertical lines, while the discrete roughness is located at $(x - x_r)/\delta_r = 0$. The energy growth shows the same qualitative patterns that were observed with the discrete roughness only configuration, but the relative amplitude of the modes has changed. Shorter wavelength disturbances were also measured; the

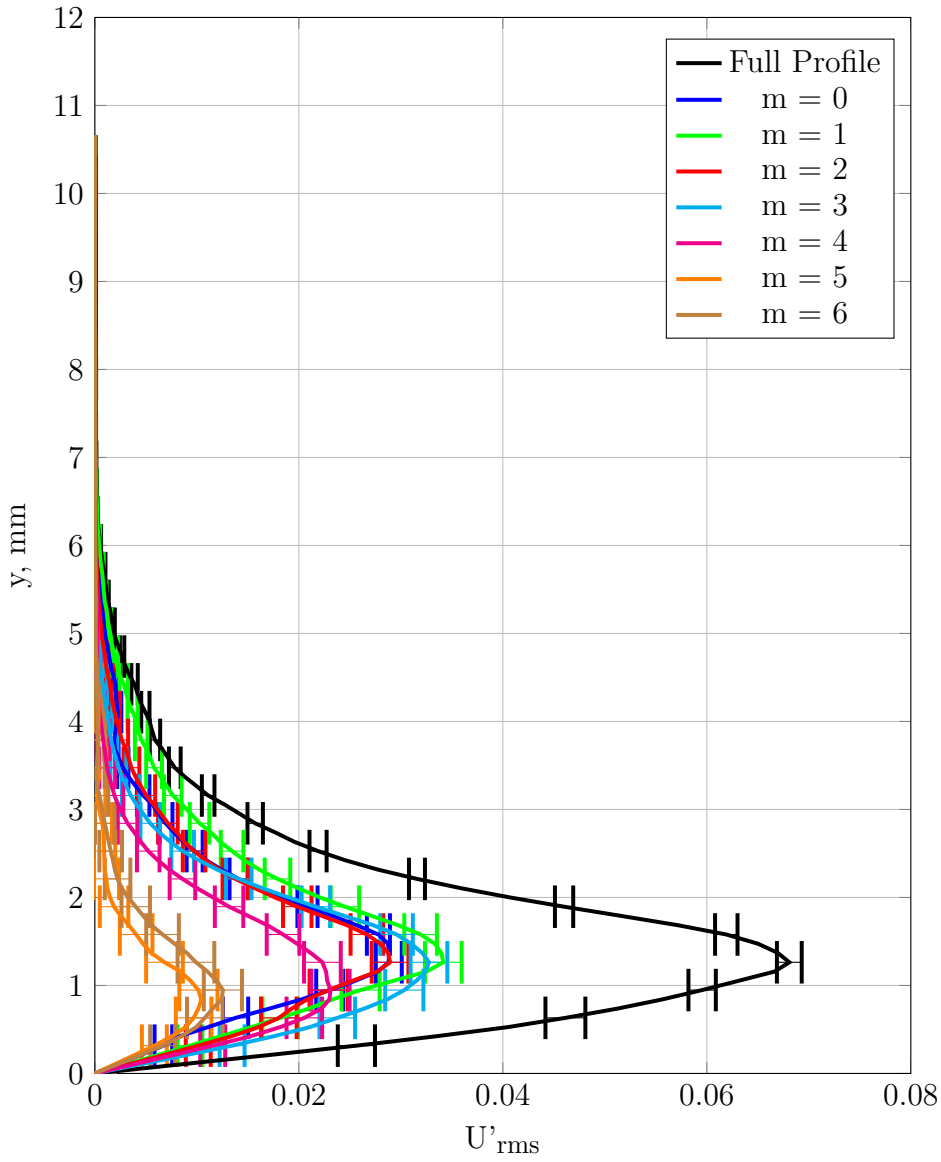

Figure 6.4: Disturbance profiles of different spanwise modes at x = 950 mm for the combined roughness configuration at the $Re_k = 151|112$ condition.

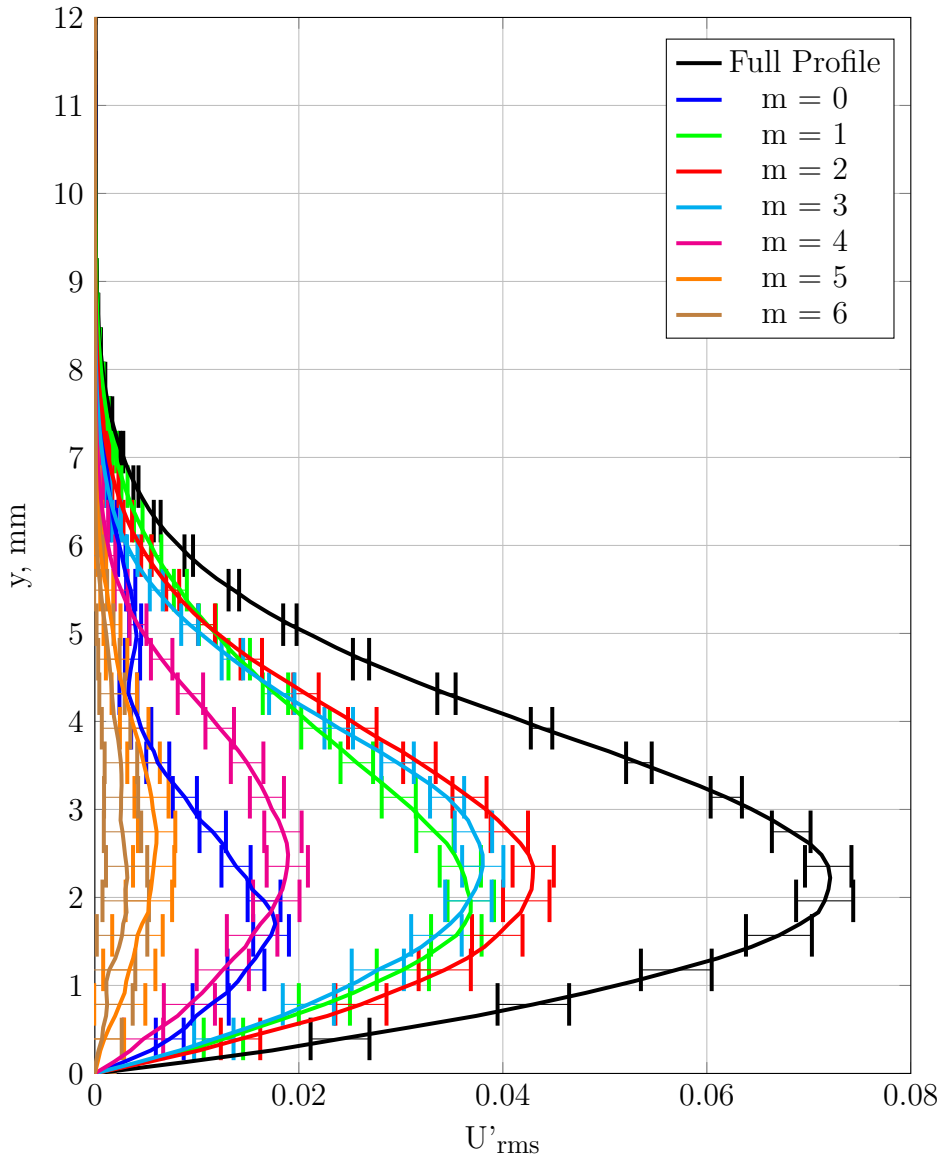

Figure 6.5: Disturbance profiles of different spanwise modes at x = 1400 mm for the combined roughness configuration at the $Re_k = 151|112$ condition.

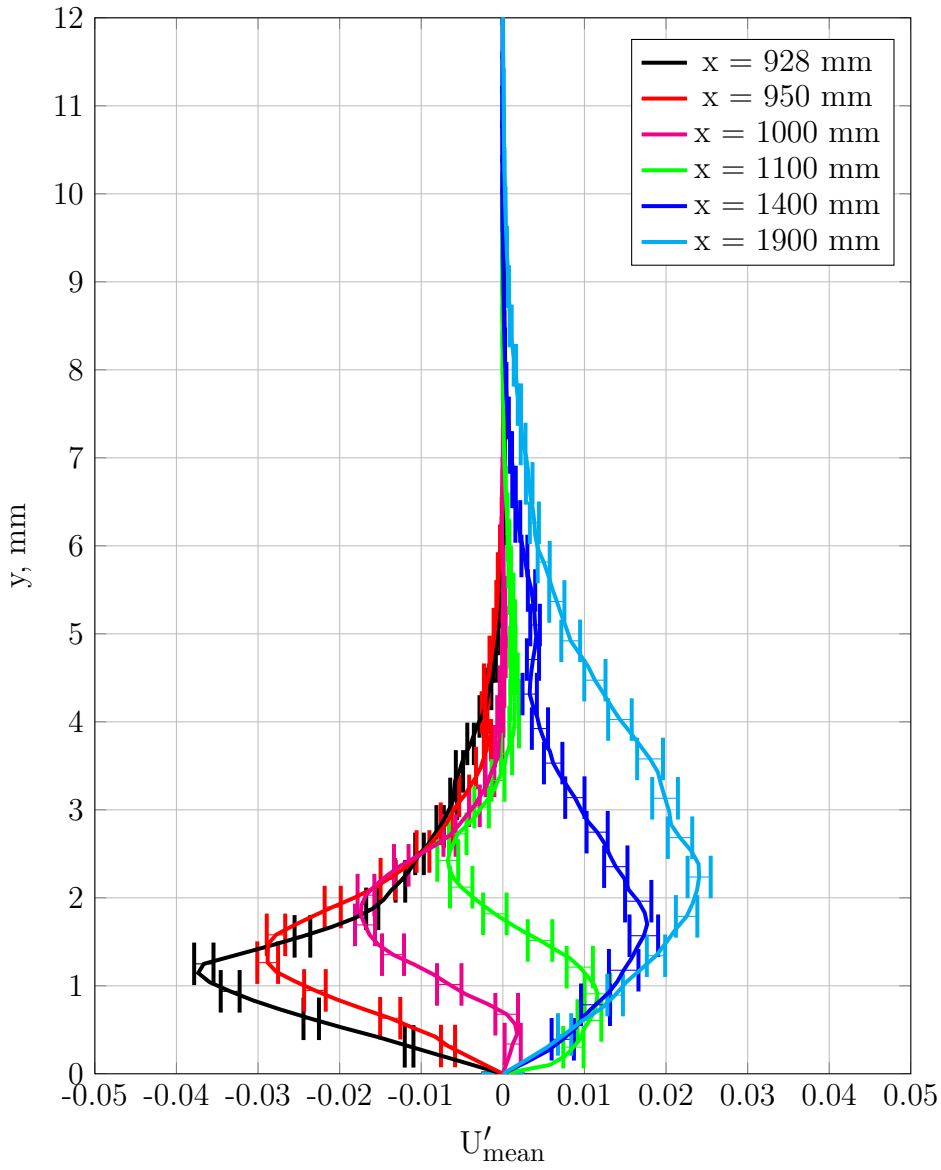

Figure 6.6: U'_{mean} profiles at multiple streamwise locations for the combined roughness configuration at the $Re_k = 151|112$ condition.

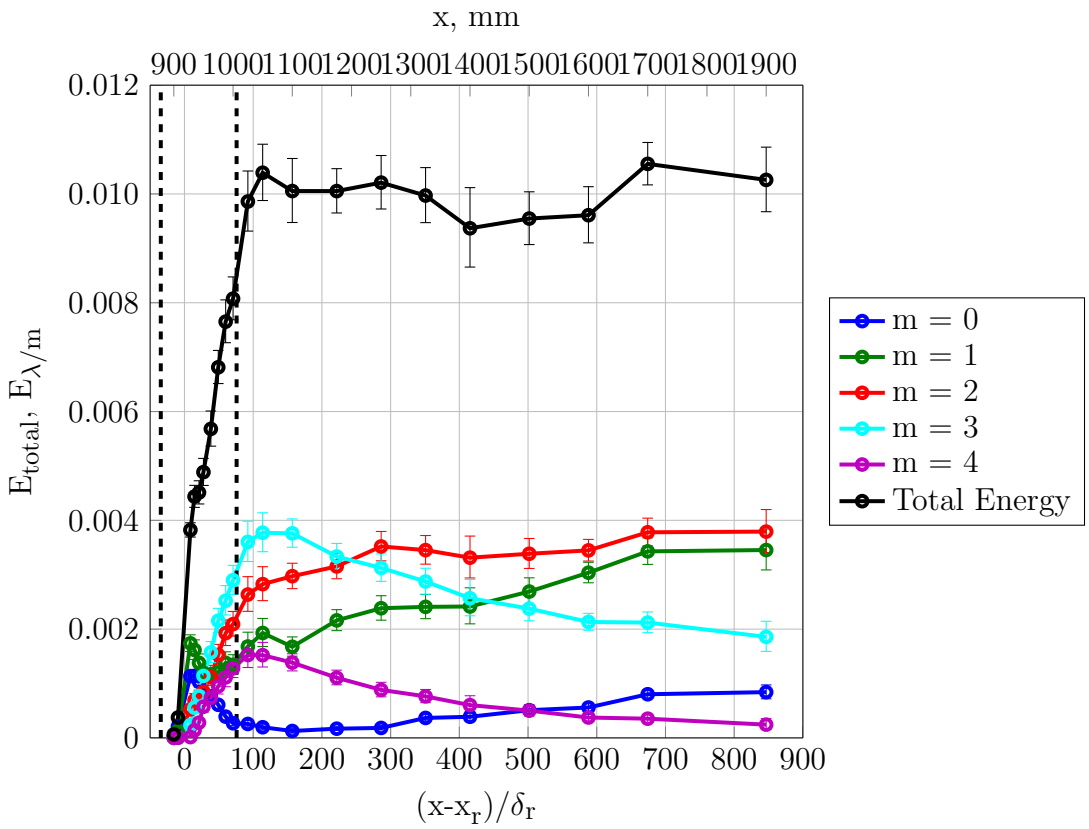

Figure 6.7: Streamwise evolution of disturbance energy for the combined roughness configuration at the $Re_k = 151|112$ condition.

energy evolution for these wavelengths is shown in Fig. 6.8. Section 7 compares the disturbance energy for all three roughness configurations (distributed, discrete, and combined) to investigate how the presence of the distributed roughness effects the receptivity of the discrete roughness.

6.2 $Re_k = 220|163$ Configuration

For the $Re_k = 220|163$ condition, the tunnel was set to the same condition as the middle Reynolds number for the distributed roughness configuration (Condition 2 shown in Table 4.1) and the higher Reynolds number for the discrete roughness configuration (shown in Table 5.1.) At this Reynolds number, the combination of the

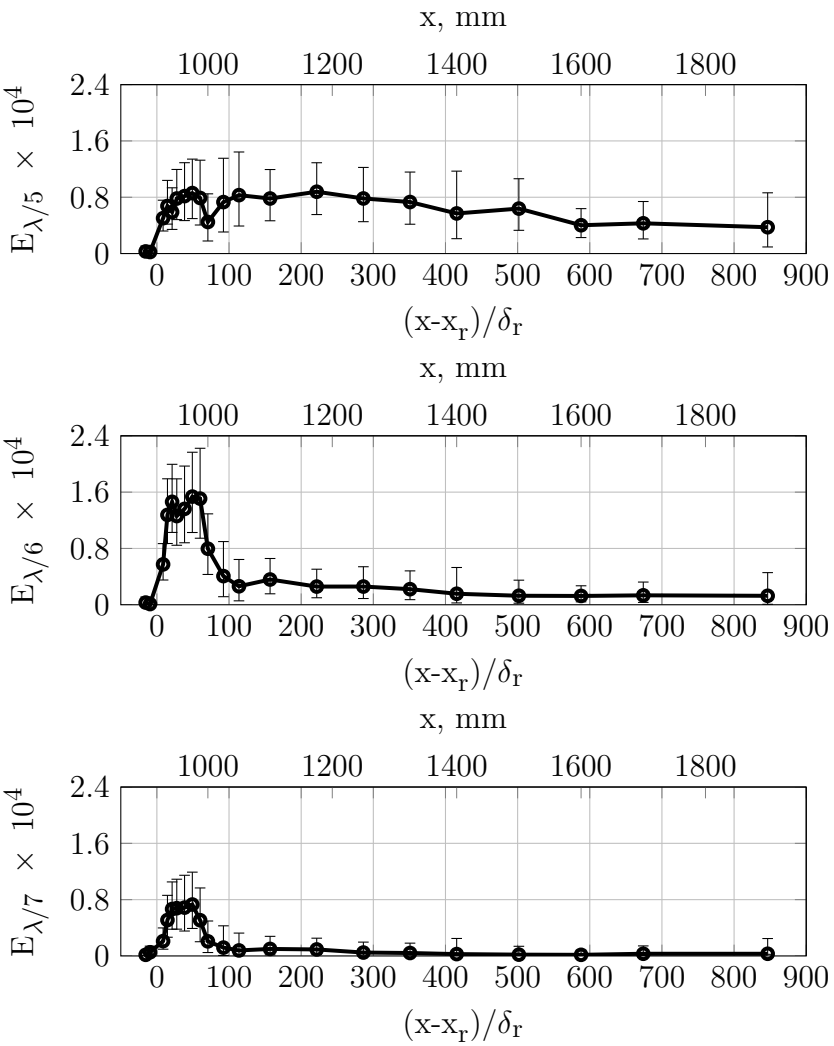

Figure 6.8: Streamwise evolution of disturbance energy for the m = 5 (top), m = 6 (middle), and m = 7 (bottom) spanwise wavelengths for the combined roughness configuration at the $Re_k = 151$ condition.

slanted rectangles and distributed roughness creates an unstable roughness wake that forms a turbulent wedge ∼17 boundary layers downstream of the discrete roughness.

6.2.1 Naphthalene Flow Visualization

Naphthalene flow visualization for the combined roughness configuration at the $Re_k = 220|163$ condition is shown in Fig. 6.9. The structure of the wake over the distributed roughness could not be visualized, but the naphthalene pattern downstream of the distributed roughness shows a wake with multiple high- and low-speed streaks which rapidly evolve into a turbulent wedge. The dogtooth structures at the edge of the wedges make defining the wedge origin and spreading angle difficult. The estimated origin of the turbulent wedge is traced back to x = 1005 mm, which is 9 mm downstream of the origin of the turbulent wedge in the discrete roughness only configuration. By x = 1119 mm, the turbulent wedges have spread across the 32 mm periodicity to create a turbulent boundary layer across the entire span.

6.2.2 Contour Plots

Hotwire scans were performed at multiple streamwise locations to characterize the flow above and downstream of the roughness. Two scans were performed upstream of the discrete roughness while above the distributed roughness. Eight additional scans were performed above the distributed roughness, but downstream of the discrete roughness. Three final scans examined the formation of the turbulent region downstream of the distributed roughness.

Figures 6.10 and 6.11 show contour plots of the roughness wake, starting in the near-wake and progressing through to a near-fully turbulent boundary layer. In the near-wake, the rms temporal fluctuations remain below 1% of the freestream speed. At x = 975 mm, the maximum unsteadiness has grown to 4% of the freestream speed. The addition of the distributed roughness has decreased the unsteadiness between x

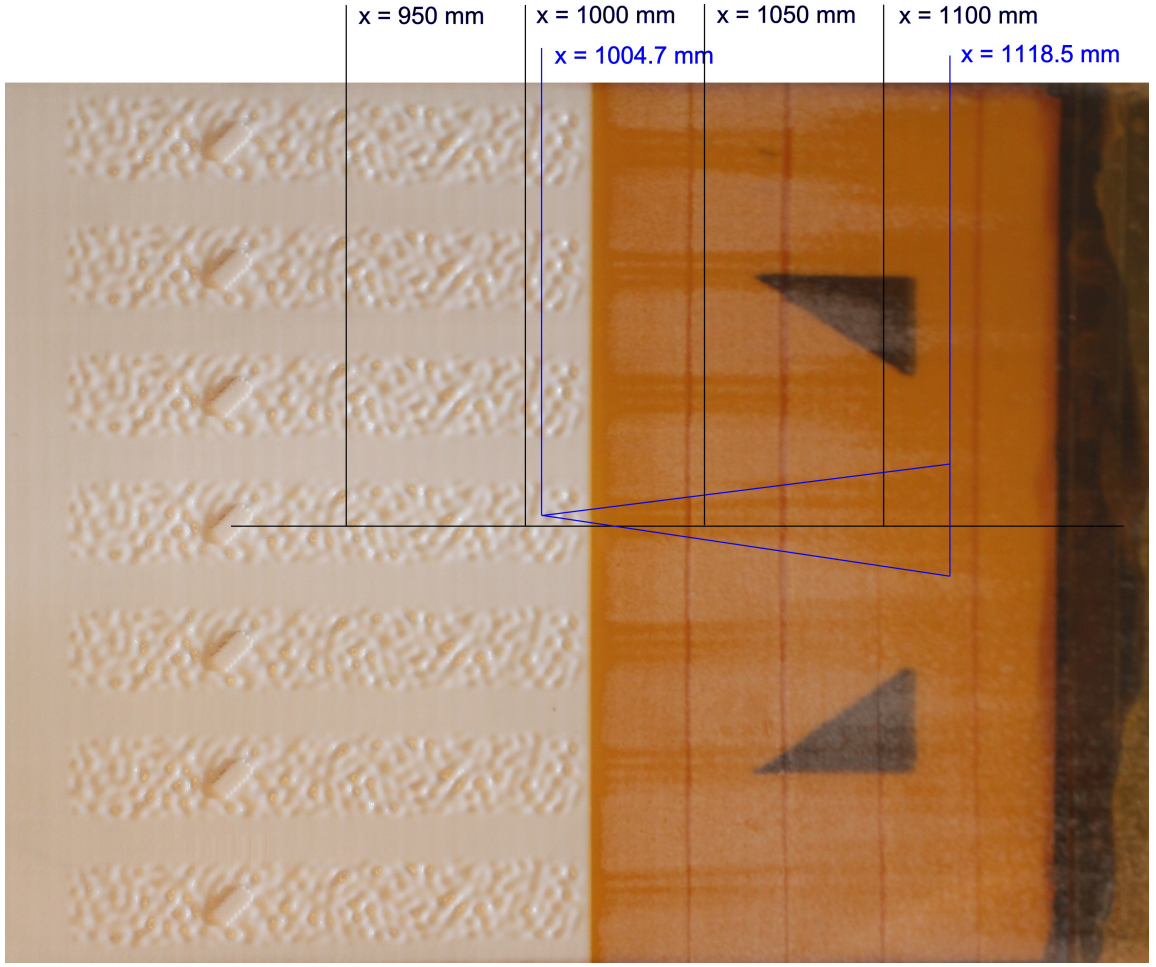

Figure 6.9: Naphthalene flow visualization of combined roughness geometry for the $\mathrm{Re_k} = 220|163$ condition

= 950 mm and x = 975 mm; Fig. 5.10 shows that the maximum rms fluctuations are 2.5% at x = 950 mm and 12% at x = 975 mm. The maximum unsteadiness at these streamwise locations is two to three time smaller for the combined roughness configurations as compared to the discrete roughness configuration.

By x = 1000 mm, a turbulent wedge has almost formed in the wake, and the rms fluctuations are almost 12% of the freestream speed. The spreading of the turbulent wedge can be seen at x = 1050 mm and x = 1100 mm, which are both downstream of the distributed roughness. Comparing the x = 1050 mm contour between Figs. 5.11 and Fig. 6.10 shows that the presense of the distributed roughness has altered the internal structure of the turbulent wedge. In both cases, the maximum unsteadiness occurs at the sides of the wedge.

6.2.3 Disturbance Profiles

Figure 6.12 shows the full disturbance profiles at multiple streamwise locations. The disturbance profiles become more full in the near-wall region as the wake evolves from x = 928 mm to x = 975 mm; however, the double-peak profiles seen with the discrete roughness configuration (Fig. 5.12) have not yet formed. In fact, the shape of the x = 975 mm profile for the combined roughness configuration resembles the shape of the x = 950 mm profile for the discrete roughness configuration. This delay in the evolution of the disturbance profiles confirms the delay in transition observed with the flow visualization.

Figures 6.13 and 6.14 show the disturbance profiles for several spanwise disturbance modes at x = 928 mm and x = 962.5 mm, respectively. At x = 928 mm, the peak disturbance may not be fully resolved due the velocity cutoff used over the distributed roughness (21% at this Reynolds number). The disturbances at the longer spanwise wavelengths have the largest amplitudes. By x = 962.5 mm, several of the

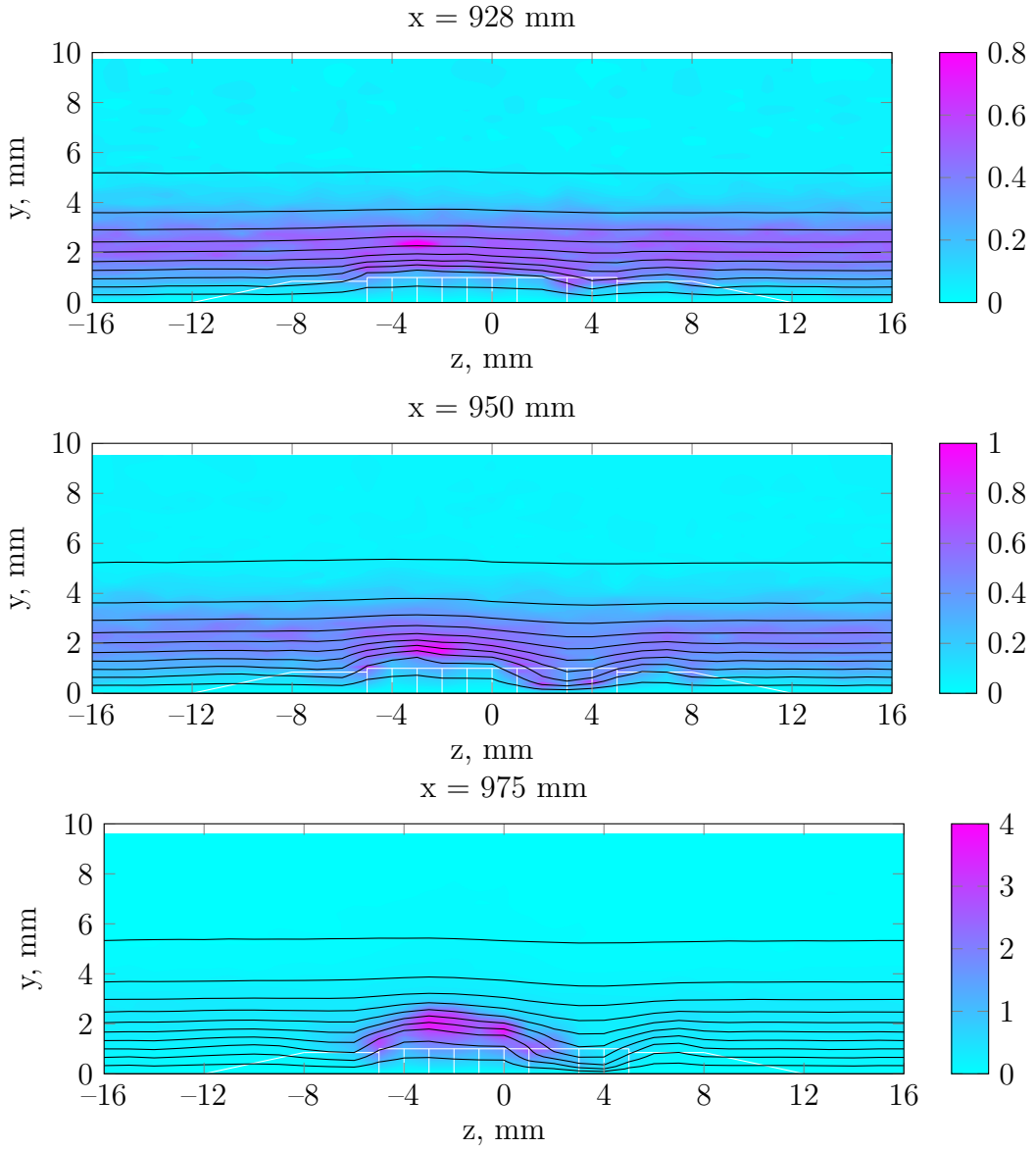

Figure 6.10: Contour plots of steady streamwise velocity (10% increments) colored by $100u'_{rms}$ at three streamwise locations for the combined roughness configuration at the $Re_k = 220|163$ condition.

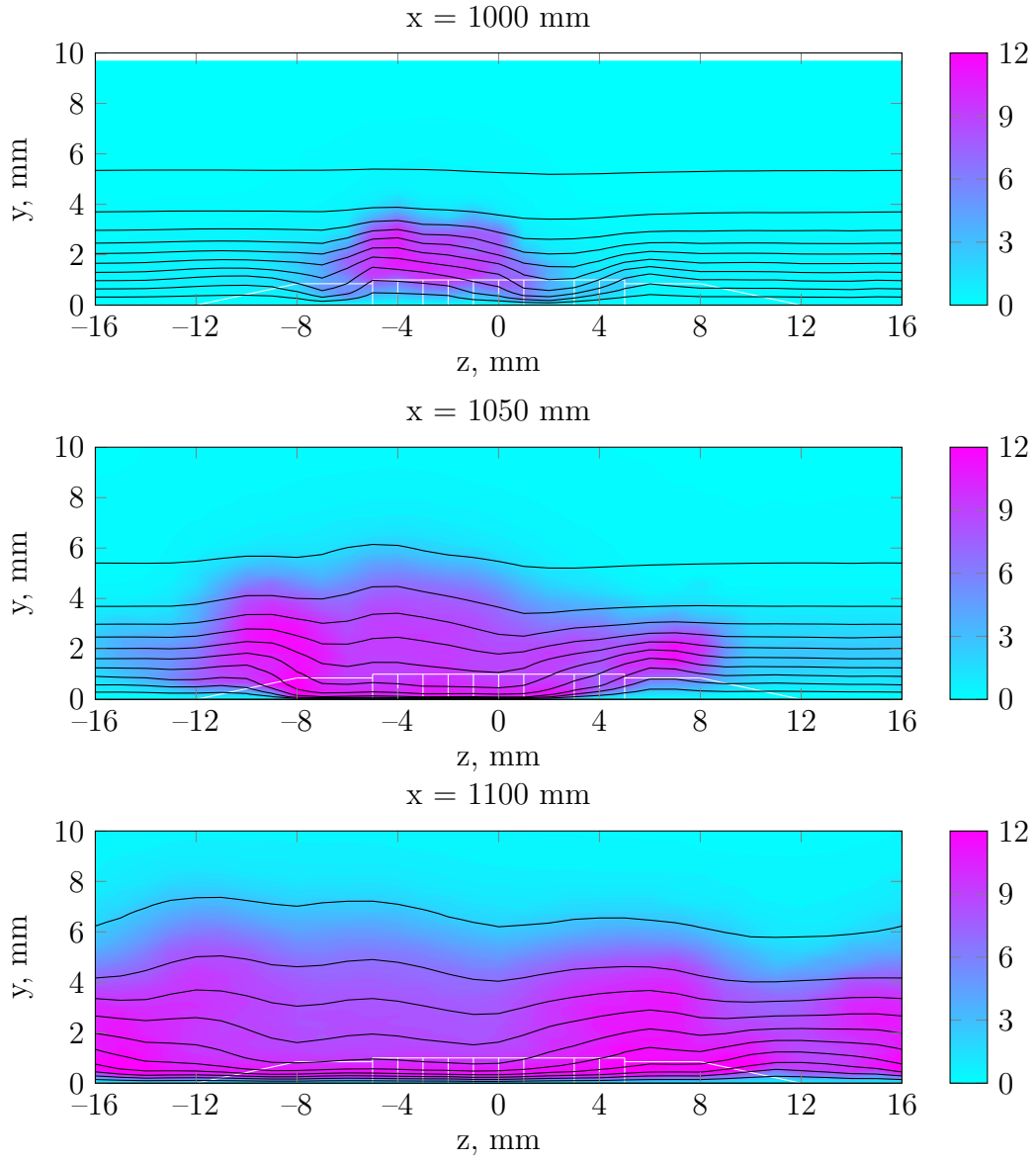

Figure 6.11: Contour plots of steady streamwise velocity (10% increments) colored by $100u'_{rms}$ at three additional streamwise locations for the combined roughness configuration at the $Re_k = 220|163$ condition.

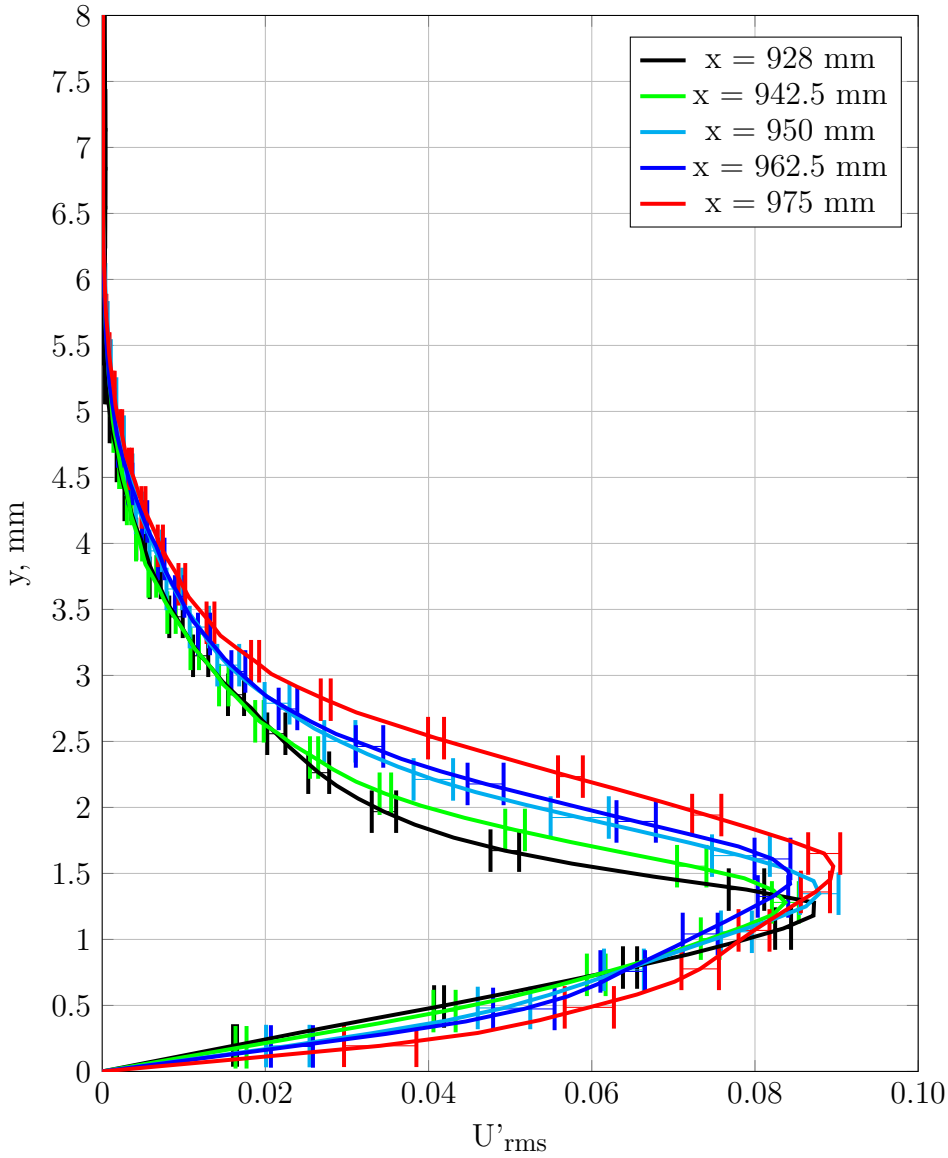

Figure 6.12: Full disturbance profiles at multiple streamwise locations for the combined roughness configuration at the $Re_k = 220|163$ condition.

profiles show a double-peak structure, which indicates the beginning of non-linearity. The disturbances at shorter spanwise wavelengths (m = 2 and m = 3) have grown to the largest amplitudes, while the m = 0 has a zero value around 0.3 mm away from the wall.

Finally, Figure 6.15 shows the U'_{mean} profiles at multiple streamwise locations. The profiles switch from deficit to excess farther downstream than for the equivalent discrete roughness case (shown in Fig. 5.15.) The profile at x = 942.5 mm shows a velocity deficit, while the same plot for the discrete roughness configuration shows a positive U'_{mean} disturbance close to the wall.

Based on observations of the two roughness cases, the transition location is linked to the shape of the U'_{mean} profiles. In both roughness configurations, the turbulent wedge forms shortly downstream of the point where the the m = 0 profile switches from predominately negative to predominately positive. As the high-speed streak penetrates the bottom of the boundary layer, disturbance energy accumulates over a broad range of spanwise wavelengths which, in turn, creates the double-peak profiles seen in Fig. 5.12. The distributed roughness slows down the rate at which the high-speed streak penetrates the bottom of the boundary layer. Eventually, the high-speed streak forms near the wall, and the turbulent wedge forms shortly downstream.

6.2.4 Steady and Unsteady Disturbance Energy

Figure 6.16 shows the streamwise evolution of the disturbance energy before the turbulent wedge forms. In the wake of the discrete roughness, the m = 2 through m = 4 modes grow, while the m = 0 and m = 1 modes decay. The m = 3 mode reaches a maximum amplitude near x = 975 mm and begins to decay before the turbulent wedge forms. The origin of the wedge occurs within a few millimeters of the end of the distributed roughness.

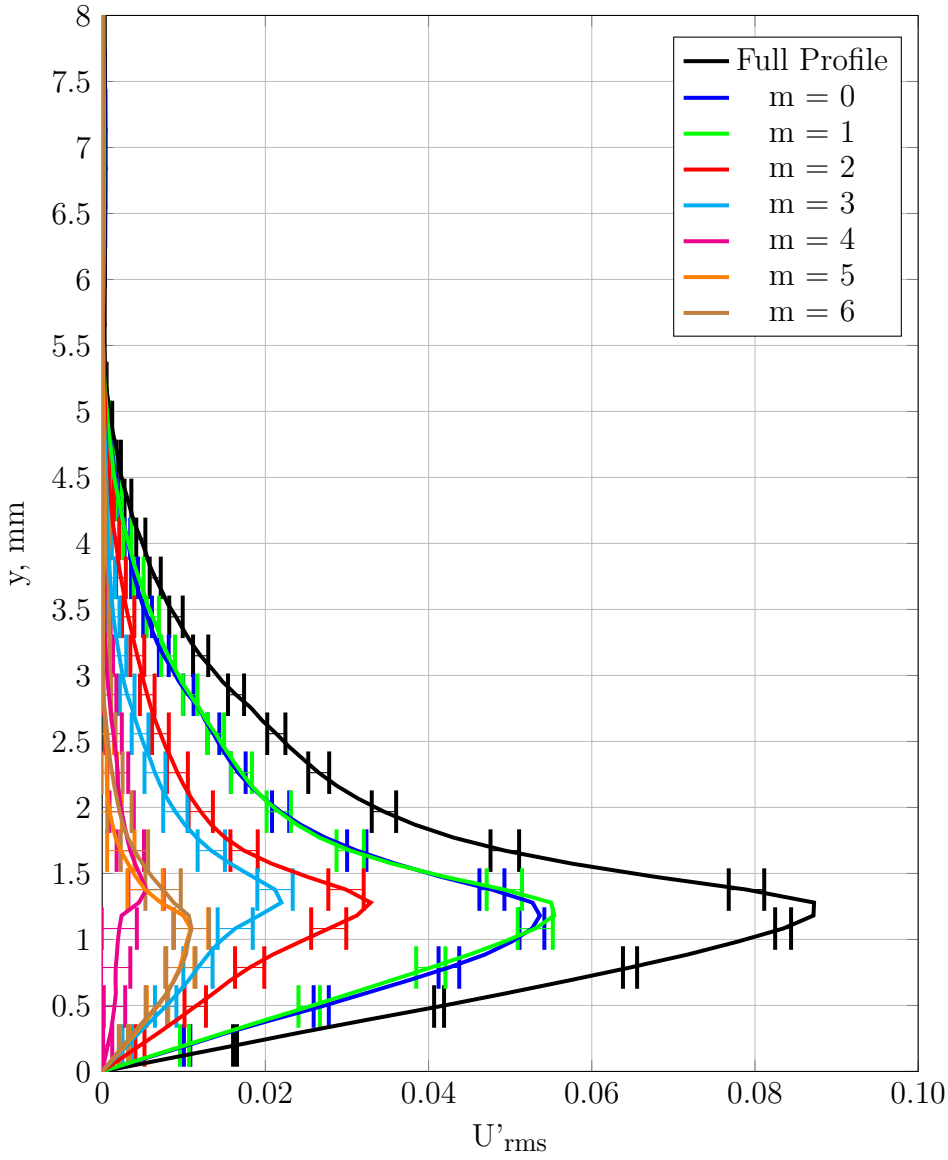

Figure 6.13: Disturbance profiles of different spanwise modes at x = 928 mm for the combined roughness configuration at the $Re_k = 220|163$ condition.

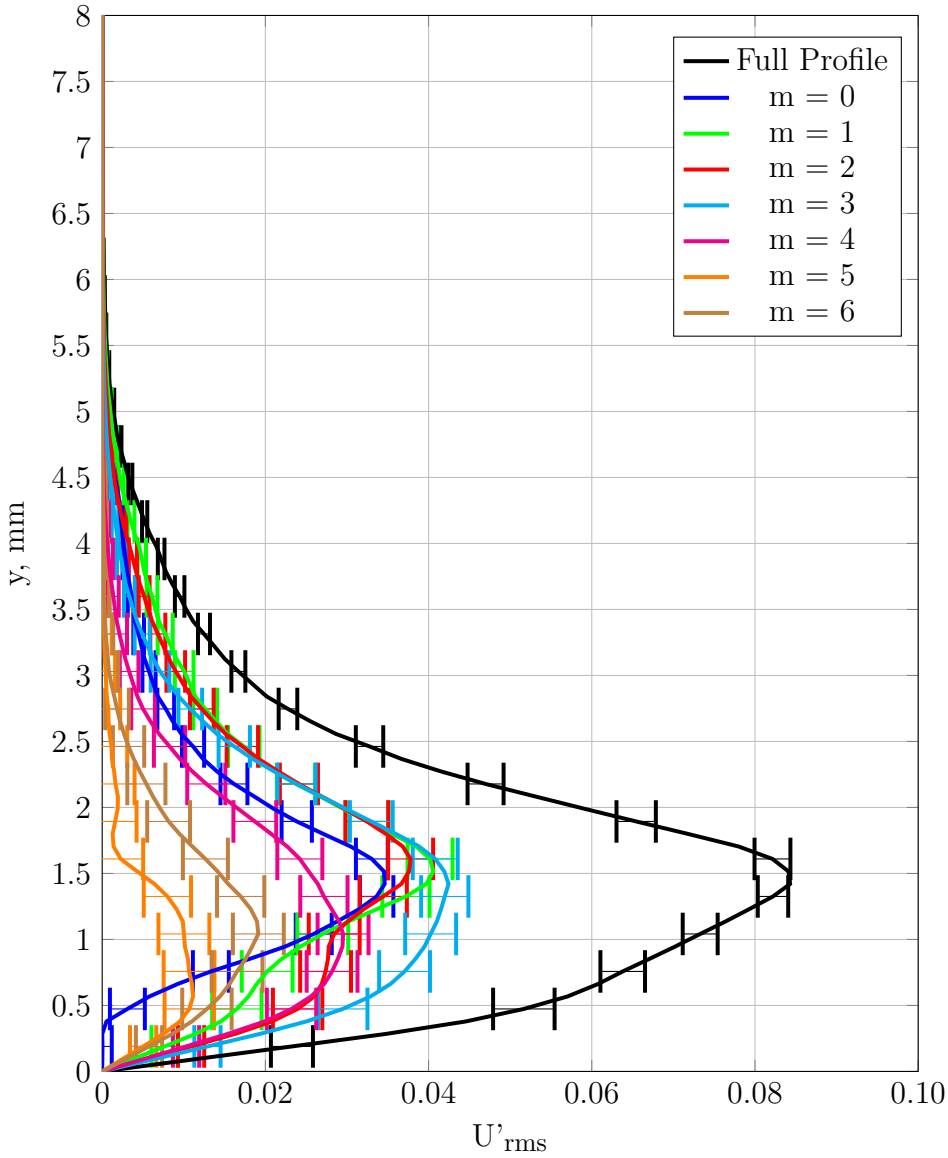

Figure 6.14: Disturbance profiles of different spanwise modes at x = 962.5 mm for the combined roughness configuration at the $Re_k = 220|163$ condition.

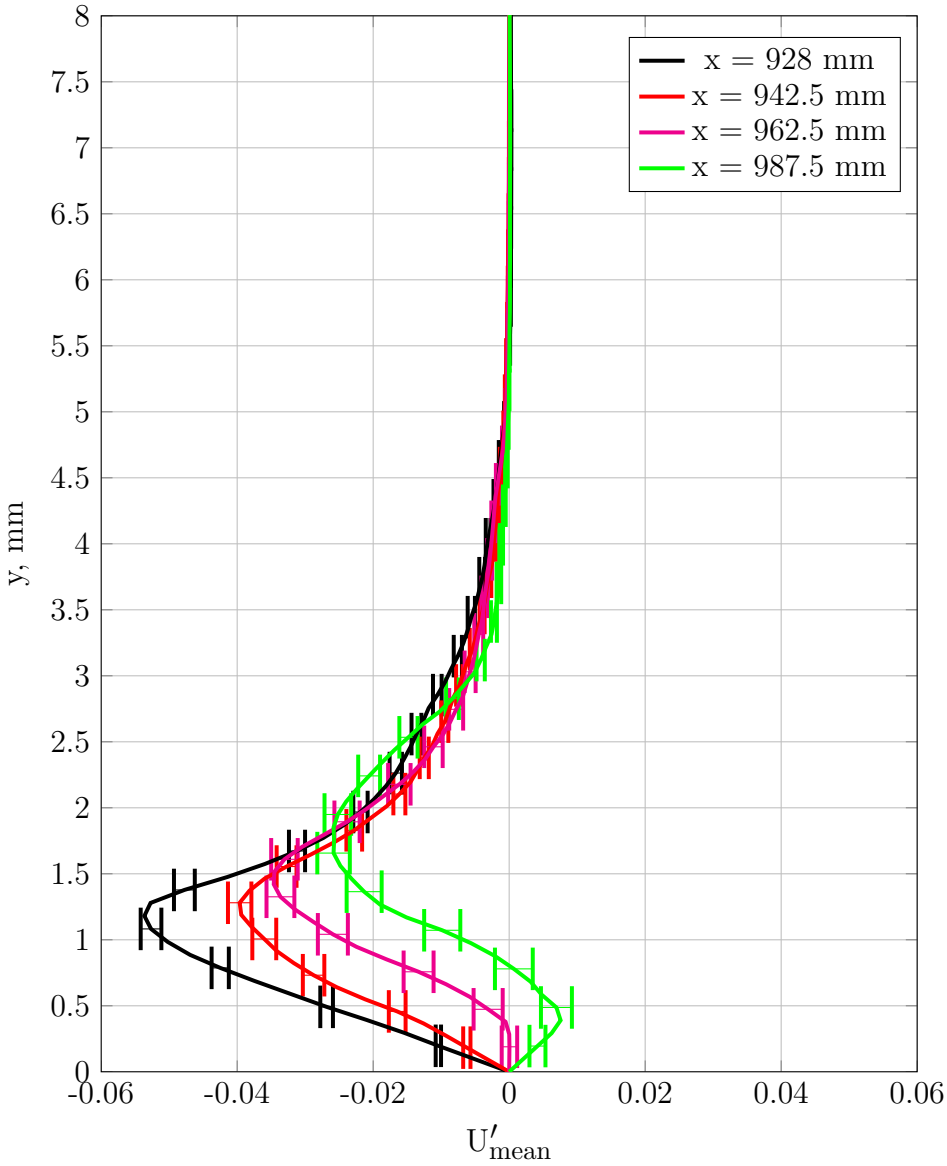

Figure 6.15: U'_{mean} profiles at multiple streamwise locations for the combined roughness configuration at the $Re_k = 220|163$ condition.

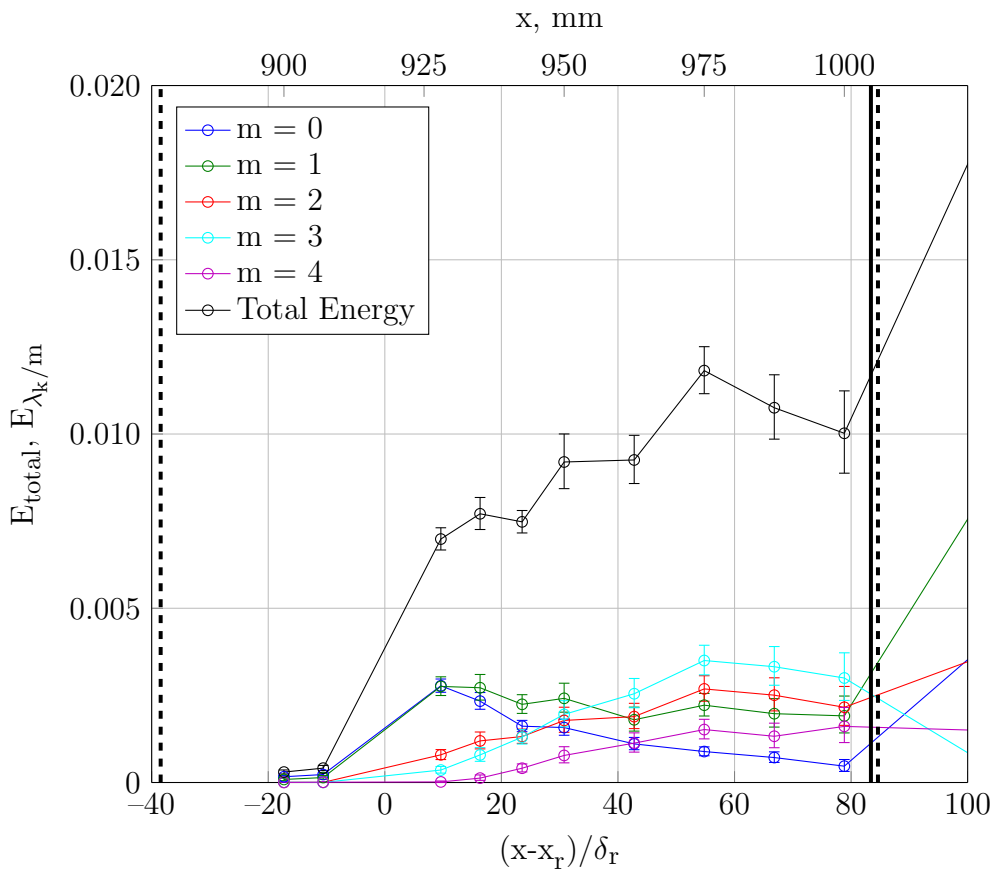

Figure 6.16: Streamwise evolution of disturbance energy for the combined roughness configuration at the $Re_k = 220|163$ condition. The dashed lines indicate the region with the distributed roughness, while the solid vertical line indicates the origin of the turbulent wedge.

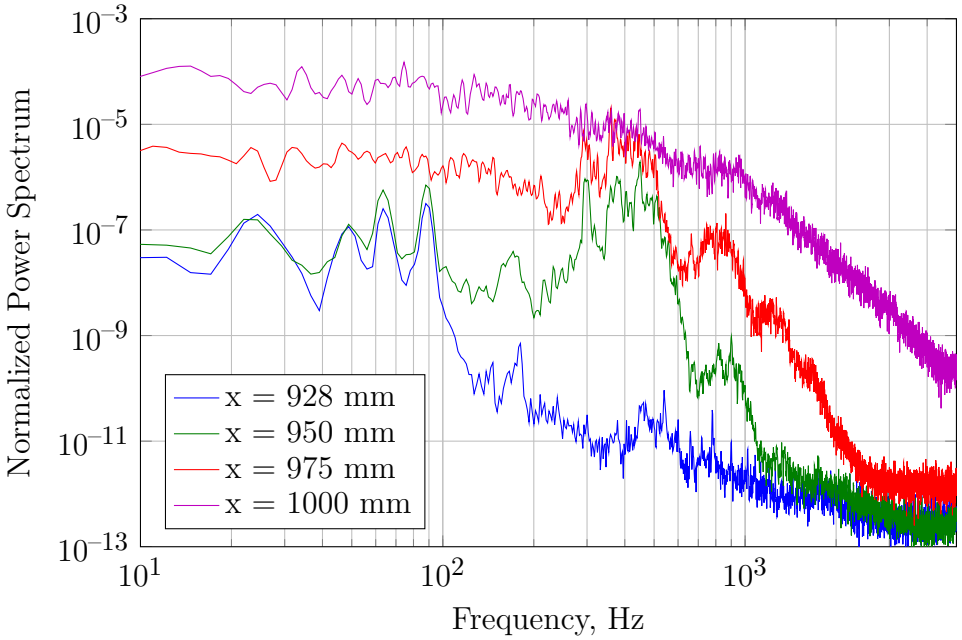

Figure 6.17: Normalized temporal power spectrum near y = 1.7 mm, z = –3 mm at multiple streamwise locations for the combined roughness only configuration at the $Re_k = 220|163$ condition

Figure 6.17 shows the temporal power spectrum of fluctuations at (y = 1.7 mm, z = -3 mm). The spectra show that the 200-700 Hz is associated with the secondary instabilities that lead to transition. A comparison of the spectra at x = 975 mm between Fig. 6.17 and Fig. 5.17, which shows the equivalent spectra for the discrete roughness only configuration, shows that the spectra from the discrete roughness only configuration become turbulent farther upstream than the spectra from the combined roughness configuration.

Figure 6.18 shows colored contour plots of the velocity fluctuations between 200 and 700 Hz, similar to what is shown in Fig. 5.18 for the discrete roughness configuration. At x = 928 mm, a low level of unsteadiness occurs 1 mm away from the wall that is most likely associated with shedding off of the top of the roughness

element. By x = 962.5 mm, the unsteadiness has grown, and the mode shape has several different lobes that are positioned around the low-speed streak. At x = 1000 mm, the turbulent wedge has formed, and the center of the wedge contains large amplitude fluctuations in the 200-700 Hz range.

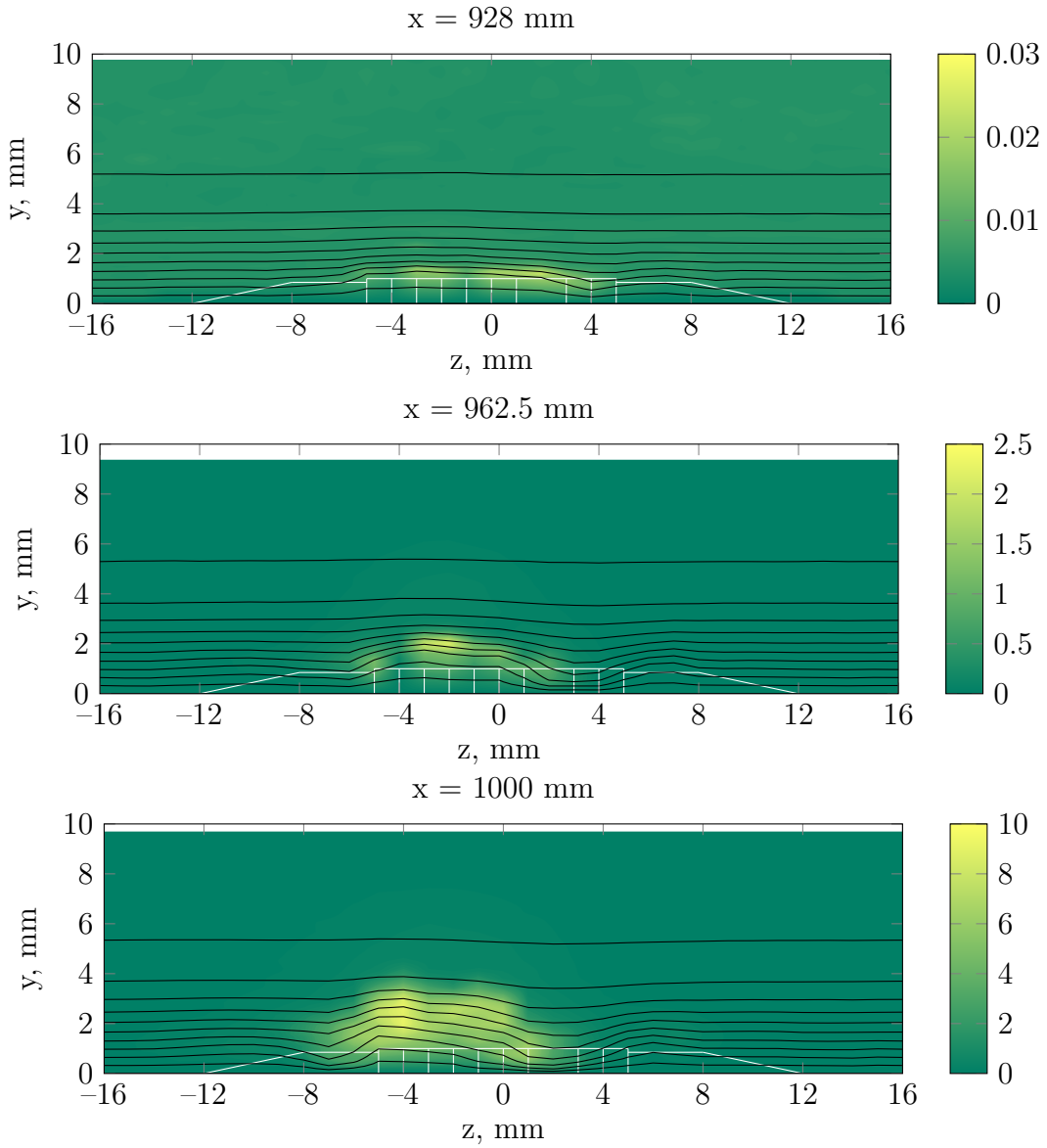

Figure 6.18: Contour plots of steady streamwise velocity (10% increments) colored by $100u'_{rms,200-700}$ at three streamwise locations for the combined roughness configuration at the $Re_k = 220|163$ condition.

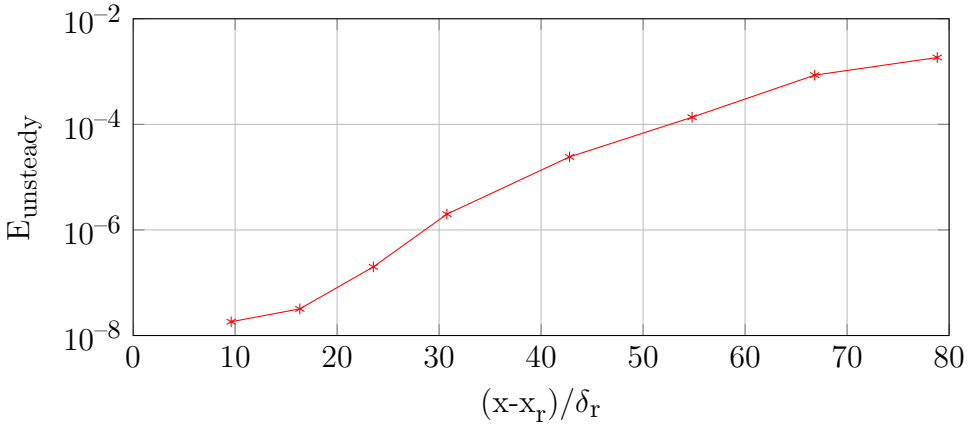

Figure 6.19: Unsteady disturbance energy for the combined roughness configuration at the $Re_k = 220|163$ condition

Figure 6.19 shows the growth of the integrated unsteady energy ($E_{unsteady}$). The unsteadiness is extremely small in the near-wake but grows exponentially throughout the near- and mid-wake before the growth rate slows just upstream of the formation of the turbulent wedge. Even though the distributed roughness changed the structure of the roughness wake, the secondary instabilities still underwent exponential growth and grew large enough to cause transition.

7. COMPARISON OF ROUGHNESS CONFIGURATIONS

Sections 4, 5, and 6 analyzed the flow above and downstream of the three roughness configurations (distributed roughness only, discrete roughness only, and combined roughness). In this section, the steady and unsteady disturbances created by the different configurations are compared in order to better understand how the distributed and discrete roughness interact with each other.

7.1 Steady Disturbance Energy

The steady disturbance energy describes how the different types of roughness distort the basic state boundary layer. The evolution of the total disturbance energy (and the energy associated with different spanwise modes) details the roughness wake and dictates whether or not the wake transitions to turbulence. The steady disturbance energy is shown for both the low Reynolds number condition ($\mathrm{Re}_{\mathrm{k}_{\mathrm{distributed}}} = 113$, $\mathrm{Re}_{\mathrm{k}_{\mathrm{discrete}}} = 151$) and the higher Reynolds number condition ($\mathrm{Re}_{\mathrm{k}_{\mathrm{distributed}}} = 163$, $\mathrm{Re}_{\mathrm{k}_{\mathrm{discrete}}} = 220$).

7.1.1 Lower Reynolds Number

At the lower Reynolds number, all three roughness configurations created a laminar wake that underwent transient growth. Figure 7.1 shows the total disturbance energy for all three configurations. The most obvious feature of this plot is the relative magnitude of the energy from the distributed roughness case compared to the configurations with the discrete roughness. The distributed roughness energy is 10 to 100 times smaller than the energies from the other roughness configurations. This trend is also seen when the disturbance is decomposed into spanwise wavelengths. Because the distributed roughness disturbances are much smaller than the other

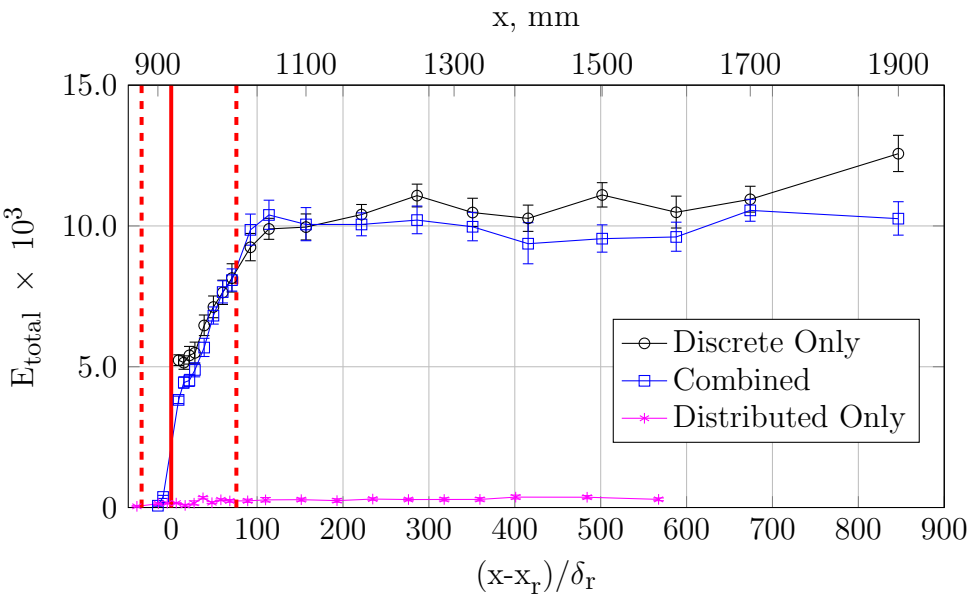

Figure 7.1: Comparison of total disturbance energy for the three roughness configurations at the lower Reynolds number configuration

disturbances, the remainder of the dissertation will focus on the energy from the discrete roughness and combined roughness configurations.

The total energy shows a slight shielding effect for this sub-critical roughness case. The energy in the near-wake and mid-wake is almost identical; however, in the far-wake, the combined roughness configuration shows slightly less disturbance energy.

Figures 7.2 through 7.7 show comparisons of the disturbance energy at the first six spanwise wavelengths. The total energy shows a moderate shielding effect in the far-wake, but the decomposition into different spanwise wavelengths shows that the presence of the distributed roughness amplifies some of the disturbance modes while suppressing others. In particular, the longer spanwise wavelength modes (m = 0 through m = 2) are suppressed, shorter wavelength modes (m = 3 and m = 4) are amplified, and the m = 5 mode is only mildly affected.

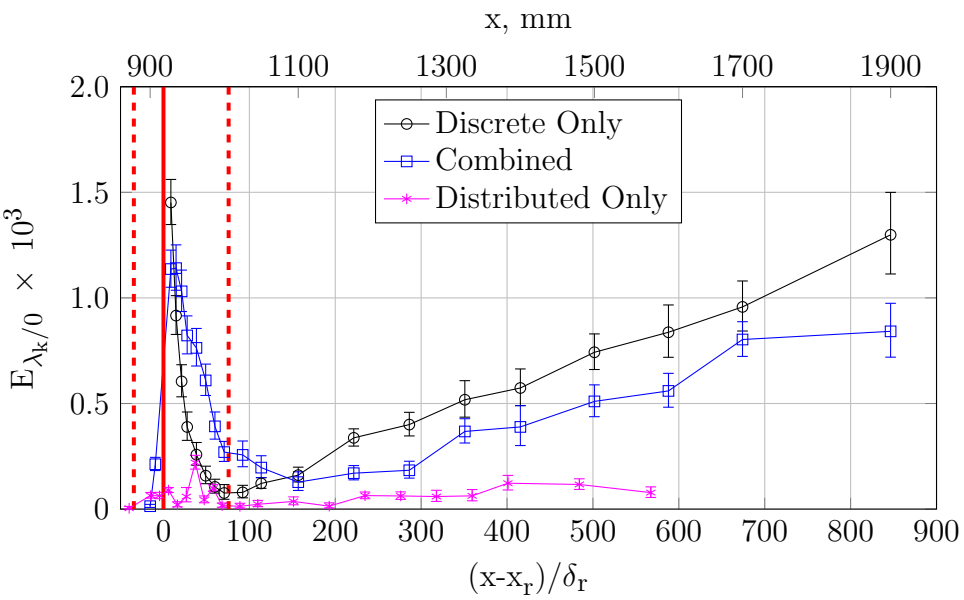

Figure 7.2: Comparison of the disturbance energy of the m = 0 mode for the three roughness configurations at the lower Reynolds number condition

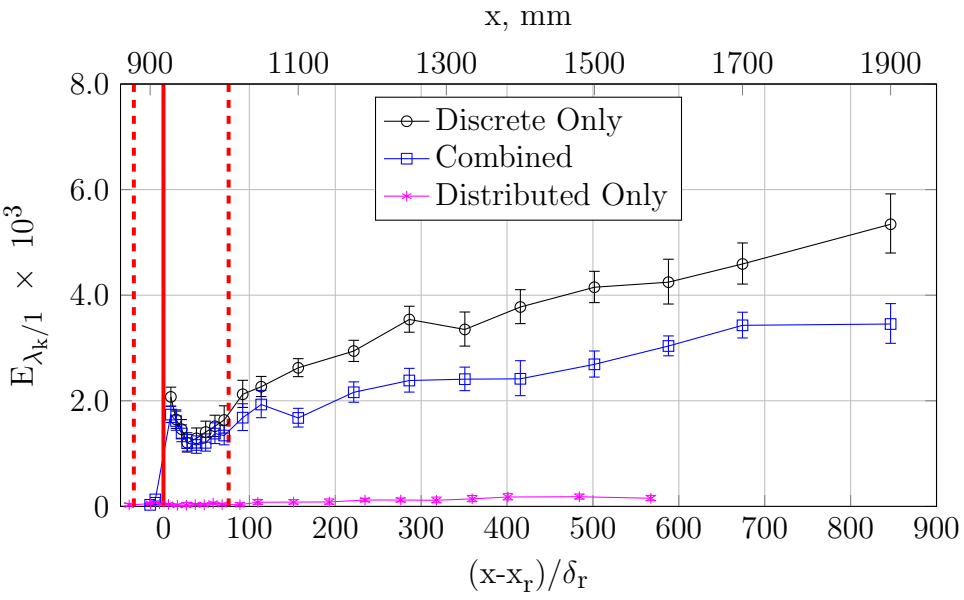

Figure 7.3: Comparison of the disturbance energy of the m = 1 mode for the three roughness configurations at the lower Reynolds number condition

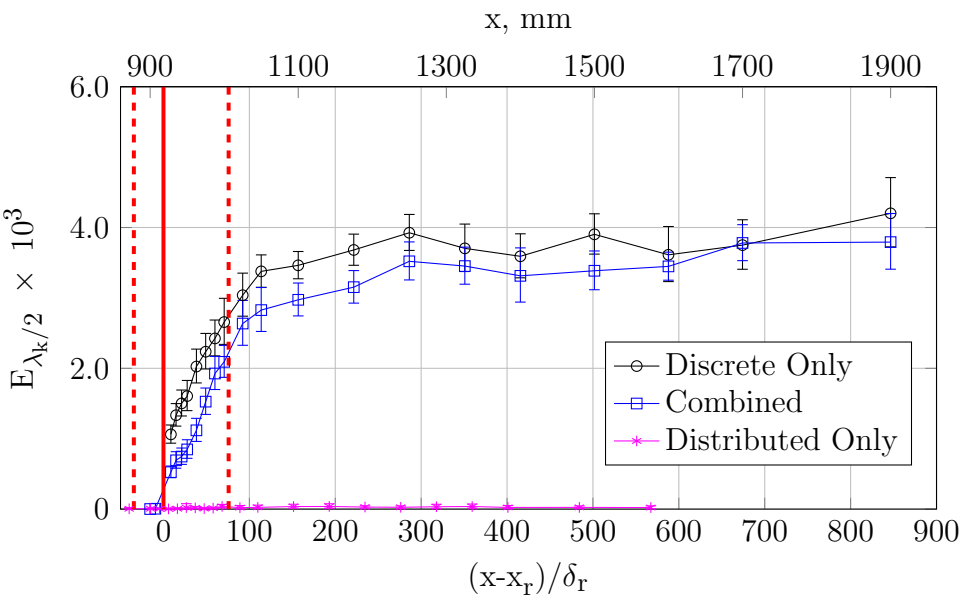

Figure 7.4: Comparison of the disturbance energy of the m = 2 mode for the three roughness configurations at the lower Reynolds number condition

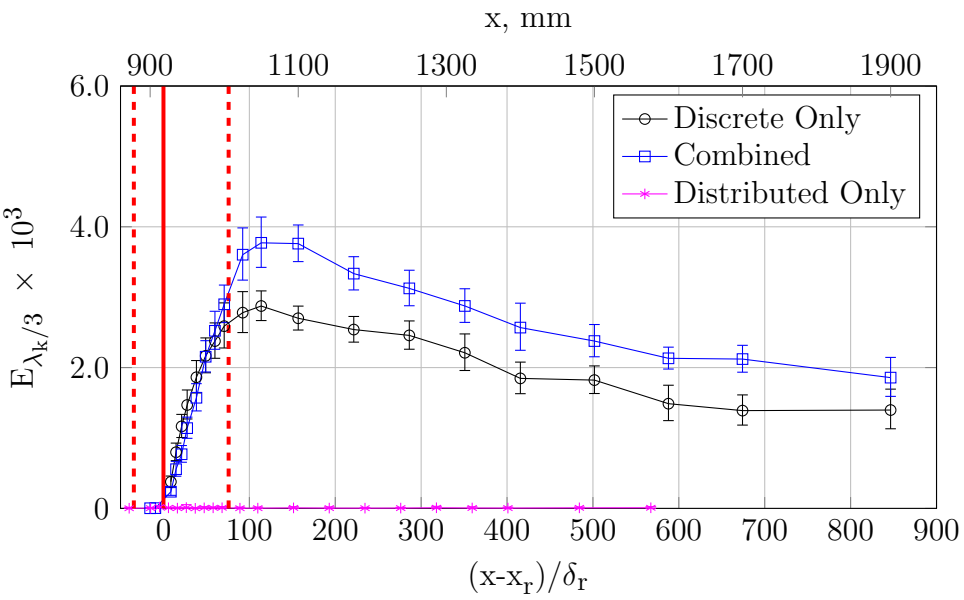

Figure 7.5: Comparison of the disturbance energy of the m = 3 mode for the three roughness configurations at the lower Reynolds number condition

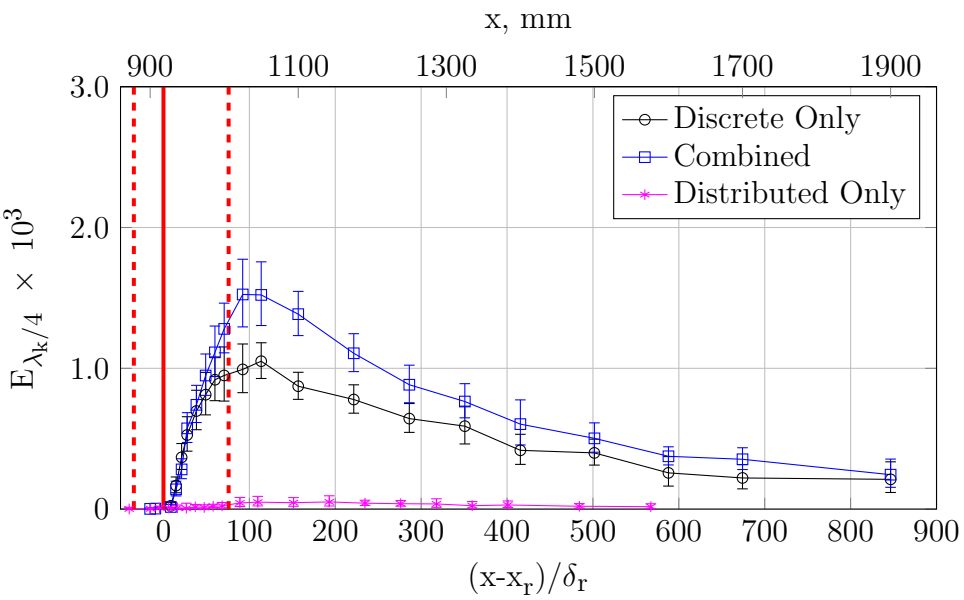

Figure 7.6: Comparison of the disturbance energy of the m = 4 mode for the three roughness configurations at the lower Reynolds number condition

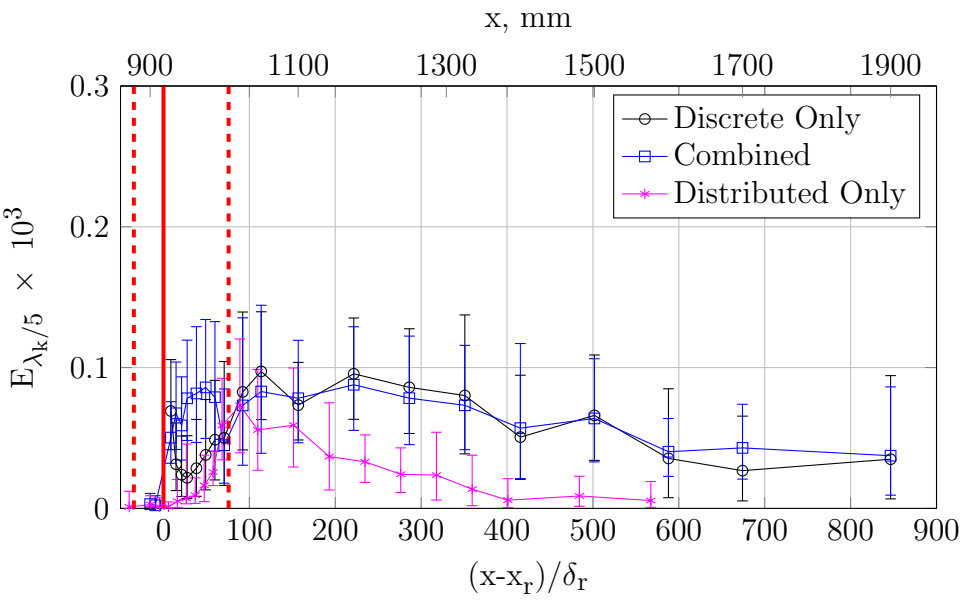

Figure 7.7: Comparison of the disturbance energy of the m = 5 mode for the three roughness configurations at the lower Reynolds number condition

Figure 7.2 compares the growth of the spanwise invariant mode. The minimum point on each curve is the location where the U'_{mean} profile switches from deficit-dominated to high-speed streak dominated. The minimum energy point is further downstream for the combined roughness case; the presence of the distributed roughness slows down the rate which high momentum fluid is pulled towards the wall. In the far wake, both configurations show m = 0 energy growth at the same spatial rate.

The m = 1 mode (shown in Fig. 7.3) is also suppressed with the addition of the distributed roughness. In the near-wake, the two roughness configurations have nearly equal energy. In the mid-wake, the growth rates of the two modes diverge; the discrete roughness only case continues to grow at a faster rate, while the combined roughness case grows at a slower rate. The difference in growth rates persists into the far-wake. The m = 2 mode, shown in Fig. 7.4, is also suppressed by the distributed roughness; adding the distributed roughness reduced the strength of this mode throughout the wake.

The comparisons for the m = 3 and m = 4 modes are shown in Figs. 7.5 and 7.6. Both modes show the same trends; in the near-wake, the two roughness configurations have nearly identical amplitudes, but the combined roughness has a larger amplitude disturbance in the mid- and far-wake. The presence of the distributed roughness does not change the rate at which the disturbances decay in the far-wake.

The initial inclination from examining Figs. 7.2 through 7.6 is to assume that the distributed roughness redistributes energy from longer wavelength modes to shorter wavelength modes; however, Fig. 7.7 shows that the m = 5 mode is only larger for the combined roughness case in the near-wake. Downstream of the distributed roughness, the two configurations contain the same amount of energy in the m = 5 mode.

One possible explanation for the redistribution of energy to the m = 3 and m = 4 modes is the inherit wavelength distribution of the distributed roughness field. Table 3.4 shows the ten largest amplitude distributed roughness modes. Of the ten modes, five of them have spanwise wavelengths with m = -4, -3, 3, or 4. As streamwise vorticity pulls high-momentum fluid towards the bottom of the boundary layer, the entrained high-momentum fluid has to travel around the peaks in the distributed roughness, thus causing an increase in the disturbance energy at the largest amplitude distributed roughness modes.

7.1.2 Higher Reynolds Number

At the higher Reynolds number, both the combined roughness and discrete roughness configurations tripped the boundary layer. Figure 7.8 compares the total disturbance energy for the different roughness configurations, while Figs. 7.9 through 7.13 compare the energy in the different spanwise modes. In all of these plots, the red vertical lines indicate the location of the discrete and distributed roughness, while the black and blue vertical lines show the location of the turbulent wedge origin for each roughness configuration.

Figure 7.8 shows the total disturbance energy for the different roughness configurations. The turbulent wedge forms ∼80 mm downstream of the distributed roughness, so the streamwise domain for the energy to grow is limited. When the distributed roughness was added, the total disturbance energy decreased slightly throughout most of the wake; however, the difference is small and by itself does not describe the difference in transition between the two cases.

The comparison of the m = 0 mode, which is shown in Fig. 7.9, shows that the distributed roughness slows down the rate in which the high-speed streak penetrates the bottom of the boundary layer. The m = 0 energy is higher in the near-wake for the

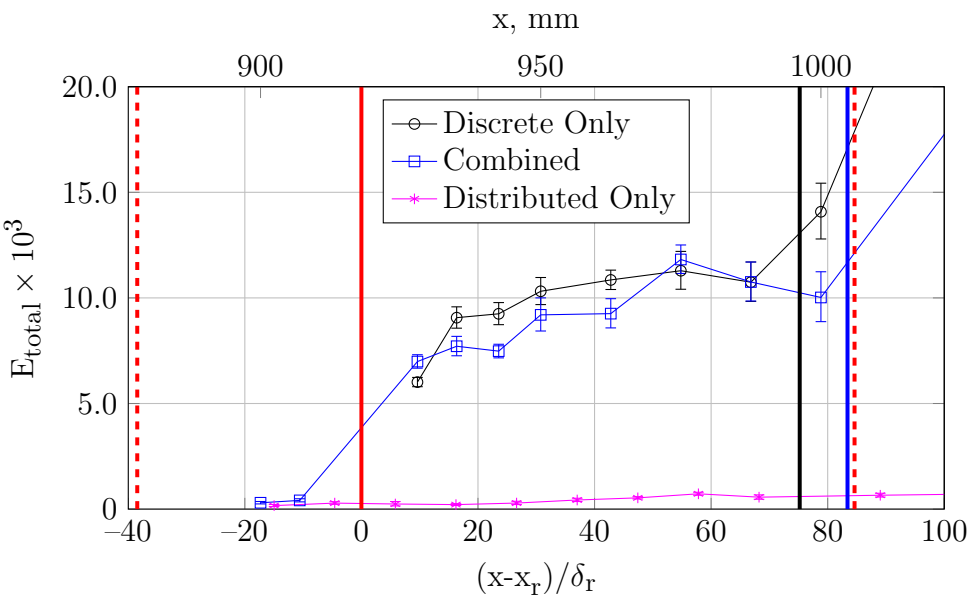

Figure 7.8: Comparison of total disturbance energy for the three roughness configurations at the higher Reynolds number configuration

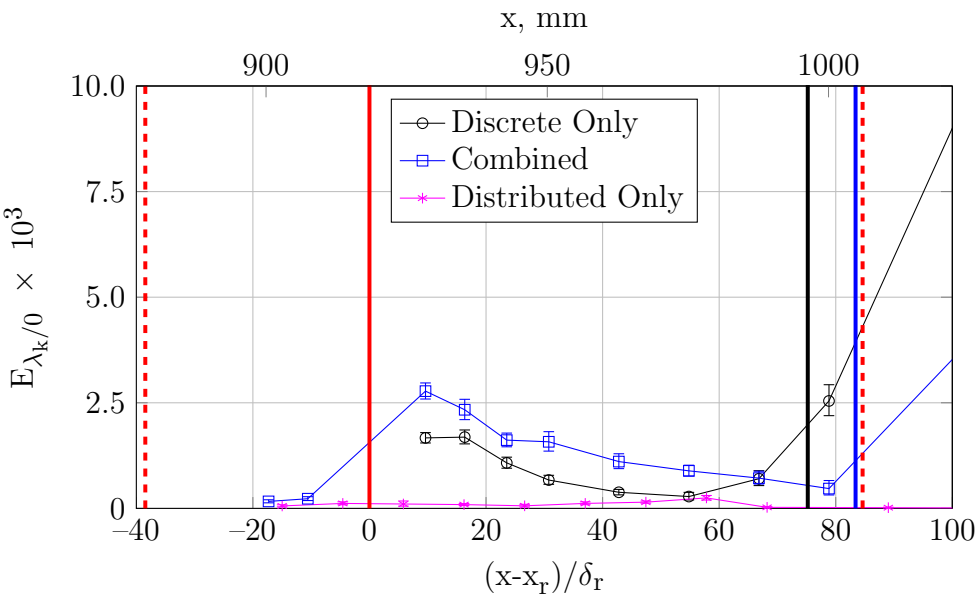

Figure 7.9: Comparison of the disturbance energy of the m = 0 mode for the three roughness configurations at the higher Reynolds number configuration

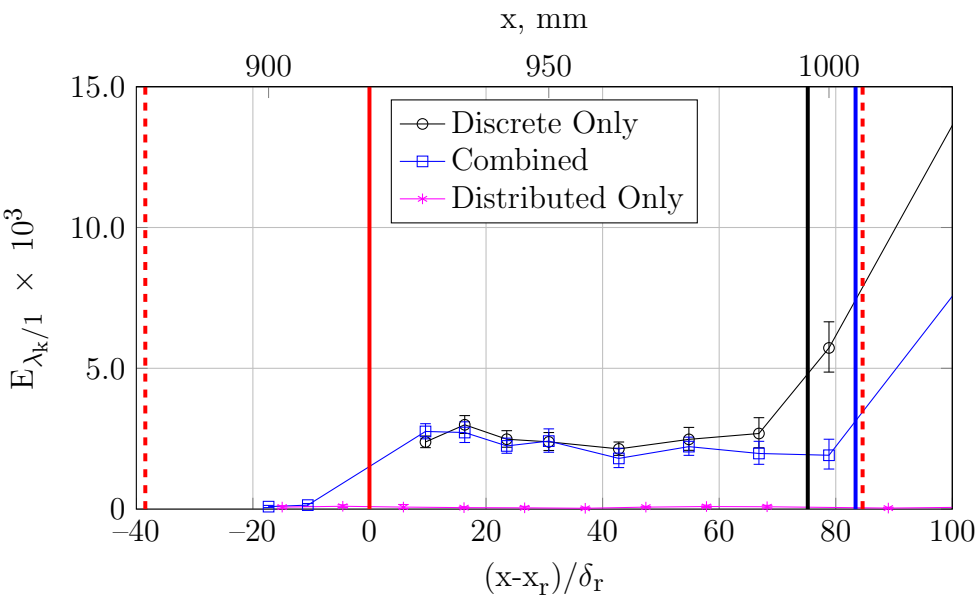

Figure 7.10: Comparison of the disturbance energy of the m = 1 mode for the three roughness configurations at the higher Reynolds number configuration

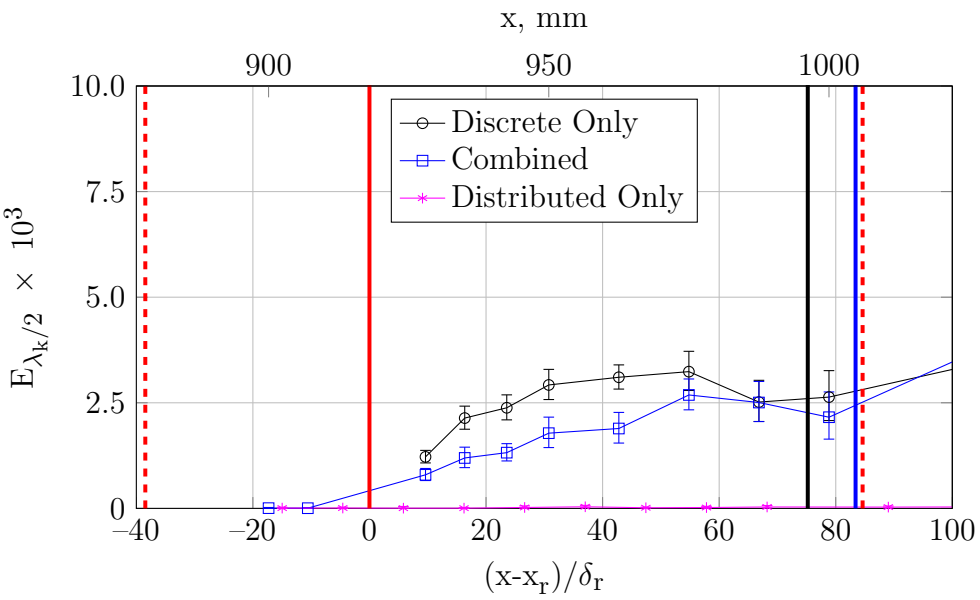

Figure 7.11: Comparison of the disturbance energy of the m = 2 mode for the three roughness configurations at the higher Reynolds number configuration

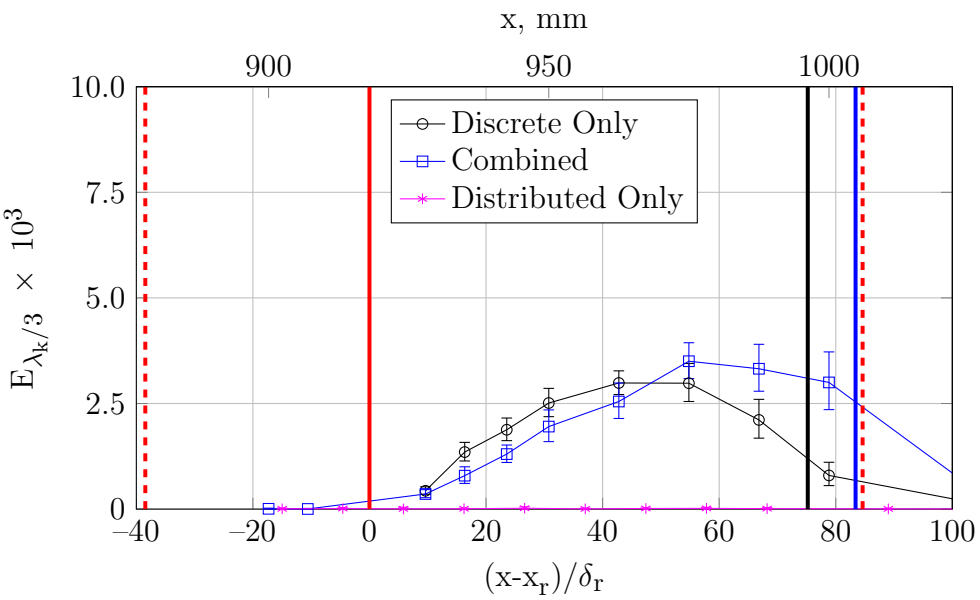

Figure 7.12: Comparison of the disturbance energy of the m = 3 mode for the three roughness configurations at the higher Reynolds number configuration

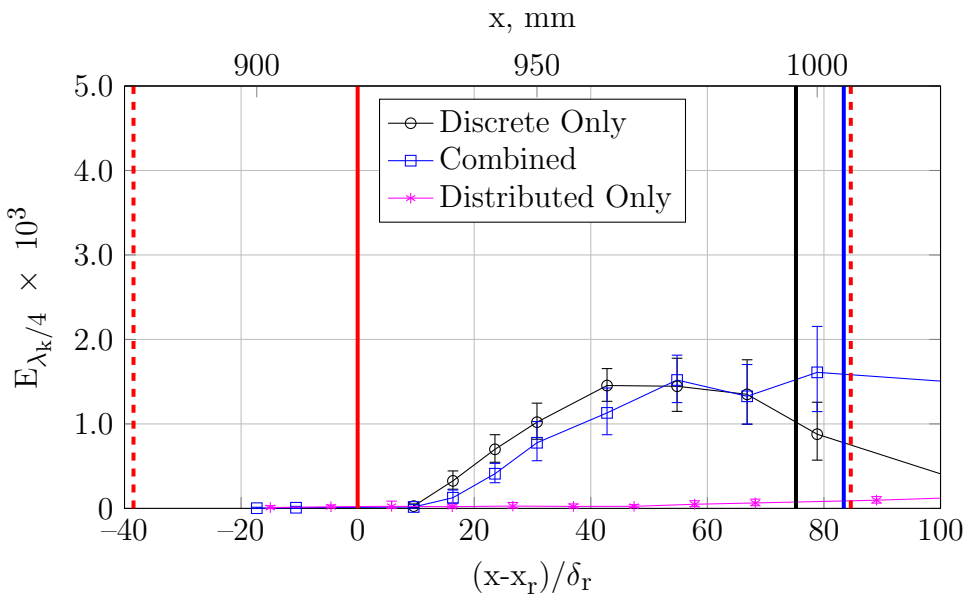

Figure 7.13: Comparison of the disturbance energy of the m = 4 mode for the three roughness configurations at the higher Reynolds number configuration

combined roughness case but continually decreases over the distributed roughness. At x $\sim$ 980 mm, the energy for the discrete roughness case reaches a minimum and begins to increase. A few millimeters downstream, the energy for the combined roughness case reaches a minimum and begins to increase. In both cases, transition begins shortly downstream of this energy minimum; this indicates that the transition location is related to the rate which the vortices bring high-momentum fluid to the bottom of the boundary layer.

The m = 1 modes (Fig. 7.10) for the two roughness configurations are the same until the turbulent wedge forms, at which point the energy begins to increase. The m = 2 mode (Fig. 7.11) is smaller for the combined roughness case and decreases just upstream of the transition point for both configurations.

The m = 3 and m = 4 modes (Figs. 7.12 and 7.13) show a slightly different behavior at the higher Reynolds number compared to the lower Reynolds number. Just downstream of the roughness element, the discrete roughness configuration has more energy in these spanwise modes than the combined roughness configuration. At x = 975 mm, the energy for the discrete roughness configuration begins to decay and becomes smaller than the energy for the combined roughness configuration. The transfer of energy from the longer spanwise wavelengths to the m = 3 and m = 4 modes is just beginning as the turbulent wedge forms.

7.2 Unsteady Disturbance Energy

At the higher Reynolds number condition, both roughness configurations trip the boundary layer. Upstream of the formation of the turbulent wedge, secondary instabilities grow along the low-speed streak centered near z = -3 mm. Comparisons of the contour plots in Sections 5 & 6 showed the combined roughness case had lower levels of unsteadiness. The differences in the unsteady disturbances between the two

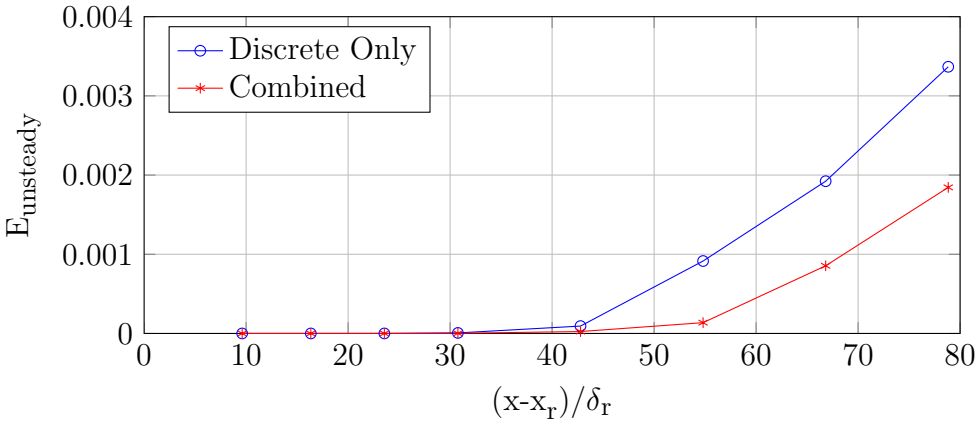

Figure 7.14: Comparison of unsteady disturbance energy for the discrete roughness and combined roughness configurations for the higher Reynolds number condition.

roughness configurations are further investigated to better understand how rapidly the secondary instabilities grow.

Figure 7.14 shows the integrated unsteady disturbance on a linear axis to highlight the transition delay achieved with the combined roughness configuration. The unsteady energy for the combined roughness case is shifted downstream 16.5 mm relative to the discrete roughness case. This difference is larger than the 9 mm delay seen from comparing flow visualization images.

Figure 7.15 compares the unsteady energy on a log axis to better understand the growth rate of the secondary instabilities. For both configurations, the disturbance grows slowly in the near-wake and sharply in the mid-wake. The growth rate then decreases as the unsteadiness saturates while the turbulent wedge begins to form.

The exponential growth rate of the disturbances was evaluated by curve fitting the points between 30 mm and 65 mm downstream of the discrete roughness, where the disturbance growth is largest and the growth rate appears linear. The growth rates are shown with dashed lines in Fig. 7.15 and are listed in Table 7.1. When the distributed roughness is added, the growth rate decreases by 24%. Even with

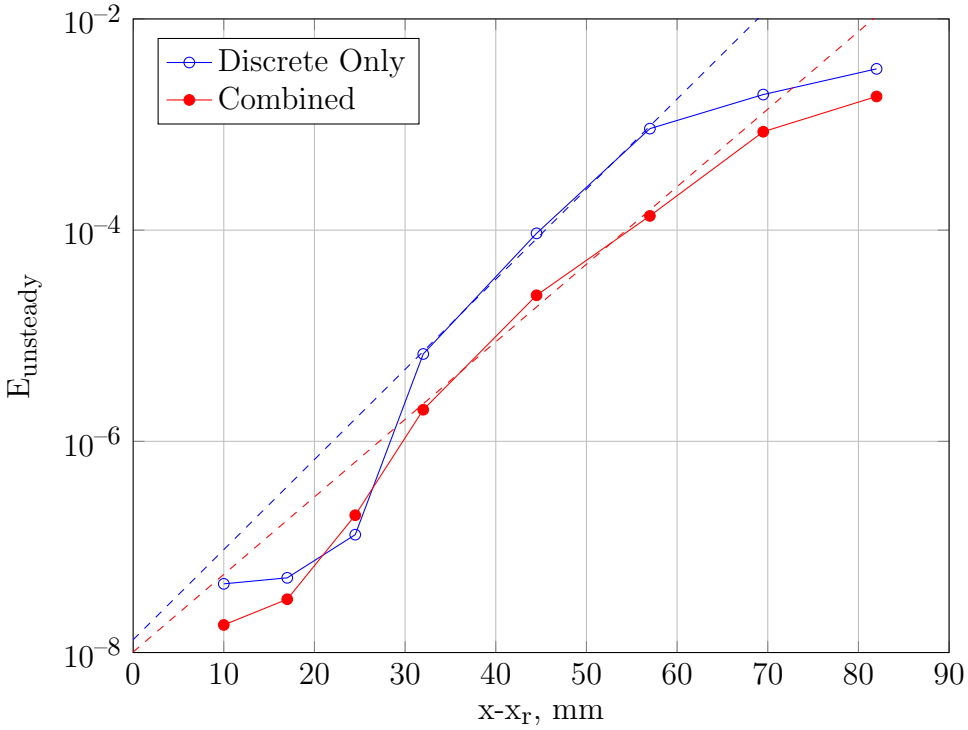

Figure 7.15: Comparison of unsteady disturbance energy for the discrete roughness and combined roughness configurations for the higher Reynolds number condition on a log axis. The exponential growth rate is shown using the dashed lines.

Table 7.1: Exponential growth rates of unsteady disturbances

Configuration	Exponential Growth Rate, 1/mm	Distance to Grow Order of Magnitude, mm
Discrete	0.1965	11.72
Combined	0.1691	13.62

the reduction in growth rate, the unsteady disturbances still grow exponentially and lead to transition. The growth rate would have to be reduced even further in order to prevent transition and create a sub-critical roughness wake.

8. CONCLUSIONS AND FUTURE WORK

This dissertation investigates the disturbances created by distributed roughness patches and discrete roughness elements in a flat plate boundary layer. The goal of this work is to better understand how different types of roughness initiate transient growth and, in some cases, lead to transition. In particular, the experiment was designed to study the shielding effect observed by Drews [30].

Different roughness configurations were manufactured using rapid-prototyping and mounted flush with the wall in a flat plate boundary layer. The three roughness configurations tested were a 32 mm wide $\times$ 128 mm long patch of distributed roughness, a discrete roughness element (a 10 mm $\times$ 5 mm, 45° slanted rectangle with 1 mm $\times$ 1 mm edges), and the combination of the two. Naphthalene flow visualization and hotwire anemometry were used to characterize the flow above and downstream of the different types of roughness at roughness Reynolds numbers ($\mathrm{Re_k}$) between 113 and 230.

By itself, the distributed roughness patch created a small amplitude, sub-critical roughness wake. The steady disturbance profiles and the integrated energy show that distributed roughness excites transient growth over a broad range of spanwise wavelengths. Comparisons of results from different freestream speeds and roughness amplitudes show that the total disturbance energy scales according to $\mathrm{Re_k^2}$, which is consistent with the results of White et al. [14] and Downs et al. [28].

The discrete roughness element also initiated disturbances that underwent transient growth. At the lower Reynolds number condition ($\mathrm{Re_k} = 151$), the obliquely oriented rectangle creates a sub-critical roughness wake. At the higher Reynolds number ($\mathrm{Re_k} = 220$), a turbulent wedge formed $\sim$15 boundary layer thicknesses downstream

of the roughness. This $\mathrm{Re_k}$ value is close to the predicted critical Reynolds number ($\mathrm{Re_{k_{critical}}} = 239$) using the correlation suggested by Tani [39].

Adding the distributed roughness around the discrete roughness modified the structure of the wake at both Reynolds numbers. At the lower Reynolds number, the total disturbance energy was slightly decreased in the far-wake. Energy was transferred from the longer spanwise wavelength modes to the shorter wavelength modes; this occurs because high-speed fluid that is brought down to the bottom of the boundary layer by streamwise vorticity must conform to the topographical modes in the distributed roughness. At the higher Reynolds number, flow visualization, steady disturbance profiles, and unsteady disturbance energy all showed that transition was delayed 7-16 mm by adding the distributed roughness. The presence of the distributed roughness changes the rate in which high-momentum fluid is brought to the bottom of the boundary layer, which appears to be linked to the transition location. The altered basic state in the combined roughness case slightly lowered the exponential growth rate of the secondary instabilities that lead to transition.

This research presents several opportunities for fruitful work moving forward. One of these possibilities includes studying a longer and wider distributed roughness patch. This experiment was the first attempt to measure transient growth created by streamwise-elongated distributed roughness. Even with a patch 128 mm long, shorter spanwise wavelength disturbances were only beginning to grow at the downstream end of the patch. Further elongating the roughness patch in the streamwise direction would provide the opportunity to better understand receptivity of roughness at multiple streamwise locations.

Secondly, the hotwire results collected in this experiment can be used as an input to secondary instability calculations to better understand the mechanism that delays transition. This work is already underway at Texas A&M by Jason Monschke; pre-

liminary results have shown that the wake of the discrete roughness at the $\mathrm{Re}_{\mathrm{k}} = 220$ condition is susceptible to secondary instabilities with strong temporal growth rates, and these instabilities are what lead to transition. The mode shapes of instabilities at specific frequencies can be compared between the secondary instability calculations and narrowband temporal spectra from the experiment. These analysis tools can be used to compare the discrete only and combined roughness wakes to better understand what features of the wake affect the mode shapes and growth rates of secondary instabilities that lead to transition.

Finally, the experiment should be extended to a new combination of distributed and discrete roughness. In this new configuration, the relative height of the distributed roughness should be increased. Because the distributed roughness by itself created such small disturbances, the distributed roughness height can be increased to further shield the discrete roughness. This may lead to a more significant transition delay or, ideally, prevent transition.

REFERENCES

[1] Joslin, R. D., "Aircraft Laminar Flow Control," *Annual Review of Fluid Mechanics*, Vol. 30, No. 1, 1998, pp. 1–29.

[2] Reshotko, E., "Transient Growth: A Factor in Bypass Transition," *Physics of Fluids*, Vol. 13, No. 5, 2001, pp. 1067–1075.

[3] Morkovin, M. V., Reshotko, E., and Herbert, T., "Transition in Open Flow Systems - A Reassessment," *Bulletin of the APS*, Vol. 39, No. 9, 1994.

[4] Ellingsen, T. and Palm, E., "Stability of Linear Flow," *Physics of Fluids*, Vol. 18, No. 4, 1975, pp. 487–488.

[5] Landahl, M. T., "A Note on an Algebraic Instability of Inviscid Parallel Shear Flows," *J. Fluid Mech.*, Vol. 98, 1980, pp. 243–251.

[6] Ergin, F. and White, E., "Unsteady and Transitional Flows Behind Roughness Elements," *AIAA Journal*, Vol. 44, 2006, pp. 2504–2514.

[7] Andersson, P., Brandt, L., Bottaro, A., and Henningson, D. S., "On the Breakdown of Boundary Layer Streaks," *Journal of Fluid Mechanics*, Vol. 428, 2001, pp. 29–60.

[8] Andersson, P., Berggren, M., and Henningson, D. S., "Optimal Disturbances and Bypass Transition in Boundary Layers," *Physics of Fluids*, Vol. 11, 1999, pp. 134.

[9] Luchini, P., "Reynolds-Number Independent Instability of the Boundary Layer over a Flat Surface: Optimal Perturbations," *Journal of Fluid Mechanics*, Vol. 404, 2000, pp. 289–309.

[10] Tumin, A. and Reshotko, E., "Spatial Theory of Optimal Disturbances in Boundary Layers," *Physics of Fluids*, Vol. 13, No. 7, 2001, pp. 2097–2104.

[11] White, E. B., "Transient Growth of Stationary Disturbances in a Flat Plate Boundary Layer," *Physics of Fluids*, Vol. 14, No. 12, 2002, pp. 4429–4439.

[12] White, E. and Ergin, F., "Receptivity and Transient Growth of Roughness-Induced Disturbances," AIAA Paper 2003-4243.

[13] Ergin, F. and White, E., "Multicomponent and Unsteady Velocity Measurements of Transient Disturbances," AIAA Paper 2005-0527.

[14] White, E. B., Rice, J. M., and Ergin, F. G., "Receptivity of Stationary Transient Disturbances to Surface Roughness," *Physics of Fluids*, Vol. 17, No. 6, 2005, pp. 064109.

[15] Denissen, N. A. and White, E. B., "Roughness-Induced Bypass Transition, Revisited," *AIAA Journal*, Vol. 46, No. 7, 2008, pp. 1874–1877.

[16] Denissen, N. A., Downs III, R. S., and White, E. B., "Transient Growth due to Surface Roughness: Theory, Simulation and Experiment," AIAA Paper 2009-0175.

[17] Fischer, P. and Choudhari, M., "Numerical Simulation of Roughness-Induced Transient Growth in a Laminar Boundary Layer," AIAA Paper 2004-2539.

[18] Choudhari, M. and Fischer, P., "Roughness-Induced Transient Growth," AIAA Paper 2005-4765.

[19] Rizzetta, D. P. and Visbal, M. R., "Direct Numerical Simulations of Flow Past an Array of Distributed Roughness Elements," *AIAA Journal*, Vol. 45, No. 8, 2007, pp. 1967–1976.

[20] Stephani, K. A. and Goldstein, D. B., "DNS Study of Transient Disturbance Growth and Bypass Transition Due to Realistic Roughness," AIAA Paper 2009-0585.

[21] Doolittle, C. J., *Near-Field Flow Structures and Transient Growth Due to Subcritical Surface Roughness*, Master's thesis, University of Texas at Austin, Ausstin, TX, 2010.

[22] Tumin, A. and Reshotko, E., "Receptivity of a Boundary-Layer Flow to a Three-Dimensional Hump at Finite Reynolds Numbers," *Physics of Fluids*, Vol. 17, No. 9, 2005, pp. 094101.

[23] Denissen, N. A. and White, E. B., "Continuous Spectrum Analysis of Roughness-Induced Transient Growth," *Phys. Fluids*, Vol. 21, No. 114105, 2009.

[24] Reshotko, E. and Leventhal, L., "Preliminary Experimental Study of Disturbances in a Laminar Boundary-Layer due to Distributed Roughness," AIAA Paper 1981-1224.

[25] Kendall, J., "Laminar Boundary Layer Velocity Distortion by Surface Roughness: Effect Upon Stability," AIAA Paper 1981-0195.

[26] Corke, T. C., Bar-Sever, A., and Morkovin, M. V., "Experiments on Transition Enhancement by Distributed Roughness," *Physics of Fluids*, Vol. 29, No. 10, 1986, pp. 3199–3213.

[27] White, E. B. and Reshotko, E., "Rougness-Induced Transient Growth in a Flat-Plate Boundary Layer," AIAA Paper 2002-0138.

[28] Downs, R. S., White, E. B., and Denissen, N. A., "Transient Growth and Transition Induced by Random Distributed Roughness," *AIAA Journal*, Vol. 46, No. 2, 2008, pp. 451–462.

[29] Drews, S. D., Downs III, R. S., Doolittle, C. J., Goldstein, D. B., and White, E. B., "Direct Numerical Simulations of Flow Past Random Distributed Roughness," AIAA Paper 2011-0564.

[30] Drews, S. D., *Direct Numerical Simulation of Flow Past Quasi-Random Distributed Roughness*, Master's thesis, University of Texas at Austin, Austin, TX.

[31] Saric, W. S., "The ASU Transition Research Facility," AIAA Paper 1992-3910.

[32] Hunt, L. E., Downs III, R. S., Kuester, M. S., White, E. B., and Saric, W. S., "Flow Quality Measurements in the Klebanoff–Saric Wind Tunnel," AIAA Paper 2010-4538.

[33] Kuester, M. S. and White, E. B., "Acoustic Forcing and Control of Reflected Waves in the Klebanoff–Saric Wind Tunnel," AIAA Paper 2012-2862.

[34] White, E. B., *Breakdown of Crossflow Vortices*, Ph.D. thesis, Arizona State University, Tempe, AZ, August 2000.

[35] White, E. and Ergin, F., "Using laminar-flow velocity profiles to locate the wall behind roughness elements," *Experiments in Fluids*, Vol. 36, 2004, pp. 805–812.

[36] Reshotko, E. and Tumin, A., "Role of Transient Growth in Roughness-Induced Transition," *AIAA Journal*, Vol. 42, No. 4, 2004, pp. 766–770.

[37] Downs III, R. S., *Environmental Influences on Crossflow Instability*, Ph.D. thesis, Texas A&M University, College Station, TX, June 2012.

[38] Press, W. H., Teukolsky, S. A., Vetterling, W. T., and Flannery, B. P., *Numerical Recipes: The Art of Scientific Computing*, Cambridge University Press, New York, NY, USA, 3rd ed., 2007.

[39] Tani, I., "Boundary-Layer Transition," *Annual Review of Fluid Mechanics*, Vol. 1, No. 1, 1969, pp. 169–196.

APPENDIX A

RUN LOGS

Tables A.1, A.2, and A.3 show the run logs for each phase of the roughness experiments. These tables are included so the data files from these runs can be easily located for reference purposes.

Table A.1: Combined Roughness Run Log

Case #	Tunnel Set Unit Reynolds Number (1/m)	Streamwise Location (mm)	IIYS (mm)	Velocity Cutoff (%)	Small Step Size (mm)	Small Step Size Cutoff (%)	Rougness Flats Location (mm)	Roughness Flats Cutoff (%)	Roughness Flats Width (mm)	Date	Tunnel Operator	Run Time (w/calibration)	Re_k
1	610000	900	0.4208	18	0.010	22	16	10	4	1/14/2014	Kuester	4:22	
2	610000	907	0.4227	18	0.010	22	16	10	4	1/23/2014	Kuester	4:28	
3	610000	928	0.4285	18	0.010	22	16	10	4	1/15/2014	Kuester	4:24	
4	610000	935	0.4304	18	0.010	22	16	10	4	1/15/2014	Kuester	4:26	
5	610000	942.5	0.4324	18	0.010	22	16	10	4	1/24/2014	Kuester	4:24	
6	610000	950	0.4344	18	0.010	22	16	10	4	1/24/2014	Kuester	4:21	
7	610000	962.5	0.4377	20	0.010	22	16	10	4	1/27/2014	Kuester	4:25	
8	610000	975	0.4411	20	0.010	22	16	10	4	1/28/2014	Kuester	3:53	
9	610000	987.5	0.4443	20	0.010	22	16	10	4	1/29/2014	Kuester	4:13	
10	610000	1000	0.4476	20	0.010	22	16	10	4	1/29/2014	Kuester	4:10	
11	610000	1025	0.4541	10	N/A	N/A	N/A	N/A	N/A	1/15/2014	Kuester	4:52	151 / 112
12	610000	1050	0.4604	10	N/A	N/A	N/A	N/A	N/A	1/16/2014	Kuester	5:06	
13	610000	1100	0.4729	10	N/A	N/A	N/A	N/A	N/A	1/16/2014	Kuester	4:42	
14	610000	1175	0.4910	10	N/A	N/A	N/A	N/A	N/A	1/25/2014	Kuester	4:50	
15	610000	1250	0.5085	10	N/A	N/A	N/A	N/A	N/A	1/27/2014	Kuester	4:44	
16	610000	1325	0.5254	10	N/A	N/A	N/A	N/A	N/A	1/27/2014	Kuester	4:42	
17	610000	1400	0.5418	10	N/A	N/A	N/A	N/A	N/A	1/28/2014	Kuester	4:48	
18	610000	1500	0.5629	10	N/A	N/A	N/A	N/A	N/A	1/30/2014	Kuester	4:46	
19	610000	1600	0.5832	10	N/A	N/A	N/A	N/A	N/A	1/30/2014	Kuester	4:55	
20	610000	1700	0.6029	10	N/A	N/A	N/A	N/A	N/A	1/31/2014	Kuester	4:50	
21	610000	1900	0.6403	10	N/A	N/A	N/A	N/A	N/A	1/31/2014	Kuester	4:46	
22	799326	900	0.3649	21	0.010	25	16	10	4	1/22/2014	Kuester	4:07	
23	799326	907	0.3666	21	0.010	25	16	10	4	1/23/2014	Kuester	4:06	
24	799326	928	0.3716	21	0.010	25	16	10	4	1/17/2014	Kuester	4:19	
25	799326	935	0.3733	21	0.010	25	16	10	4	1/18/2014	Kuester	4:14	
26	799326	942.5	0.3751	21	0.010	25	16	10	4	1/22/2014	Kuester	4:47	
27	799326	950	0.3769	21	0.010	25	16	10	4	1/17/2014	Kuester	4:14	
28	799326	962.5	0.3798	26	0.010	30	16	10	4	1/22/2014	Kuester	4:03	228 / 169
29	799326	975	0.3827	26	0.010	30	16	15	4	1/24/2014	Kuester	5:30	
30	799326	987.5	0.3856	26	0.010	30	16	15	4	1/29/2014	Kuester	4:54	
31	799326	1000	0.3885	28	0.010	30	16	15	4	1/18/2014	Kuester	4:57	
32	799326	1025	0.3942	28	0.010	30	14	16	4	1/19/2014	Kuester	4:46	
33	799326	1050	0.3998	28	0.010	31	14	17	4	1/20/2014	Kuester	5:09	
34	799326	1100	0.4107	29	0.010	32	14	18	3	1/21/2014	Kuester	5:10	
35	610000	865	0.4000	10	0.010	N/A	N/A	N/A	N/A	1/14/2014	Kuester	4:52	N/A
36	799326	865	0.3563	10	0.010	N/A	N/A	N/A	N/A	1/17/2014	Kuester	4:42	

Table A.2: Discrete Roughness Only Run Log

Case #	Tunnel Set Unit Reynolds Number (1/m)	Streamwise Location (mm)	IIYS (mm)	Velocity Cutoff (%)	Small Step Size (mm)	Small Step Size Cutoff (%)	Rougness Flats Location (mm)	Roughness Flats Cutoff (%)	Roughness Flats Width (mm)	Date	Tunnel Operator	Re_k
1	610000	928	0.4285	10	N/A	N/A	N/A	N/A	N/A	12/9/2013	Kuester	
2	610000	935	0.4277	10	0.010	13	N/A	N/A	N/A	12/3/2013	Kuester	
3	610000	942.5	0.4324	10	N/A	N/A	N/A	N/A	N/A	12/5/2013	Kuester	
4	610000	950	0.4344	10	0.010	13	N/A	N/A	N/A	11/27/2013	Kuester	
5	610000	962.5	0.4377	10	N/A	N/A	N/A	N/A	N/A	12/5/2013	Kuester	
6	610000	975	0.4411	10	N/A	N/A	N/A	N/A	N/A	12/6/2013	Kuester	
7	610000	987.5	0.4443	10	N/A	N/A	N/A	N/A	N/A	12/6/2013	Kuester	
8	610000	1000	0.4476	10	0.010	13	N/A	N/A	N/A	11/21/2013	Kuester	
9	610000	1025	0.4541	10	N/A	N/A	N/A	N/A	N/A	12/9/2013	Kuester	
10	610000	1050	0.4604	10	N/A	N/A	N/A	N/A	N/A	12/10/2013	Kuester	151
11	610000	1100	0.4729	10	0.010	13	N/A	N/A	N/A	11/22/2013	Kuester	
12	610000	1175	0.4910	10	N/A	N/A	N/A	N/A	N/A	12/10/2013	Kuester	
13	610000	1250	0.5085	10	N/A	N/A	N/A	N/A	N/A	12/4/2013	Kuester	
14	610000	1325	0.5254	10	N/A	N/A	N/A	N/A	N/A	12/11/2013	Kuester	
15	610000	1400	0.5418	10	0.010	13	N/A	N/A	N/A	12/2/2013	Kuester	
16	610000	1500	0.5629	10	N/A	N/A	N/A	N/A	N/A	12/11/2013	Kuester	
17	610000	1600	0.5832	10	0.010	13	N/A	N/A	N/A	12/2/2013	Kuester	
18	610000	1700	0.6029	10	N/A	N/A	N/A	N/A	N/A	12/3/2013	Kuester	
19	610000	1900	0.6403	10	N/A	N/A	N/A	N/A	N/A	12/12/2913	Kuester	
20	799326	928	0.3716	10	N/A	N/A	N/A	N/A	N/A	12/12/2913	Kuester	
21	799326	935	0.3733	10	N/A	N/A	N/A	N/A	N/A	12/13/2013	Kuester	
22	799326	942.5	0.3751	10	N/A	N/A	N/A	N/A	N/A	12/13/2013	Kuester	
23	799326	950	0.3769	10	N/A	N/A	N/A	N/A	N/A	12/16/2013	Kuester	
24	799326	962.5	0.3798	26	0.010	30	14	15	4	1/3/2014	Kuester	
25	799326	975	0.3827	25	0.010	28	14	14	4	12/19/2013	Kuester	228
26	799326	987.5	0.3856	25	0.010	28	14	15	4	1/6/2014	Kuester	
27	799326	1000	0.3769	20	0.010	23	16	15	8	12/17/2013	Kuester	
28	799326	1025	0.3942	25	0.010	30	14	15	4	1/6/2014	Kuester	
29	799326	1050	0.3998	27	0.010	30	14	15	4	1/7/2014	Kuester	
30	799326	1100	0.4107	28	0.010	32	14	18	3	1/8/2014	Wilcox/Long	
31	610000	1250	0.5085	10	N/A	N/A	N/A	N/A	N/A	1/9/2014	Kuester	151

Table A.3: Distributed Roughness Only Run Log

Case #	Tunnel Set Unit Reynolds Number (1/m)	Side of Roughness Insert	Streamwise Location (mm)	IIYS (mm)	Velocity Cutoff (%)	Small Step Size (mm)	Small Step Size Cutoff (%)	Date	Tunnel Operator	Re_k
1	610000	Positive	900	0.425	17	0.010	22	6/6/2013	Kuester	
2	610000	Positive	912.5	0.425	17	0.010	22	7/26/2013	Wilcox	
3	610000	Positive	925	0.425	17	0.010	22	6/6/2013	Kuester	
4	610000	Positive	937.5	0.440	17	0.010	22	7/18/2013	Kuester	
5	610000	Positive	950	0.444	17	0.010	22	7/19/2013	Kuester	
6	610000	Positive	962.5	0.459	17	0.010	25	6/5/2013	Kuester	
7	610000	Positive	975	0.465	19	0.010	23	6/10/2013	Kuester	
8	610000	Positive	987.5	0.460	17	0.010	25	7/26/2013	Kuester	
9	610000	Positive	1000	0.465	19	0.010	23	6/10/2013	Kuester	
10	610000	Positive	1025	0.465	10	N/A	N/A	6/10/2013	Kuester	
11	610000	Positive	1050	0.550	10	N/A	N/A	5/20/2013	Kuester	112
12	610000	Positive	1100	0.560	10	N/A	N/A	7/25/2013	Kuester	
13	610000	Positive	1150	0.560	10	N/A	N/A	5/21/2013	Kuester	
14	610000	Positive	1200	0.560	10	N/A	N/A	5/21/2013	Kuester	
15	610000	Positive	1250	0.550	10	N/A	N/A	5/22/2013	Kuester	
16	610000	Positive	1300	0.485	10	N/A	N/A	5/27/2013	Kuester	
17	610000	Positive	1350	0.520	10	N/A	N/A	5/29/2013	Kuester	
18	610000	Positive	1400	0.490	10	N/A	N/A	6/3/2013	Kuester	
19	610000	Positive	1500	0.520	10	N/A	N/A	5/28/2013	Kuester	
20	610000	Positive	1600	0.540	10	N/A	N/A	5/29/2013	Kuester	
21	610000	Negative	900	0.445	25	0.010	28	5/31/2013	Wilcox	
22	610000	Negative	925	0.450	25	0.010	28	5/31/2013	Wilcox	
23	610000	Negative	950	0.454	25	0.010	28	6/1/2013	Wilcox	
24	610000	Negative	975	0.459	25	0.010	28	6/1/2013	Wilcox	
25	610000	Negative	1000	0.463	25	0.010	28	6/3/2013	Kuester	
26	610000	Negative	1050	0.480	10	N/A	N/A	5/29/2013	Kuester	
27	610000	Negative	1100	0.481	10	N/A	N/A	5/30/2013	Kuester	
28	610000	Negative	1150	0.481	10	N/A	N/A	5/30/2013	Kuester	56
29	610000	Negative	1200	0.481	10	N/A	N/A	5/30/2013	Kuester	
30	610000	Negative	1250	0.508	10	N/A	N/A	5/30/2013	Wilcox	
31	610000	Negative	1300	0.517	10	N/A	N/A	5/30/2013	Wilcox	
32	610000	Negative	1350	0.463	10	N/A	N/A	6/3/2013	Kuester	
33	610000	Negative	1400	0.535	10	N/A	N/A	5/31/2013	Kuester	
34	610000	Negative	1500	0.532	10	N/A	N/A	5/31/2013	Kuester	
35	610000	Negative	1600	0.571	10	N/A	N/A	5/31/2013	Kuester	
36	799326	Positive	900	0.374	20	0.010	25	7/8/2013	Kuester	
37	799326	Positive	912.5	0.377	20	0.010	25	7/9/2013	Kuester	
38	799326	Positive	925	0.379	20	0.010	25	7/23/2013	Kuester	
39	799326	Positive	937.5	0.382	20	0.010	25	7/9/2013	Kuester	
40	799326	Positive	950	0.385	20	0.010	25	7/10/2013	Kuester	
41	799326	Positive	962.5	0.388	20	0.010	25	7/10/2013	Kuester	
42	799326	Positive	975	0.390	20	0.010	25	7/10/2013	Kuester	
43	799326	Positive	987.5	0.393	20	0.010	25	7/10/2013	Kuester	
44	799326	Positive	1000	0.396	20	0.010	25	7/19/2013	Kuester	
45	799326	Positive	1025	0.401	10	N/A	N/A	7/1/2013	Wilcox	
46	799326	Positive	1050	0.406	10	N/A	N/A	7/1/2013	Wilcox	182
47	799326	Positive	1100	0.417	10	N/A	N/A	7/19/2013	Kuester	
48	799326	Positive	1150	0.427	10	N/A	N/A	7/2/2013	Wilcox	
49	799326	Positive	1200	0.437	10	N/A	N/A	7/20/2013	Kuester	
50	799326	Positive	1250	0.446	10	N/A	N/A	7/3/2013	Wilcox	
51	799326	Positive	1300	0.456	10	N/A	N/A	7/3/2013	Wilcox	
52	799326	Positive	1350	0.465	10	N/A	N/A	7/4/2013	Wilcox	
53	799326	Positive	1400	0.474	10	N/A	N/A	7/4/2013	Wilcox	
54	799326	Positive	1500	0.491	10	N/A	N/A	7/5/2013	Wilcox	
55	799326	Positive	1600	0.508	10	N/A	N/A	7/5/2013	Wilcox	
56	968315	Positive	900	0.350	22	0.010	26	6/18/2013	Kuester	
57	968315	Positive	912.5	0.350	22	0.010	26	6/18/2013	Kuester	
58	968315	Positive	925	0.350	22	0.010	26	6/18/2013	Kuester	
59	968315	Positive	937.5	0.350	22	0.010	26	7/22/2013	Kuester	
60	968315	Positive	950	0.350	22	0.010	26	6/19/2013	Kuester	
61	968315	Positive	962.5	0.350	22	0.010	26	6/19/2013	Kuester	
62	968315	Positive	975	0.350	25	0.010	28	7/22/2013	Kuester	
63	968315	Positive	987.5	0.350	25	0.010	28	7/22/2013	Kuester	
64	968315	Positive	1000	0.350	25	0.010	30	6/20/2013	Kuester	
65	968315	Positive	1025	0.390	10	N/A	N/A	6/12/2013	Kuester	
66	968315	Positive	1050	0.390	10	N/A	N/A	6/12/2013	Kuester	226
67	968315	Positive	1100	0.410	10	N/A	N/A	6/13/2013	Kuester	
68	968315	Positive	1150	0.425	10	N/A	N/A	6/13/2013	Kuester	
69	968315	Positive	1200	0.445	10	N/A	N/A	6/13/2013	Kuester	
70	968315	Positive	1250	0.460	10	N/A	N/A	6/14/2013	Kuester	
71	968315	Positive	1300	0.475	10	N/A	N/A	6/14/2013	Kuester	
72	968315	Positive	1350	0.485	10	N/A	N/A	6/14/2013	Kuester	
73	968315	Positive	1400	0.490	10	N/A	N/A	6/17/2013	Kuester	
74	968315	Positive	1500	0.490	10	N/A	N/A	6/17/2013	Kuester	
75	968315	Positive	1600	0.510	10	N/A	N/A	6/17/2013	Kuester	
76	968315	Negative	900	0.338	16	0.010	21	7/24/2013	Kuester	
77	968315	Negative	912.5	0.341	16	0.010	21	7/24/2013	Kuester	
78	968315	Negative	925	0.343	16	0.010	21	7/24/2013	Kuester	
79	968315	Negative	937.5	0.346	16	0.010	21	7/25/2013	Kuester	
80	968315	Negative	950	0.349	16	0.010	21	7/16/2013	Kuester	
81	968315	Negative	962.5	0.351	16	0.010	21	7/17/2013	Kuester	
82	968315	Negative	975	0.354	16	0.010	21	7/17/2013	Kuester	
83	968315	Negative	987.5	0.357	16	0.010	21	7/17/2013	Kuester	
84	968315	Negative	1000	0.359	16	0.010	21	7/18/2013	Kuester	
85	968315	Negative	1025	0.365	10	N/A	N/A	6/25/2013	Wilcox	
86	968315	Negative	1050	0.370	10	N/A	N/A	6/25/2013	Wilcox	113
87	968315	Negative	1100	0.380	10	N/A	N/A	6/26/2013	Wilcox	
88	968315	Negative	1150	0.390	10	N/A	N/A	6/26/2013	Wilcox	
89	968315	Negative	1200	0.399	10	N/A	N/A	6/26/2013	Wilcox	
90	968315	Negative	1250	0.409	10	N/A	N/A	6/27/2013	Wilcox	
91	968315	Negative	1300	0.418	10	N/A	N/A	6/27/2013	Wilcox	
92	968315	Negative	1350	0.427	10	N/A	N/A	6/27/2013	Wilcox	
93	968315	Negative	1400	0.435	10	N/A	N/A	7/25/2013	Wilcox	
94	968315	Negative	1500	0.452	10	N/A	N/A	7/25/2013	Wilcox	
95	968315	Negative	1600	0.469	10	N/A	N/A	7/1/2013	Wilcox	